Series of Lectures of the University of Applied Science Ruhr West
June, 16th - 17th 2016 | Vol. 5

IEEE WORKSHOP 2016

S 2016 SENSORICA

Industrial and Medical Measurement and Sensor Technology Vehicle Sensor Technology

Abstractbook

TTS Technische Thermodynamik Siegen

UNIVERSITÄT SIEGEN

HRW HOCHSCHULE RUHR WEST
UNIVERSITY OF APPLIED SCIENCES
INSTITUT MESS- UND SENSORTECHNIK

ITMO UNIVERSITY

IM Chapter IEEE GERMANY SECTION

Introduction

The highly successful lecture series on the topic of measurement and sensor technologies as part of the IEEE Workshop at the University of Applied Sciences Ruhr West (HRW) is being continued in collaboration with the University of Siegen, the TU Chemnitz and the ITMO National Research University of Information Technologies, Mechanics and Optics in St. Petersburg. This time the event is featuring an even more international orientation by linking it with the Russian SENSORICA. The topics cover industrial and medical measurement technology as well as sensor technology in vehicles.

Our event offers a platform for knowledge transfer between industry and public and commercial research institutions in the area of measurement technology.

This Abstract Book offers the opportunity of contacting speakers even after the event. In addition we are very pleased to have selected contributions published in a special edition of the journal „tm Technisches Messen“ (De Gruyter Oldenbourg Verlag) again this year.

We like to thank everybody having contributed to the success of this workshop and are looking forward to lively discussions!

The Organizing Committee:

Prof. Dr. Jörg Himmel
University of Applied Sciences Ruhr West
Prof. Dr. Olfa Kanoun
Chemnitz University of Technology
Prof. Dr. Gennadij Lukjanow
ITMO University, St. Petersburg
Prof. Dr. Thomas Seeger
University of Siegen
Prof. Dr. Klaus Thelen
University of Applied Sciences Ruhr West

Contents

Thermographic phosphors as temperature sensors for the gaseous, liquid and solid phases

B. Fond, Ch. Abram, F. Beyrau - Invited Talk

Lehrstuhl für Technische Thermodynamik, Otto-von-Guericke Universität Magdeburg, Magdeburg 39104, Germany

Authors e-mail address: benoit.fond@ovgu.de

Abstract

This talk discusses thermographic phosphor particles as versatile optical sensors allowing the measurement of surface temperatures, but also temperature of liquids and gases. While phosphor thermometry on surfaces is a rather mature technique, recent developments have extended the concept to the study of fluid flows, e.g. those involving heat transfer or chemical reactions, by introducing micrometre-size phosphor particles into these flows. The feature of these optical sensors and their implementation is discussed for temperature imaging in the respective phases.

Thermographic phosphors are solid crystalline materials with temperature-dependent luminescent properties. Upon excitation, typically with UV radiation, the phosphor material emits luminescence, often red-shifted and with a wide range of lifetimes spanning hundreds of picoseconds to several milliseconds. While rare-earth doped insulators, e.g. $Y_2O_3:Eu^{3+}$ were extensively investigated, a very wide range of materials present interesting luminescent properties for temperature sensing, including semiconductors, e.g. ZnO [1]. Most of these materials are inert and have a high melting point (often above 2000 K), which are favorable features in harsh environments e.g. in presence of shocks or chemically reacting flows. For remote thermometry, either the temperature dependence of the luminescence lifetime (temporal method), or that of the emission spectrum (spectral method) is exploited. These temperature dependencies often span many hundreds of kelvin for a single phosphor. In addition some materials are suitable for thermometry at low temperatures, e.g. below 200 K, while others can be used above 1400 K.

For surface temperature measurements, a thin layer of phosphor (10-50 microns thickness) is deposited onto the surface of interest (e.g. piston crown, combustor liner, pipe wall), and excited by a laser or a LED. A robust approach for temperature imaging on solid surfaces consists of recording hundreds of frames with a high frame rate camera (kHz – MHz) of the luminescence emission following a short laser pulse (~10 ns). This way, a decay time can be extracted at each spatial location from the time series of recorded luminescence intensities (see Fig. 1 left), which is then converted to temperature using calibration data. Owing to the large number of samples, and to the high sensitivity of the temporal response of many phosphors to temperature, precision as high as 0.2 K can be obtained. As an illustration, here a coating composed of $YAG:Cr^{3+}$ is used to study fluid-to-wall heat transfer in a throttled flow expanding into a square-section optically accessible tube. It reveals a rather large region of uniform cooling rate as opposed to our initial expectation of a highly localised impingement type cooling.

This lifetime imaging approach is however limited to measurements on still or slow-moving objects, due to the relatively long measurement times (30 µs - 5 ms). For fast-moving objects e.g. turbine blades, and necessarily for temperature measurements in turbulent flows of liquid or gas, the spectral method must be used since it requires a single exposure, which can be as short as ns-µs. In this case, two spectral filters are carefully chosen to exploit the temperature dependence of the emission spectrum, as shown in Fig. 1 (right). These are mounted on image sensors so as to record a pair of spectrally filtered images. A ratio is then generated from each image pair, which is converted into temperature from calibration data.

Over the past 10 years, the concept of using thermographic phosphors tracer particles for temperature in gaseous flows has been explored [2,3,4]. In gases, small particles (~ 1-2 microns) must be used in order to follow turbulent fluctuations in the gas temperature [4]. In addition, since the suspensions must be very dilute (~100 particles/mm^3), only very bright phosphors with a short lifetime (µs and below) suiting the necessarily short camera exposure time offer sufficient signal levels. Therefore the constraints on suitable luminescence properties, and therefore useful phosphors, are considerably more stringent than for phosphors for surface measurements. $BAM:Eu^{2+}$ and ZnO are suitable and have been demonstrated for flow thermometry with a precision of up to 10 and 3 K respectively [1,5]. Additionally a very attractive feature of using thermographic phosphor particles as a flow temperature tracer is that the same particles can be used to simultaneously measure the flow velocity field using a standard Particle Image Velocimetry approach [4]. The temperature-velocity pair obtained in this way is an especially valuable progression toward combined vector-scalar imaging, offering a unique insight into turbulent heat transfer processes and/or turbulence-chemistry interactions. Following demonstration studies of the combined technique in jet flows, the concept was extended to kHz-rate measurements using high repetition rate lasers and cameras, allowing the time-resolved studies of flow instabilities, see Fig. 2 [6]. In this

talk, the applications of the technique to two practical test cases are presented, gas turbine film cooling, and the investigation of Joule-Thomson cooling in the throttled flow configuration mentioned above. Both cases illustrate the wealth of information provided by these measurements, in particular as validation datasets for numerical models. Interestingly, the velocity-temperature pair measured in the throttled configuration clearly shows the presence of a back-flowing warmer fluid layer near the wall, which explains the uniform cooling rate distribution observed in the surface measurements.

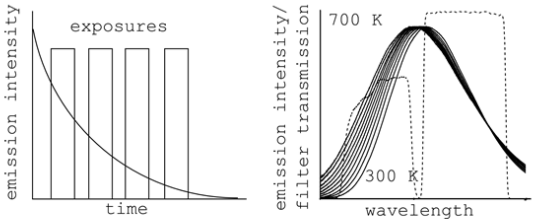

Fig. 1: Temporal (left) and spectral (right) method for temperature determination using thermographic phosphors

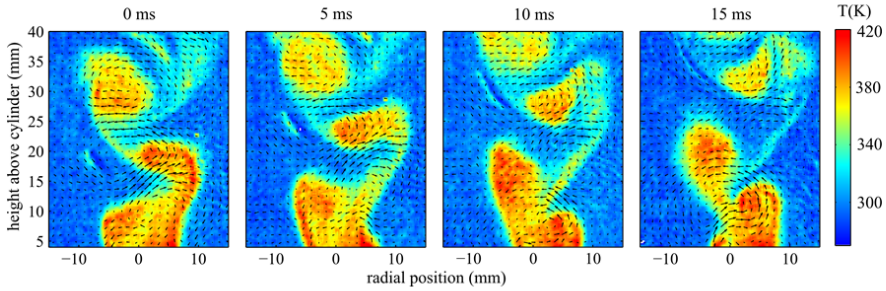

Fig. 2: Temperature and velocity fields measured in the wake of a heated cylinder [6].

Finally, the use of phosphor particles for temperature measurements in liquid flows has also been explored using an implementation similar to that for gas-phase measurements [7]. Although the particle size requirements can be slightly relaxed (~5 microns), a specific excitation scheme may be necessary to avoid interferences from Raman scattering of excitation laser light by the liquid molecules. Measurements in a buoyant thermal plume are presented, as an illustration of the potential of the technique for natural convection studies.

These various examples from our laboratory of using thermographic phosphors particles as a sensors for temperature (and velocity) measurements of all three phases illustrate their potential as a research tool for providing a more complete picture of complex fluid/thermodynamic systems, as well as for sensing in industrial processes and even natural or biological systems. Yet, there is much work to be done in for example increasing the maximum measurable temperature or improving the temperature sensitivity. The almost infinite variety of thermographic phosphors, mostly uninvestigated for the purpose of temperature sensing, means that the outlook of successful further developments in these directions is promising.

References

[1] Abram, C., Fond, B., and Beyrau, F. 2015. High-precision flow temperature imaging using ZnO thermographic phosphor tracer particles. *Opt. Express*, 23, 19453-19468.

[2] Omrane, A., Petersson P., Aldén M., and Linne M. 2008. Simultaneous 2D flow velocity and gas temperature measurements using thermographic phosphors, *Appl. Phys. B Lasers O,* 92, 99-102.

[3] Rothamer, D. A., and Jordan, J. 2012. Planar imaging thermometry in gaseous flows using upconversion excitation of thermographic phosphors. *Appl. Phys. B Lasers O*, 106, 435- 444.

[4] Fond, B., Abram, C., Heyes, A. L. , Kempf, A. M. , and Beyrau, F. 2012. Simultaneous temperature, mixture fraction and velocity imaging in turbulent flows using thermographic phosphor tracer particles, *Opt. Express,* 20, 22118-22133.

[5] Fond, B., Abram, C., and Beyrau F. 2015. Characterisation of the luminescence properties of BAM Eu^{2+} particles as a tracer for thermographic particle image velocimetry. *Appl. Phys. B Lasers O*, 121, 495–509

[6] Abram, C., Fond, B., Heyes, A., and Beyrau, F. 2013. High-speed planar thermometry and velocimetry using thermographic phosphor particles. *Appl. Phys. B Lasers O*, 111, 155–160.

[7] Abram, C., Poujin, M., and Beyrau, F. 2016. Temperature field measurements in liquids using ZnO thermographic phosphor tracer particles. *Submitted to Experiments in Fluids.*

The prototype of the sensor system for monitoring greenhouse gas emissions to wastewater treatment plants

A. Malyshev[1], G. Lukyanov[1]

[1]*Department of Laser and Light Engineering, ITMO University, Saint Petersburg 197101, Russia*

Authors e-mail: malyshev_alexey@hotmail.com

Abstract

This article describes the use of non-contact measurement methods of gas concentrations at the station sewage treatment plants by means of a sensor system based on optocoupler LED - photodiode, then the device. This device is housed in a plastic box above the water surface, where the measurement of carbon dioxide concentration in real time. The experiment was conducted on different areas of treatment facilities to compare the volume of carbon dioxide emissions from these zones. At the end of the experiment it was concluded that the possibility of using the system for the measurement of carbon dioxide concentrations.

For wastewater treatment plants greenhouse gas emissions characterizes the efficiency of water treatment technology cycles. Oxidation of water at the water treatment is needed to improve the efficiency of its further purification. The decrease of pH levels accompanied by a shift of carbon balance and, in the formation of excess carbon dioxide and its emission into the atmosphere until a new equilibrium. Thus, compliance with treatment technologies to minimize greenhouse gas emissions.

Monitoring of greenhouse gas emissions reduced to determining the "carbon footprint", ie the calculation of greenhouse gas emissions. Currently, the following standards for their calculation: ISO 14064-1: 2006 GOST R 14064-2007, PAS 2050: 2011. According to these standards, there are three methods to measure the greenhouse gas emissions:

- Calculation based on (1) information on the activities of the company on greenhouse gases multiplied by the emission factor or the removal of greenhouse gases; (2) using models; (3) correlations specific to the production area [1];
- Measurement [2, 3];
- The combination of measurement and calculation[4].

The role of measurement in general is determining in the assessment of how indirect emissions and assess of the direct emissions of greenhouse gases into the atmosphere. In most of water treatment companies currently quantification of greenhouse gas emissions reduced to the calculated data, based on energy consumption data of companies [1].

In the works of Russian scientists of Rostov State Construction University, headed by prof. NS Serpokrylovym noting the relationship between the composition of water in sewage treatment plants, purification process and the emission of greenhouse gases: carbon dioxide, ammonia, hydrogen sulfide and methane. Measuring greenhouse gases authors performed indirectly, by fluctuations in the partial pressure of gas at the surface of the water. Further, on the basis of observations made, offered a table indicator of carbon dioxide emissions - compliance / violation of the technological cycle[7].

Also in the works of foreign colleagues for the measurement of carbon dioxide flux on the water surface following methods are used to collect samples:

1) Open and closed container method for sampling ambient air samples in different areas of sewage treatment plants that are not ventilated;
2) The method of use of plastic bags for collecting ambient air samples from ventilated areas.

Next, these samples were studied in the laboratory for the presence of various concentrations of gases such as methane, carbon dioxide and nitrogen [8-9].

Monitoring of emissions of greenhouse gases at wastewater treatment plants can be based on the sensor system, including sensors measuring the concentration, wireless data collection, data collection to digital converter. Measuring the concentration of greenhouse gases in the on-line in the water and surface water without sample collection can be performed by optocoupler LED-photodiode (LLC "ICE-microsensors"). The proposed optoelectronic devices designed for the mid-infrared (1.6-5.0 microns) on the basis of narrow gap nanoheterostructures system GaSb-InAs. The characteristic absorption bands of carbon dioxide, methane, nitrous oxide just are in the mid-IR. The advantages of LEDs in the middle infrared region as compared to the thermal sources of infrared radiation and adsorption, catalytic sensors are compact (chip size 0.3x0.3 mm), low power (pulsed about 1 mW), high speed (tens of nanoseconds), high service life (80,000 - 100,000 hours), the possibility of creating miniature multi-element arrays and matrices. A prototype of on the sensor system is presented in Fig. 1. It includes device, enclosed in case with connectors to provide power supply and to receive

signal from optocoupler. Further that plastic box placed in plastic box with volume of 11 m3 that attached to metallic holder. By using that metallic holder we can place device near water surface to perform experiment.

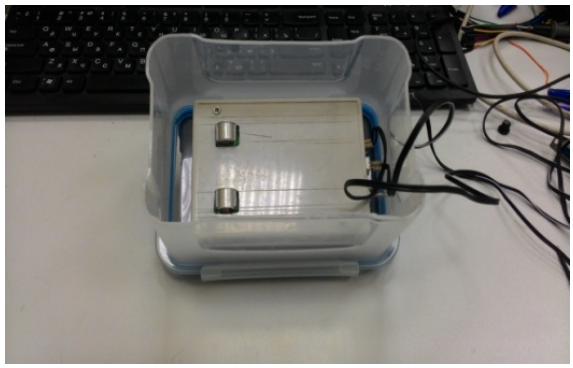

Fig.1 A prototype of the sensor system.

At the water treatment plant GUP Vodokanal of St. Petersburg performed testing a prototype of the sensor system for monitoring carbon dioxide emissions. Prototype testing was carried out near the water surface at the outlet section №3 WWTP. The measurement results are shown in Fig. 2.

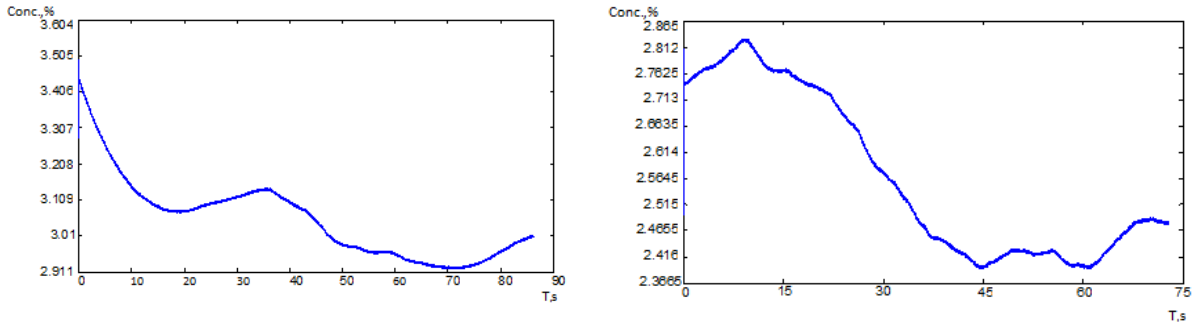

a *b*

Fig.2 a - aerobic zone №4, b – aerobic zone № 3.

References

[1] Aderhold J, Davydov V Yu, Fedler F, Klausing H, Mistele D, Rotter T, Semchinova O, Stemmer J, Graul J 2001 *J. Cryst. Growth* **151** 701
[2] Strite S, Morkoc H 1992 J. Vac. Sci. Technol. B **10** 1237
[3] Nakamura S, Senoh M, Nagahama S, Iwase N, Yamada T, Matsushita T, Kiyoku H and Sugimoto Y 1996 *Japan. J. Appl. Phys.* **35** L74
[4] Sze S M 1969 *Physics of Semiconductor Devices* (New York: Wiley–Interscience)
[5] Dorman L I 1975 *Variations of Galactic Cosmic Rays* (Moscow: Moscow State University Press) p.103
[6] Caplar R and Kulisic P 1973 Proc. Int. Conf. on Nuclear Physics (Munich) vol 1 (Amsterdam: North-Holland/American Elsevier) p 517
[7] Kamenev J., Popova J. Increase of operating efficiency of sewage-purification facilities by regulation of modes on basis of an short-time check-out methodology by emission of gases. Naukovedenie, 2103, № 6.
[8] Andrew G. Schneider, Amy Townsend-Small, Diego Rosso. Impact of direct greenhouse gas emissions on the carbon footprint of water reclamation processes employing nitrification–denitrification. Science of The Total Environment, Volume 505, 1 February 2015, Pages 1166-1173
[9] Xu Yan, Lin Li, Junxin Liu. Characteristics of greenhouse gas emission in three full-scale wastewater treatment processes. Journal of Environmental Sciences, Volume 26, Issue 2, 1 February 2014, Pages 256-263.

Highly sensitive "Molecular LIBS" for the detection of halogens in chlorine-contaminated concrete

Th. Dietz, A.-S. Rother, P. Kohns, G. Ankerhold

University of Applied Sciences Koblenz – RheinAhrCampus, Laser Spectroscopy and Photonics, Joseph-Rovan-Allee 2, 53424 Remagen, Germany

Authors e-mail address: ankerhold@hs-koblenz.de

Abstract

Laser-Induced Breakdown Spectroscopy (LIBS) with pulsed laser excitation is an established method for analyzing the atomic components of an unknown sample based on their characteristic emission spectra. However, LIBS provides insufficient results if atoms to be measured exhibit weak elemental emission lines in unfavorable infrared spectral regimes or if characteristic elemental spectra are disturbed by overlapped stronger lines of other elements in the sample (Fig. 1a) [1].

The analysis of the much more intense molecular emission bands arising in the plasma cooling phase seems to be a promising solution. This requires a time-resolved measurement of the LIBS spectra [2,3]. The molecular analysis is carried out on the observation of newly formed radicals and diatomic molecules whose strong emission bands are often in the visible spectral region. We use "Molecular LIBS" instead of atomic or ionic LIBS for the elemental analysis of chlorine in concrete, in which chlorine included in the cement, reacts to calcium chloride (CaCl) with the calcium contained in the cement (Fig. 1b).

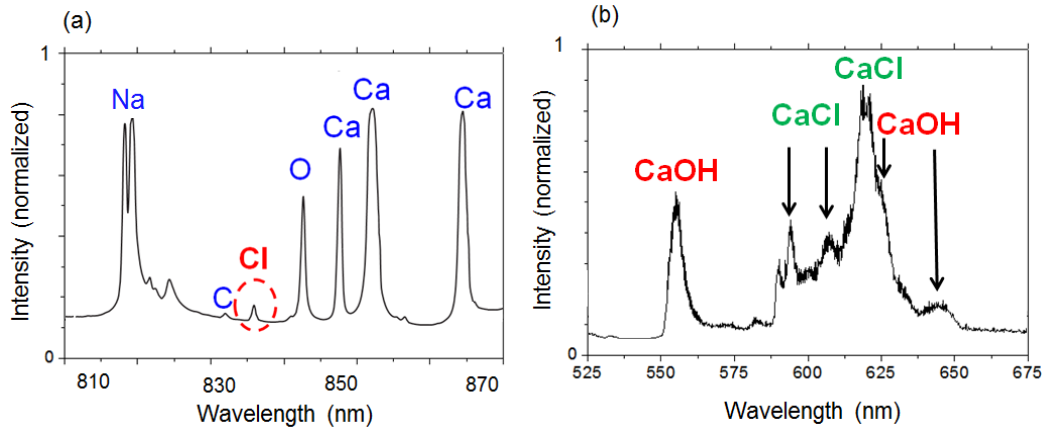

Fig. 1: (a) weak emission line of chlorine at 837.6 nm (red circle) close to strong atomic lines of other elements in a conventional LIBS experiment [1]; (b) intense molecular bands of CaCl and CaOH after a time delay of 50 µs.

The stability and hence the lifetime of buildings such as bridges or parking garages is drastically reduced by the diffusion of chloride from de-icing salt into the concrete [1]. Corrosion of the steel reinforcement occurs if the chloride contamination exceeds a certain level (pitting corrosion). The quantitative measurement of the chloride content by space-resolved techniques is therefore highly demanded since it allows estimating the damage and subsequently the lifetime anticipated.

The damage threshold of the chlorine contamination in concrete is 0.2 mass percent (European Standard EN 206: 2014) related to the proportion of cement. Well-established space-resolved methods only achieve a limit of detection of worse than 1 mass percent whereas the limit of detection in our research project is intended to be better than 0.1 mass percent.

Calibration samples required for a quantitative measurement were provided by the cooperation partner "Bundesanstalt für Materialforschung und -prüfung" (BAM). Fast evaluation electronics for the time-resolved measurement with passively Q-switched lasers are developed by the industrial partner SECOPTA analytics GmbH.

From a Principal Component Analysis (PCA) of the molecular spectra measured in the plasma cooling phase we were able to identify the best time parameters to clearly separate different concentrations of chlorine (Fig. 2a). A fully quantitative analysis of chlorine in concrete can be performed by a Partial Least Squares Regression (PLS) (Fig. 2b). Up to now, we achieve a detection limit of less than 0.2 mass percent mainly determined by matrix effects and calibration errors.

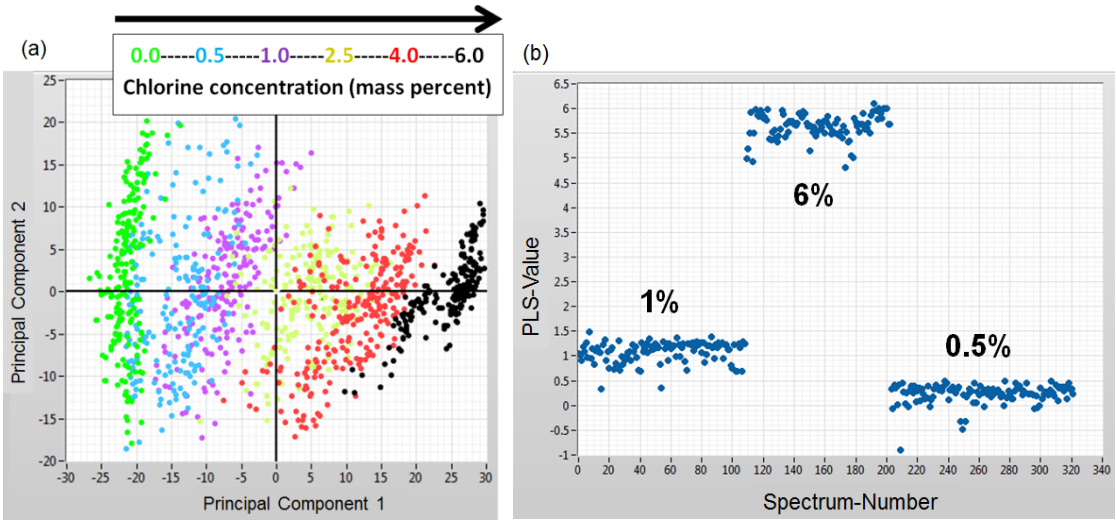

Fig. 2 (a): Principal Component Analysis (PCA) of six samples of concrete with different chlorine concentrations; (b) assignment of LIBS spectra to different chlorine concentrations applying a Partial Least Squares Regression (PLS).

Acknowledgements: This project is supported by the German Federal Ministry for Economic Affairs and Energy (BMWi), project grant No KF26821030F4. The authors thank in particular the BAM (Bundesanstalt für Materialforschung und -prüfung) and SECOPTA analytics GmbH Berlin.

References

[1] G. Wilsch, F. Weritz, D. Schaurich, H. Wiggenhauser, *"Determination of chloride content in concrete structures with laser-induced breakdown spectroscopy",* Construction and building materials, **19**, 10, 724-730, 2005.

[2] M. Gaft, L. Nagli, N. Eliezer, Y. Groisman, O. Forni, *"Elemental analysis of halogens using molecular emission by laser-induced breakdown spectroscopy in air",* Spectrochimica Acta Part B, **98**, 39-47, 2014.

[3] A.-S. Rother, P. Kohns, G. Ankerhold, *"Obtaining further Information on Sample Composition by Analyzing Radical and Molecular Band Emission in Laser-Induced Breakdown Spectroscopy"*, Proceedings of the 8th Euro-Mediterranean Symposium on Laser-Induced Breakdown Spectroscopy (EMSLIBS 2015), Linz, Austria, 14-18 Sept. 2015.

Investigation of heat transfer by the gradient heat flux sensors and PIV method

A.V. Bashkatov, A. Y. Babich, A.A. Gusakov, M. A. Grekov, A.V. Mityakov, S.Z. Sapozhnikov, V. V. Seroshtanov, V.Y. Mityakov, E. R. Zaynullina, A.N. Dymkin

Peter the Great St. Petersburg Polytechnic University, 195251, St. Petersburg, Russia

Authors e-mail address: bshktv.a@gmail.com

Abstract

In this article the investigation of simultaneous heat transfer and flow properties by the gradient heat flux sensors [1] and PIV (Particle Image Velocimetry) method is provided [2]. More particularly, research of heat transfer during cross flow around a cylinder at the Reynolds numbers of $1{,}2\cdot10^4 \ldots 5{,}2\cdot10^4$ were conducted. In addition, the vortex generators to increase the heat removal from the surface of the cylinder were successfully applied. The presented method is able to show the connection between heat transfer and flow pattern.

Experiments were carried out in the closed-circuit wind tunnel (Fig. 1). The test section of wind tunnel has 870 mm of length. Contraction cone outlet is of 450 mm in diameter. The Eiffel chamber 3 is worked out of Plexiglas to allow PIV measurements from outside the chamber. The wind tunnel is equipped with a water-air heat exchanger 2 to maintain constant flow temperature. The longitudinal turbulent intensity was found to be less than 1% for $10^4 < \mathrm{Re} < 10^5$.

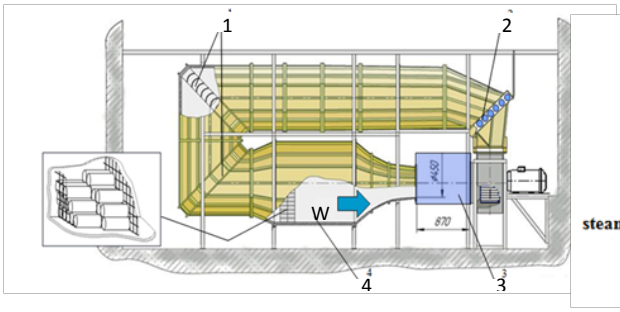

1 – turning vanes, 2 – water-air heat exchanger,
3 – Eiffel chamber, 4 – settling chamber with honeycomb
Figure 1. Scheme of the wind tunnel

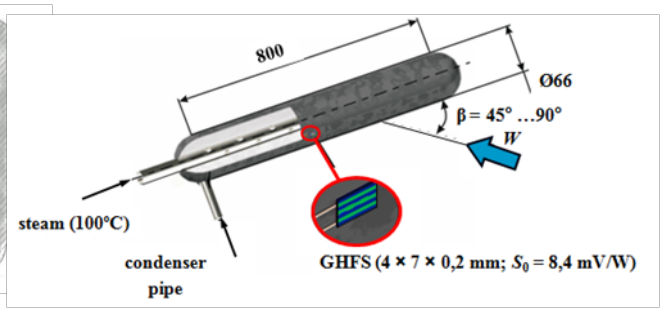

Figure 2. Scheme of the heated cylinder model

Heat flux was measured by the gradient heat flux sensor (GHFS) invented in Peter the Great St. Petersburg Polytechnic University. The operating principle of a GHFS [1] is based on a transverse Seebeck effect: when the heat flux transits through a plate with anisotropy of thermophysicl and thermoelectric properties, the thermo-electromotive force (thermo-EMF) occurs. its direction normally to heat flux vector and proportionally to heat flux rate. The response time of our GHFS is about $10^{-8}...10^{-9}$ s, which allows us to consider GHFS almost free from transit-time effects heat flux measuring unit.The GHFS is made of a single crystal bismuth, 99,99% pure [1]. Sensor platform dimensions were 2×2 mm, wih the thickness of 0,2 mm.

Fig. 2 illustrates the scheme of a cylinder model, used in the experiments and located in the Eiffel chamber (Fig. 1). The cylinder, 66 mm in diameter, is made of a steel sheet which is 0,1 mm thick. The cylinder length is 800 mm. The model was heated by the water steam with temperature about $100^{\circ}\mathrm{C}$. Experiments were carried out with constant temperature boundary conditions. The GHFS was mounted on the cylinder surface, flush with the surface (Fig. 2). The cylinder was turned around its axis by the electric driver which allowed us to move the sensor in a circumferential direction along the cylinder surface.

The principle operation of PIV system consists in that the tracers are fed into a stream, which are illuminated by light sheet-beam, divorced in plane by the cylindrical lens. On command of timing unit the laser produces a double flash, the first camera captures the tracers and the second camera records the signal of GHFS measured by the oscilloscope, The data from both cameras are transmitted to the computer for the further processing. Verification of the proposed method was considered in the paper [3].

Nusselt number fluctuation after the boundary layer separation is very high. The reason is the vortex shedding, caused by the rolling up of the separated boundary layer. Simultaneity the experiment allows us to observe this process and its influence on heat transfer. Fig. 3 illustrates Nusselt number fluctuation when the cylinder was rotated in the field of $90^{\circ} < \varphi < 100^{\circ}$. Fig. 4 shows that heat transfer intensity depends strongly on vorticity and flow velocity at the examined range.

By analogy with the Prandtl problem with the ring on the ball, series of experiments using a vortex generator in the form of thin wire (with a diameter of 0,8 ... 2 mm) were carried out. Nevertheless, we have investigated heat transfer. Since the vortex generator is cause of flow turbulence and shifts the point of separation, therefore it intensifies heat transfer.The optimal diameter, which corresponds to thickness (about 1 mm) of boundary layer and the angle of installation of vortex generators were experimentally chosen: $d_t = 1\text{mm}, \varphi_t = 55^o$.

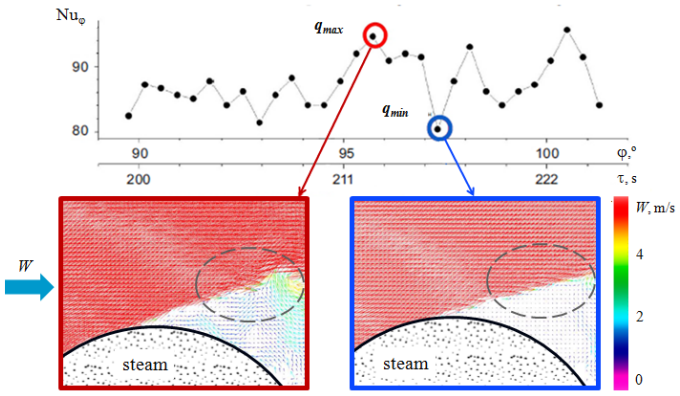

Figure 3. The angular heatgram $\text{Nu}_\varphi(\varphi)$ (a) and velocity fields (b)

Experiments with installed vortex generators showed increase of average heat transfer coefficient around the model by 14% at the $\text{Re} = 5,3 \cdot 10^4$, but in allocating vortex generator at a distance of 1,2 mm from the cylinder the lower point on a graph was removed, thereby average heat transfer coefficient was increased by 20% at the $\text{Re} = 4,9 \cdot 10^4$ (Fig. 4).

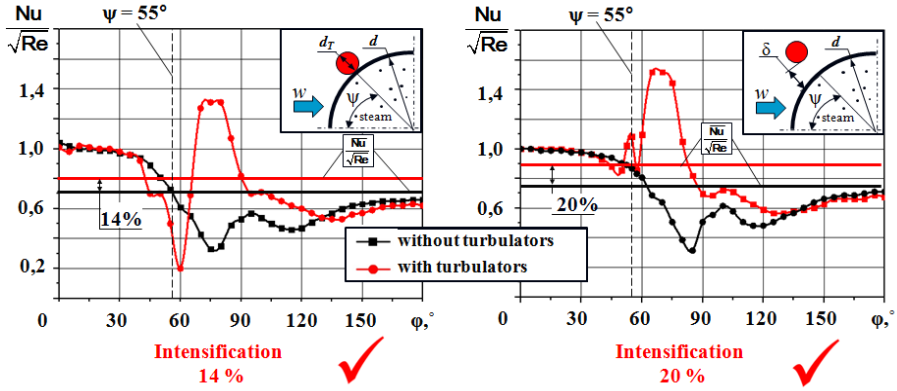

Figure 4.Influence of the gap between the vortex generator and the cylinder surface on value of of heat transfer coefficient.

Our experiment shows that the suggested method could provide us the complete dataset about the heat transfer processes related to the velocity field. Simultaneity of both experiments allows us to observe instant processes and its influence on heat transfer. Described experimental results are in a good agreement with the previous researches [4, 5], which confirms the validity of the suggested method. The results show that the suggested method requires further development and could be employed in many aspects of study.

References

[1] Sapozhnikov S. Z., Mityakov V. Y., Mityakov A. V. Gradient heat flux measurement fundamentals - St.Petersburg (2012-2013) (in Russian).

[2] Institute of Thermophysics SB RAS, Novosibirsk. «POLIS» velocity profile measuring instrument [Online]. Available: http://eng.polisinstruments.ru/

[3] Andrey Gusakov, et. al. “Simultaneous PIV and Gradient Heat Flux Measurement of a Circular Cylinder in Cross-Flow”, Applied Mechanics and Materials Vol. 629 (2014) pp. 444-449.

[4] Ertan Buyruk. Heat transfer and flow structures around circular cylinder in cross flow // Tr. J. of Engineering and Environmental Science 23 (1999), pp. 299 – 315.

[5] Hajime Nakamura, Tamotsu Igarashi. Unsteady heat transfer in separated flow behind a circularcylinder – Yokosuka, Japan.

Molecular Laser-Induced Breakdown Spectroscopy – A new gateway to an advanced material analysis

A.-S. Rother, Th. Dietz, P. Kohns, G. Ankerhold

University of Applied Sciences Koblenz – RheinAhrCampus, Laser Spectroscopy and Photonics, Joseph-Rovan-Allee 2, 53424 Remagen, Germany

Authors e-mail address: ankerhold@hs-koblenz.de

Abstract

Laser-Induced Breakdown Spectroscopy (LIBS) is a powerful and widely used method to identify the elemental composition of an unknown sample by analyzing the emitted atomic or ionic lines of spectra instantly measured after the irradiation of an intense laser pulse. Still, some elements can exhibit emission lines that are very weak beyond the detection range or overlapped by emission lines of other components, so that the detection of those elements proves to be very difficult.

It became apparent that aside from the atomic and ionic lines also broad band emission of radicals and molecules occurs after a certain delay time within the microsecond range between laser pulse and data acquisition as the plasma cools down and the atomic emission lines are getting much weaker [1-3]. This provides further spectral information about the sample composition which cannot or not as easily be obtained by the common way of analyzing LIBS spectra. Especially halogens are of great interest since they are hard to detect by common LIBS analysis.

In comparison calcium has proven to easily show strong band emission after its strong and numerous atomic lines weaken. This can be observed e. g. for dental enamel, as it emits only calcium lines within the first 10 µs after the laser pulse, which disappear after about 50 µs, meanwhile the molecular emission of CaO and CaOH, which could be identified by considering [4], becomes dominant [5].

This study focusses on how calcium related bands can be measured. Therefore, we observed the spectra emitted by samples containing native molecules of calcium and halogens as well as self-made samples which consist of a mixture of gypsum and a halogen salt. The best results can be observed for calcium fluoride (CaF_2). Differing from other examined samples, the involved processes follow a very short time line, so that within the first microsecond only atomic and ionic lines of calcium can be observed (Fig. 1a). Within the first 10 µs the CaF bands already appear, while the atomic lines are still dominant (Fig. 1b). Those CaF bands become dominant after 30 µs when the atomic emission almost completely disappeared (Fig. 1c). This behavior of CaF appears to be in good conformity with [2].

Furthermore, we found out that halogens combined with calcium are even observable without time-resolved studies, which is a new approach. Fig. 1d shows an appropriate spectrum of calcium fluoride. Among strong atomic calcium peaks also band emission can be found. This behavior could be proven to be a characteristic of calcium, since it does not show for most other elements. This can be explained as the result of strong but rather short living atomic emission compared to the less intense band emission that has a very long lifetime in comparison to other elements. Therefore, within rather long integration time of about 100 ms the weaker band emission can still compete with the strong atomic and ionic lines, which dominate most other spectra.

For the non-time-resolved examination of calcium chlorine, we initially observed the spectrum of pure gypsum ($CaSO_4$), which shows a strong band emission of calcium oxide (Ca_xO_x). When mixing gypsum with sodium chlorine (NaCl), during cooling down processes CaCl is formed and emits the correspondent bands, which suppress the emission of calcium oxide. A comparison to the emission of $CaCl_2$ chunks formed a similar spectral shape, which proves that components like halogens can be identified by observing a self-made mixture of it with gypsum. Furthermore, the sensitivity is greatly enhanced as it can be seen for fluorine in Fig. 1d, where the atomic peak of fluorine is clearly evanescent compared to the strong band emission.

In another approach, we studied a mixture of gypsum and sodium bromine (NaBr) in order to examine the formation of CaBr within the plasma. The observed spectrum was compared with the gypsum spectrum and showed just little differences, since both spectra form mostly the same shape. However, there could be found two differences, the strong atomic sodium peak and a narrow band emission that could be identified as CaBr. Differing from CaCl and CaF it seems that CaBr does not suppress the calcium oxide emission. Since we did not observe any emission of calcium sulfur compounds yet, it seems likely that the formation of molecules and radicals with certain components is more favored. Hence, chlorine and fluorine seem to be more preferred than oxygen, which itself is favored more than bromine and sulfur.

In conclusion, our studies demonstrate the high potential of "Molecular LIBS" as an extension for all LIBS setups with non-time resolved spectrometers for certain molecules containing e.g. calcium or aluminum.

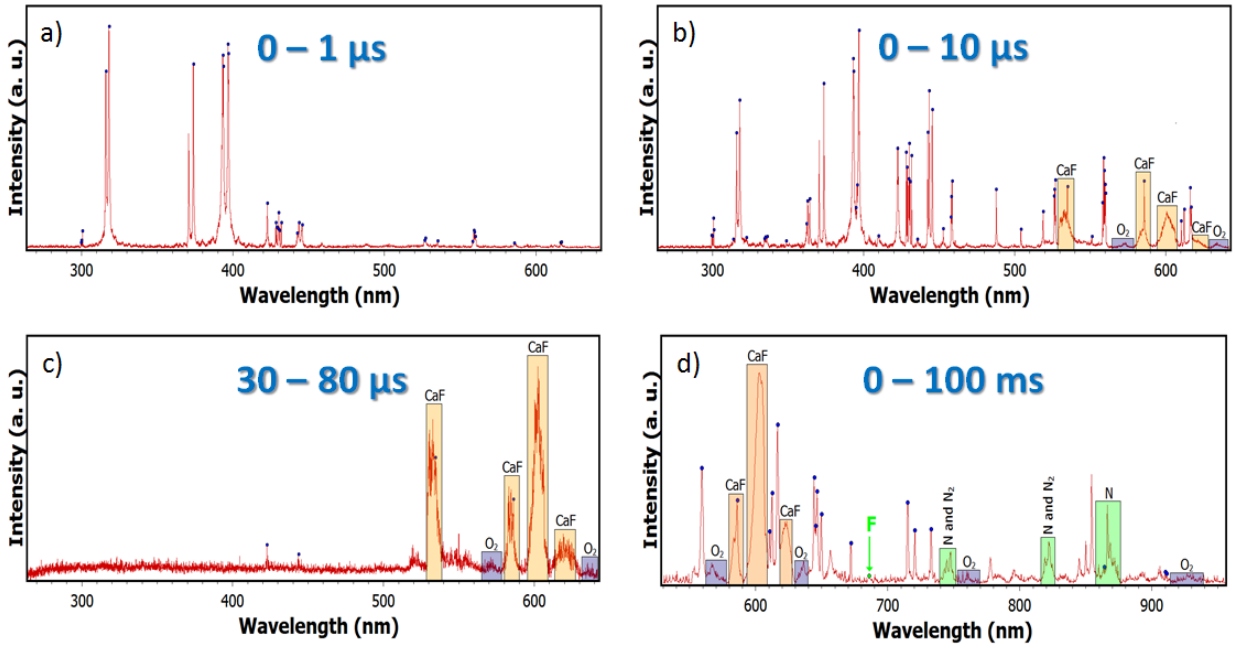

Fig. 1: Spectra observed for a calcium fluoride crystal as sample; (a) to (c) demonstrate the temporal evolution of the spectra, while (d) was measured with a non-time resolved spectrometer and shows atomic and molecular emission. The spectra have been normalized so that the intensity scaling is not shown here. The blue points show the identified atomic calcium peaks.

Acknowledgements: This project is supported by the German Federal Ministry for Economic Affairs and Energy (BMWi), project grant No KF26821030F4. The authors thank in particular the BAM (Bundesanstalt für Materialforschung und -prüfung) and SECOPTA analytics GmbH Berlin.

References

[1] C. Haisch, R. Niessner, O.I. Matveev, U. Panne, N. Omenetto, *"Element-specific determination of chlorine in gases by Laser-Induced-Breakdown-Spectroscopy (LIBS)"*, Springer, 1996.

[2] M. Gaft, L. Nagli, N. Eliezer, Y. Groisman, O. Forni, *"Elemental analysis of halogens using molecular emission by laser-induced breakdown spectroscopy in air"*, Spectrochimica Acta Part B, **98**, 39-47, 2014.

[3] V. Asselborn, A.-S. Rother, P. Kohns, G. Ankerhold, *"Sensitivity Enhancement of Laser-Induced Breakdown Spectroscopy (LIBS) by Time-Resolved Studies of the Formation of Radicals and Molecules"*, Proc. 8th International Conference on Laser-Induced Breakdown Spectroscopy (LIBS2014), Beijing, China, 2014.

[4] R.W.B. Pearse, A. G. Gaydon, *"The Identification of Molecular Spectra"*, Chapman and Hall, 4th Ed., 1976.

[5] A.-S. Rother, P. Kohns, G. Ankerhold, *"Obtaining further Information on Sample Composition by Analyzing Radical and Molecular Band Emission in Laser-Induced Breakdown Spectroscopy"*, Proc. 8th Euro-Mediterranean Symposium on LIBS (EMSLIBS 2015), Linz, Austria, 2015.

Train traffic control system based on fiber optical sensors

G. Osadtchy[1,2], D. Efanov[1,2], V. Ivanov[3], I. Razvitnov[4]

[1] AO "Institute Stroyproekt", Russia, St. Petersburg city, Dunaisky Prospect, 13/2,

[2] Petersburg State Transport University, Russia, St. Petersburg city, Moskovsky Ave. 9
[3] ITMO University, Russia, St. Petersburg city, Kronverksky Ave., 49
[4] Stock Company "Institute Giprostroymost — St. Petersburg", Russia, St. Petersburg city, Yablochkova St. 7

Authors e-mail address: osgerman@mail.ru, TrES-4b@yandex.ru, vlivanov@corp.ifmo.ru, igor.Razvitnov@gpsm.ru

Abstract

Within network of railroads of Russian Federation for traffic control of railroad trains such systems as electric token, semi-automatic block and automatic are being applied [1]. Modern railroads traffic control is considered as an automatic blocking system which composed of separates spots of control (some times dozens). Each spot of control equipped with sensor being detected train position for transmission of needed information to train operator regarding recommended speed and number of available free areas for safety movement continuation. For one way train traffic regulation signal towers are being presented. Vast terrains of Russia (Third place in the world regarding railroad network length), high requirements concerning reliability and safety plus slow rate of modern automatic technology implementation are the cause of huge quantity of relay controlled systems application for train traffic monitoring (about 90% from entire systems of train traffic management). However train traffic control systems are being gradually transformed from relay controlled systems to microprocessor's systems [2]. Meanwhile, the abovementioned transformation belongs to intellectual level of management only – introduction of segments of microprocessors per technological algorithms realization instead of relay systems logic. Orders for management fulfillment regarding wayside devices are being transformed from computing system via interface relay controlled system [3]. Sensors of microprocessor, responsible for train position detection are the same as those allocated per relay systems. At the moment there are railroad networks of tone frequencies which main weak point is colossal consumption of copper-wire cable (to be extended along total rail track), plus necessity of big quantity of operation functions [1]. Defects of cable network availability for the abovementioned system are the reason of large amount of work failures. Indeed, in case of speed rate over 200 km/h, quality of applied technology of relay-controlled system shows incorrect outcome some times. Designers of railroad trains management schemas are forced to analyze the work of automatic schemas and to insert needed corrections within it [4, 5]. Unfortunately, those measures are local and may not solve the global problem. Consequently, implementation of centralized microprocessor schemas is not a breakthrough decision without alternation of wayside technological devices. Cost effective technological solution is an application of fiber optical sensors based on Fiber Optic Bregg Grating. Similar physical effect is being conducted within Structural Health Monitoring per linear facilities [6].

Fiber optical fabric (in comparison to copper-wire material) is not the matter of electromagnetic interference [7]; in this case, the advantage is cabling procedure may be fulfilled together with power cables installation. Fiber optical cable is not affected to back traction current, chemical and electrical corrosion, pre-failure conditions will be eliminated such as short cutting in the cables and serious signal attenuation. Accumulated experience may be good opening for future execution of fiber optical connection within sphere of railroad trains management systems.

Position sensor per train circuit is the trouble spot within any system of train management. On network of railroads of Russian Federation constant flow of electrical current is being applied which effects on entire energy consumption of the whole system. Energy leakage within cable network is the heel of Achilles, which requires submission of powerful energy sources. In case of railroads for traffic control arrangement based on fiber optical sensors, energy consumption will be sharply cut down, which is the reason of low light wave decay within light-guide fiber (in this case, special amplifiers are not needed anymore for remote facilities).

Fiber optical sensors should be placed direct under rail base inside of designated spots of cribwork (Fig. 1). Information from sensors to be transmitted over the fiber optical cabling placed inside of special ditch allocated along the railroad track (Fig. 2). To increase the control of railroad train system reliability based on fiber optical connection, implementation of vapor-phase and major coding methods should be helpful together with self-controlled systems being applied integration codes [8, 9]. To obtain data from fiber optical sensors reflectors are being implemented for signal digitization and transmission to designated monitoring computer. Inside of the software of the microprocessor complex, model of railroad train management is functioning with initial data of sensors from design spots of monitoring (this is an analog of relay-controlled system). System redundancy is limited by power of node only. Computers of various areas of control to be reunited within single network of dispatch control system.

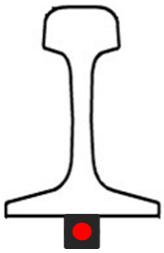

Fig. 1 Sensor fixation to rail

Fig. 2. Structural schema of data transmission arrangement

Replacement of relay-controlled system with fiber optical network should not reduce functional characteristics such as: rail circuit, sensor of train position, network integrity control system with channel of data transmission to locomotive. Besides, it will be possible to arrange the control of axel control of railroad coaches, defects of trolleys, actual live load per rails, quantity and weight of passing trains etc. [10]. That way implementation of fiber optical sensors is an advance technology in the field of railroad trains management as per low velocity of trains as well as per high speed trains.

References

[1] Theeg G., Vlasenko S. Railway Signalling & Interlocking. – DW Media Group GmbH | Eurailpress, Hamburg, 1st Edition, 2009, 448 p.

[2] Sapozhnikov Val.V., Sapozhnikov Vl.V., Efanov D.V. Application of codes with summation for the synthesis of railway automation and remote control systems based on field-programmable gate arrays // Automation on Transport, 2015, vol. 1, no. 1, pp. 84-107.

[3] Sapozhnikov Vl.V. Microprocessor-based systems of centralization: textbook for vocational training and colleges of railway transport. Moscow, GOU «Training center for railway transport education», 2008, 398p.

[4] Lykov A.A., Efanov D.V., Kuznetsov V.A. Problems in increasing reliability of ABTTs-2000 automatic block signal systems in organizing high-speed traffic // Transport of the Russian Federation, 2011, no. 3, pp. 40-43.

[5] Kravtsov Yu.A., Arkhipov E.V., Bakin M.E. Advanced coding schemes of voice-frequency track circuits // Automation on Transport, 2015, vol. 1, no. 2, pp. 119-126.

[6] Tam H.Y., Lee T., Ho S.L., Haber T., Graver T., Méndez A. Utilization of fiber optic Bragg Grating sensing systems for health monitoring in railway application // 6th International Workshop on Structural Health Monitoring, 11–13 September, 2007, pp. 1824-1831.

[7] Kravtsov Yu.A. Electromagnetic compatibility of track circuits and electric rolling stock with asynchronous traction motor // Automation on Transport, 2015, vol. 1, no. 1, pp. 7-27.

[8] Sapozhnikov Val. V., Sapozhnikov Vl. V. Self-checking digital devices. St. Petersburg, Energoatomizdat, 1992, 224 p.

[9] Sapozhnikov V., Sapozhnikov Vl., Efanov D., Dmitriev V. New Sum Code for Effective Detection of Double Errors in Data Vectors // Proceedings of 13th IEEE East-West Design & Test Symposium (EWDTS`2015), Batumi, Georgia, September 26-29, 2015, pp. 154-159.

[10] G. den Buurman A vital instrument in asset management // European railway review, 2005, no. 3, pp. 80-86.

Absorption thin film ferroelectric-polymer composite at terahertz frequencies

A. Gorbachev, L. Grigoryev, E. Sedykh

ITMO University, 197101, Saint-Petersburg, Russia

Authors e-mail address: agorbachev@corp.ifmo.ru

Abstract

Nowadays there is an intensive study of the interaction between THz radiation and inorganic and organic objects, especially biological objects. Since THz radiation lies in the submillimeter range, there is a common problem of creating an effective uncooled photodetector in the THz region.

The limiting factor in the development of devices using terahertz radiation is the lack of a developed element base of photonics, in particular the range of THz receivers with high sensitivity, operating without cryogenic cooling and that could be compatible with the planar manufacturing microdevices photonics technology. Planar technology for creating microbolometers or micro-opto-electro-mechanical (MOEMS) detectors can be used to create a photodetector module for special television systems operating in the THz frequency range. Parameters of these detectors are directly dependent on the selective absorption of terahertz radiation by layer of material applied to the techniques used in planar technology.

In this paper several related tasks were resolved. At the beginning, the process of propagation submillimeter radiation through composite material containing a ferroelectric phase in a polymer matrix was simulated. Simulation of the propagating radiation was carried out with the involvement of the Maxwell-Garnett effective medium model. We used the model of the environment with spherical shape ferroelectric inclusions.

Further, composite ferroelectric polymer containing phase of barium titanate was created. The polymer was used as the UV-curable photoresist, allowing to form a receiving area topology using laser vector lithography. The comprehensive studies about the optical and electric properties of the composite in the frequency range 0.1 - 1.2 THz have been conducted. Below, math model and equations used for simulation absorption of the material under investigation will be discussed.

Often, in optics, considering the effective medium approximation models electrostatic approximation is used, which includes as the smallness of particle size, as spacing relative to the wavelength used. If any of these conditions is broken, it should be taken into account the scattering by particles that nanocomposite consists of, as well as the interference of scattered waves.

Existing mathematical models describe composite structures based on Mie theory, which considers the optical properties of an isolated particle as a multipole expansion waves scattered from the scope with radius that is small in comparison with the wavelength of the incoming radiation. In this paper, to describe composite media dielectric constant of the composite and the environment are used.

The basic equation from effective medium approximation theory allowed us to calculate the overall dielectric constant ε of the composite material:

$$\frac{\varepsilon - \varepsilon_m}{L(\varepsilon - \varepsilon_m) + \varepsilon_m} = \eta \frac{\varepsilon_p - \varepsilon_m}{L(\varepsilon_p - \varepsilon_m) + \varepsilon_m} \quad (1)$$

where ε_m - the dielectric constant of the matrix, ε_p - the dielectric constant of the inclusions, η - the volume fraction of inclusions, L - depolarization factor. Some efforts were made to apply this theory to metallic particles in such composites [1]. In this study the idea was developed and applied to composite medium containing ferroelectric particles. The absorption spectra were calculated according to the equations (2-3):

$$\eta(\omega) = \frac{2\omega}{c} Im\sqrt{\epsilon_c(\omega)\mu_c}(\omega) \quad (2)$$

$$I(\omega) = I_0 e^{-\eta(\omega)d} \quad (3)$$

where ω – frequency, ϵ_c, μ_c – magnetic and dielectric constants of the medium, η - absorption coefficient, d - thickness of the sample.

Properties of the material can be considerably changed due to the particle size within its structure, or the film thickness, when these parameters are below some critical value. In such cases, it may be observed permittivity dependence on the size of its constituent particles. This phenomenon is called size effect [2].

Most of the studied today ferroelectric thin films are nanostructured, consisting of a particle size of about ten nanometers. In some issues [66] it was shown that the surface of each particle constituting the thin film is a thin

non-ferroelectric layer having a thickness of about 3 nm from the dielectric constant of about 40. This layer is called the "dead" layer. It must be taken into account when calculating the effective dielectric constant of the thin film, since its presence results in a decrease in its value.

To calculate the effective dielectric constant used the formulas given in [3]:

$$\varepsilon_{eff} = \frac{9\varepsilon_1\varepsilon_2\varepsilon_3 a^3 + 3\varepsilon_2\varepsilon_3(\varepsilon_1 + 2\varepsilon_1)(b^3 - a^3)}{\varepsilon_1\varepsilon_2(2a^3 + b^3) + 2(\varepsilon_1\varepsilon_3 + \varepsilon_2^2)(b^3 - a^3) + 2\varepsilon_2\varepsilon_3(2b^3 + a^3)} \quad (4)$$

where r - radius of the particles, b = a + t (t - the thickness of the "dead" layer), ε_1 - the dielectric constant of the particles, ε_2 - the dielectric constant of the "dead" layer, ε_3 - the dielectric constant of the medium around the "dead" layer, while $\varepsilon 2 << \varepsilon 3 < \varepsilon 1$.

To calculate the abortion spectrum used by expressions given in [1].

One of the most common methods today to generate terahertz radiation is using photoconductive antenna, supplied with a bias voltage by using two sources of visible or infrared radiation with nearby wavelengths. When the field of these sources are formed on the photoconductive antenna photocurrent occurs at a frequency corresponding to the difference of the wavelengths incident to the antenna.

To investigate the optical characteristics of the composite in the terahertz spectral region the setup was used, presented below.

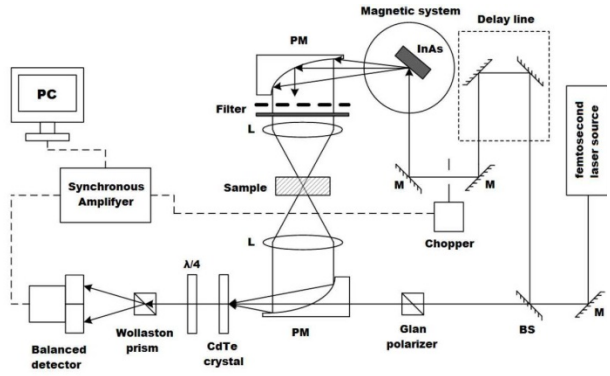

Fig. 1: The experimental setup to study the optical properties of composite ferroelectric material in polymer containing barium titanate.

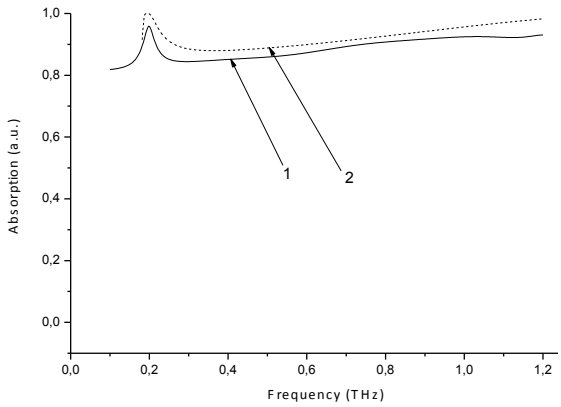

Fig. 2: Comparison simulation absorption of the composite material to the result obtained during the experiment: 1- experimental absorption in thin film composite with $BaTiO_3$; 2- simulation absorption in composite.

Based on the results of the research uncooled photodetector was created that effectively registers terahertz radiation, and is compatible with thick film integrated circuit manufacturing technology. Futher investigation the frequency characteristics of the pyroelectric detector based on ferroelectric polymer composite showed that the photodetector effectively registers input THz radiation with a modulation frequency up to 50 kHz.

References

[1] Kurbatsky V.P., Korotun A.V., Pogosov V.V. Effect of Quantization of the Electron Spectrum of Small Metallic Particles on Optical Absorption in Composite Materials // Technical Physics V.82. N 9. P. 130 - 134 (2012).

[2] Vendik, O. G.; Zubko, S. P. // Crystallography Reports; Nov2004, Vol. 49 Issue 5, p.1-7

[3] Chen B., Yang H., Zhao L. et al. // Appl. Phys. Lett. 2004. V. 84. N 4. P. 583-585.

Laser-Induced Gratings in Probing Gases and Liquids

D.N. Kozlov[1,3], J. Kiefer[2], Th. Seeger[3,4]

Invited Talk

[1] *A.M. Prokhorov General Physics Institute, Russian Academy of Sciences, 119991, Moscow, Russia*
[2] *Technische Thermodynamik, Universität Bremen,D-28359 Bremen, Germany*
[3] *Lehrstuhl für Technische Thermodynamik, Universität Siegen,D-57076 Siegen, Germany*
[4] *ITMO University Saint Petersburg, 197101 Saint Petersburg, Russia*

Authors e-mail address: dnk@kapella.gpi.ru

Abstract

Laser-induced gratings (LIGs, also known as transient gratings, TGs) are locally excited transient spatially-periodic modulations of the complex refractive index of the medium. LIGs are generated if two coherent equally polarized pump beams from a pulsed laser are crossed at a small angle and create a fringe pattern in the intersection region. Thermalization of the energy conveyed to the resonantly absorbing species of the medium by the pump radiation, as well as electrostriction (the deformation of a dielectric material in an electric field due to its polarization), result in transient modulations of the density in the form of a superposition of standing acoustic waves and stationary density gratings, with a spatial period equal to the fringe spacing. These density modulations cause the respective modulations of the refractive index.

The temporal evolution of the density modulations formed by thermalization depends on the rate of the energy exchange. Rapid energy exchange generates a standing acoustic wave and a stationary density grating. Slow energy exchange favours the formation of the stationary density grating, while the development of the acoustic contribution is suppressed. The acoustic waves are damped due to viscosity and heat conduction of the medium, as well as due to the divergence of the two counter-propagating acoustic wave packets, forming the standing wave, from the excitation volume. The stationary density modulations decay by heat conduction alone.

To detect LIGs, a third, continuous-wave probe laser beam, is adjusted to cross the pump beams intersection region (probe volume) at an appropriate angle and to be Bragg-diffracted by the LIG. The power of the diffracted radiation, detected with high temporal resolution (the LIG signal), characterizes the evolution of the transient grating. From this signal, information about the local thermophysical properties of the medium, including speed of sound, thermal diffusivity, and acoustic damping rate, is extracted.

The non-linear optical technique employing LIGs enables the non-contact determination of a few parameters in a single measurement, with the spatial resolution defined by the dimensions of the probe volume. In addition, since the measurements can be performed using a single laser pulse, the technique can provide data at a definite moment after a single transient event or at high repetition rates, determined by the repetition rate of the pump laser, during an ongoing process. This is of interest for real-time process monitoring and control purposes.

A typical experimental setup used for diagnostics employing LIGs comprises a pulsed pump laser, a cw probe laser, a set of optical elements used to attenuate, split, direct, focus and collimate the beams, a fast photomultiplier to detect the light diffracted by a LIG, a digital oscilloscope, with a trigger photodiode, and a computer. In particular, the lasers employed in the presented experiments were a Q-switched Nd^{3+}:YAG laser (10 Hz, 1064 nm) and a cw argon ion laser (515 nm) or frequency-doubled diode-pumped Nd^{3+}:YAG laser (532 nm).

The application of the LIGs technique to gas diagnostics is exemplified by the results of quantitative investigations of a non-stationary pressurized fuel injection into air at elevated pressure and temperature, under non-reacting conditions. The fuel was being injected into a chamber through a swirl gasoline direct-injection nozzle. Heated gaseous or liquid propane, C_3H_8, as the main component of liquefied petroleum gas, was employed, the parameters of the experiment (like temperature, amount of injected gas, and pressure) being close to conditions of practical interest which exist in real engines with direct injection. The measurements were performed inside the fuel jet at different distances from the injector outlet along the axis of propane injection, and were repeated at increasing delays after start of the injection pulse. The temporal shape of the LIG signals, containing non-resonant electrostrictive and resonant thermal (due to weak absorption of the 1064 nm pump radiation by C_3H_8 molecules) contributions, was recorded in a single-shot mode. Various approaches for the fast evaluation of the temporal shape of the measured LIG signals has been tested. As a result, the local vapor-phase fuel concentration (or the fuel-air ratio) and the temperature during the temporal evolution of the direct-injected fuel spray have been determined simultaneously. In particular, propane concentrations in the range of 0.2-8 % could be defined.

The employment of LIGs to probing liquids is exemplified by the studies of thermophysical properties of room temperature ionic liquids (RTILs). Over the past two decades the beneficial properties of these substances for applications as solvents, reaction media, electrolytes, etc. have been understood. The countless number of potential combinations of cations and anions composing RTILs enables tailoring fluids with the desired properties for specific applications.

A few samples belonging to a common sub-class of RTILs based on dialkyl-imidazolium cations, with 1-ethyl-3-methylimidazolium ([EMIm]) cation and different anions, at ambient pressure and temperature have been taken for the studies. LIGs were being created as a result of thermalization of a quasi-resonant excitation of highly-lying combinational vibrational states of the RTIL molecules and electrostrictive compression of the liquid by radiation of the pump laser.

By fitting temporal profiles of single LIG signal measurements, the speed and damping of the laser-excited acoustic waves in the RTIL samples, as well as their thermal diffusivity were simultaneously derived. Based on these values and data from the literature, isentropic compressibility, thermal conductivity, and bulk viscosity of the samples were determined. Good agreement between the obtained values and some of those already available from alternative studies has been found. Hence, the technique proves to be a practical instrument to obtain data necessary for modeling the properties of ionic liquids with arbitrary composition or to screen samples in the production process of RTILs with specific properties.

The presented results demonstrate the possibilities of the LIGs technique in accurate systematic measurements of multiple properties of molecular gases and liquids. In particular, if 1064-nm radiation of a Q-switched Nd^{3+}:YAG laser is employed, the technique is shown to be useful when applied to the media with species containing CH-, CH_2-, or CH_3- functional groups.

Measurement and Analysis of Wave Front Structures of Diode Lasers

I.-M. Eichentopf[1], M. Reufer[1]

[1] *Hochschule Ruhr West, Institute of Natural Sciences, Duisburgerstr. 100, 45479 Mülheim an der Ruhr, Germany*

Authors e-mail address: inga-maria.eichentopf@hs-ruhrwest.de

Abstract

In order to analyze the beam quality of laser sources wave front measurements using a Shack-Hartmann sensor became an established way. With the detection of the wave front deflection a change of the modal composition of the laser beam can be recorded directly. While this method is well known for nearly Gaussian laser beams, the wave front analysis of broad area semiconductor lasers is an open field of current research. Detailed analysis of the wave front gives an additional path to get insight into the modal composition of semiconductor lasers, which have a dominant impact on the output parameters of the devices. For our investigations we utilize lasers emitting light in the near infrared (λ= 980nm) based on the material system GaAs. For this type of laser the number and structure of optical modes is affected by thermal as well as electric effects inside the active medium. In our investigations we associate the detected wave front with a composition of Lengendre polynomials and detect their transformation with changing working conditions of the laser.

The setup is shown in the Fig. 1 (a). The intensity and wave front of the optical far field of a single emitter is measured by means of a Shack-Hartmann sensor [1]. This type of sensor consists of a conventional CCD chip, which is covered with a micro lens array. The lens array splits the incoming light into a multitude of elementary beams focused on different areas on the CCD. The difference between the angle of radiation of the measured wave front and a flat reference wave front is detected. Based on this information the local gradient of the wave front can be determined and the wave front can be reconstructed by using mathematical algorithms. In Fig. 1 (b) the cross-sections of a typical intensity distribution of a multimode laser is shown.
In y-direction the so called fast diverging axis (FA) shows a Gaussian shape. The significant intensity modulation appears for the x-direction, the slow diverging axis (SA).

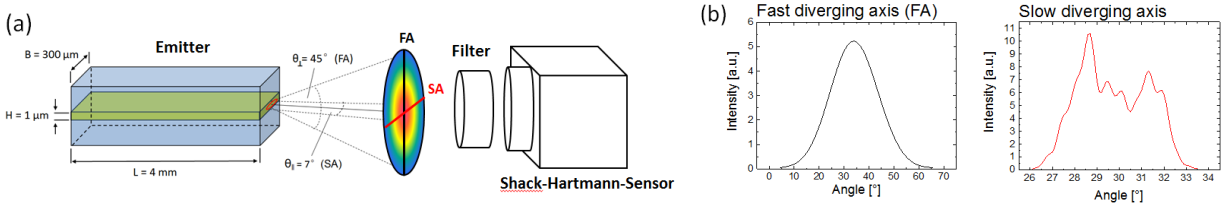

Fig. 1: (a) Experimental Setup with a laser diode, filters and Shack-Hartmann sensor; (b) Typical measurements of an intensity distribution for the fast axis (FA) and the slow axis (SA).

This modulation indicates the presence of higher order modes and carries the main information for the changes of the mode structure. It can be described by a combination of incoherent Hermite-Gaussian-Modes with different weighting factors [2]:

$$I(x,y,z) \sim |\bar{E}(x,y,z)|^2 = \sum_{n,m} \left|\alpha_{n,m}\bar{E}_{n,m}(x,y,z)\right|^2 \qquad (1)$$

Where I is the intensity, E is the electric field at the position (x,y,z) and $\alpha_{n,m}$ is the weighting factor for the electric field $E_{n,m}$ of the particular Hermite-Gaussian mode.
In contrast to the intensity distribution, the wave front analysis carries in addition the information of the phase of the light wave. A characteristic wave front of a multimode laser is shown in Fig. 2 (a) for two different diode currents. The wave front of the FA shows only slight modulations whereas the wave structure of the SA changes significantly with an increase from $3I_{th}$ to $6I_{th}$ of the applied diode current. Because of the rectangular geometry of the section of the beam used for the analysis the waviness of the wave front can be fitted by a set of Legendre polynomials [3]. The amplitudes of the polynomials 6 to 32 are utilized below to describe the structural changes as can be seen in Fig. 2 (b). Thereby the polynomials 1 to 5 are not shown here since they represent typical

aberrations (Tilt x/y, Focus, Astig. 0°/45°) of the system which are removed in all mappings of the wave fronts displayed. Regarding the development of the amplitudes of the polynomials it can be determined that the main changes in the wave front structure are described by the polynomials 10, 15, 21 and 28 when the applied current is increased from $3I_{th}$ to $6I_{th}$. Comparing the distribution of weighting factors $\alpha_{n,m}$ over the modal index a change in the mode composition can be determined (see Fig. 2 (c)), which is represented in a change of the intensity distribution as well. It can be seen that fluctuations in the intensity distribution can also be detected as changes in the amplitudes of the polynomial coefficients (cf. Fig. 2 (b)). However the correlation of the polynomials and optical modes is still unresolved.

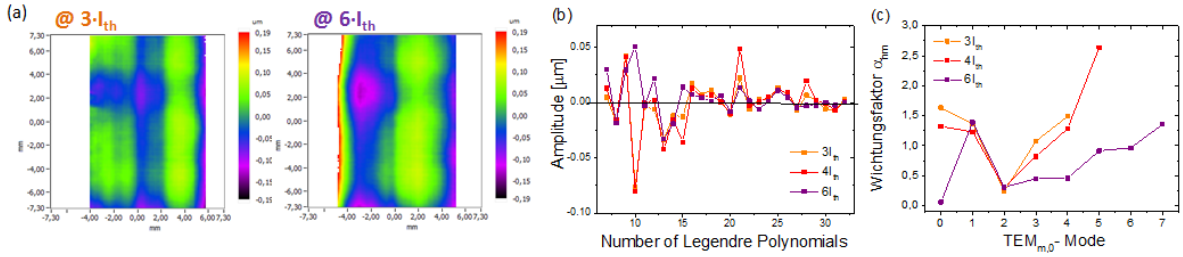

Fig. 2: (a) Wave front map and (b) amplitude distribution of Legendre polynomials for a multimode single emitter for varying diode currents in terms of I_{th} (=threshold current for the laser emission), (c) Modal composition of the beam of a multimode laser diode for different diode currents.

Additionally diodes of the same batch have been investigated while applying a current of $5I_{th}$. The wave fronts as well as the corresponding amplitudes of the Legendre polynomials are displayed in Fig. 3. Previous investigations of the intensity distribution (not presented here) show a deviation of the Gaussian shape in the fast axis for laser diode 2, which is not present for laser diode 1. In Fig. 3 (a) it can be seen that it is possible to distinguish the modal wave front composition of the two lasers. The wave front of laser diode 1 is more donut shaped while the wave front of diode laser 2 exhibits one wave in y-direction. This behavior can be resolved as well in the amplitude coefficients of the Legendre polynomials (see Fig. 3 (b)). It can be seen that the polynomials 15 to 32 represent a basic set for both diodes, but the polynomials 7, 9, 12 and 14 show clearly a deviation for both lasers. In comparison polynomials 7, 12 and 14 show higher amplitudes for laser 1 and describe the donut shape of the wave front. For laser 2 which has a wave appearing in the FA (y-direction) the polynomial 9 dominates. This polynomial indicates the modulation of the wave front in the y-direction. So the wave in the FA can be correlated to the polynomial coefficient as well as to the differences in the map of the two wave fronts.

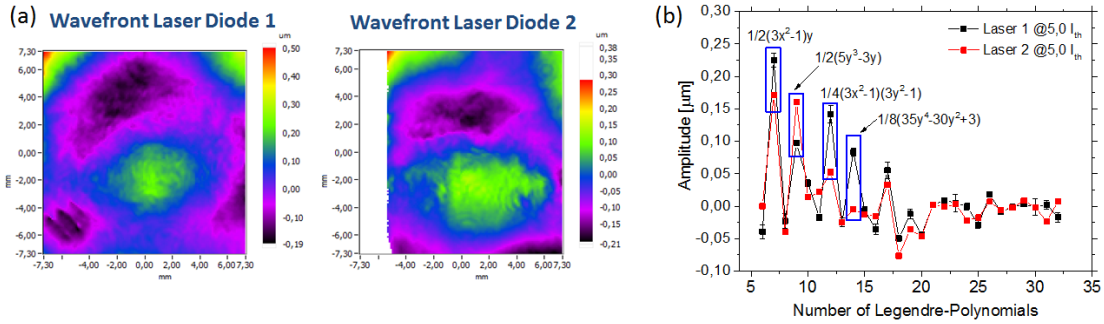

Fig. 3: (a) Wave front map for two single emitters for a state of nearly Gaussian intensity distribution at $5I_{th}$, (b) Amplitudes of Legendre polynomials with identification of the significant Legendre polynomials.

The talk will describe the development of the wave front for changing working conditions of several laser diodes and will draw first conclusions on the modal structure of the laser under investigation.

References

[1] *Charakterisierung von Laserstrahlung mittels Hartmann-Shack-Wellenfrontsensor*, M. Kunzmann, B. Schäfer, K. Mann, 2005, Photonik 1, 52-55.
[2] *Grundlagen der Photonik*, Bahaa E. A. Saleh, Malvin Carl Teich, 2., vollständig überarbeitete und erweiterte Auflage, 2008, WILEY-VCH Verlag GmbH&Co. KGaA, Weinheim.
[3] *Wavefront reconstruction algorithm based on legendre polynomials for radial shearing interferometry over a square area and error analysis*, E. Kewei, Chen Zhang, Mengyang Li, Zhao Xiong, and Daha Li, 2015 Aug 10, Opt. Express, 23, 16, 20267-79.

Simultaneous PIV and gradient heat flux measurement at the dimpled array

V.V. Seroshtanov, A.V. Bashkatov, E.R. Zaynullina, A.N. Dymkin, A.Y. Babich, A.A. Gusakov, A.V. Mityakov, S.Z. Sapozhnikov, V.Y. Mityakov

Peter the Great St. Petersburg Polytechnic University ,195251, St. Petersburg, Russia

Authors e-mail address: vladvik1992@gmail.com

Abstract

Fluid dynamic and heat transfer special aspects are important in many fields of power units design. Intensification of heat transfer may be achieved by using discrete roughness on heat-transfer area. Well known connection between surface heat transfer and fluid dynamics determines the importance of real-time experimental investigation of both processes**.** Now we present some significant results, acquired during development and probation of the new method which is based on combined use of PIV technology [1] and unique gradient heat flux sensors. In this paper the method is applied to investigation of heat transfer and fluid dynamics at the dimpled array**.**

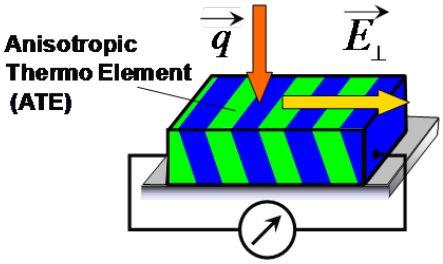

Fig. 1: Transverse Seebeck effect.

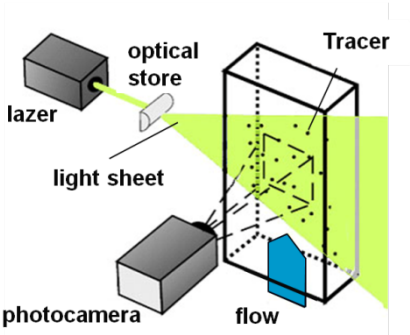

Fig. 2: PIV-diagnostic.

Experiments were carried out in the closed-circuit wind tunnel. The wind tunnel test section is 870 mm length. Contraction cone outlet diameter is 450 mm. The wind tunnel is equipped with the water-air heat exchanger for maintaining of constant flow temperature. Free-stream temperature T_∞ and velocity W_∞ were measured by Testo 435-2 multifunction HVAC and IAQ meter. The longitudinal turbulent intensity was found to be less than 0.5 %. To obtain velocity field PIV system POLIS with the "ActualFlow" software application were used [1]. Heat flux was measured by gradient heat flux sensor (GHFS) invented at Peter the Great St.Petersburg State Polytechnic University (Russia) [2].

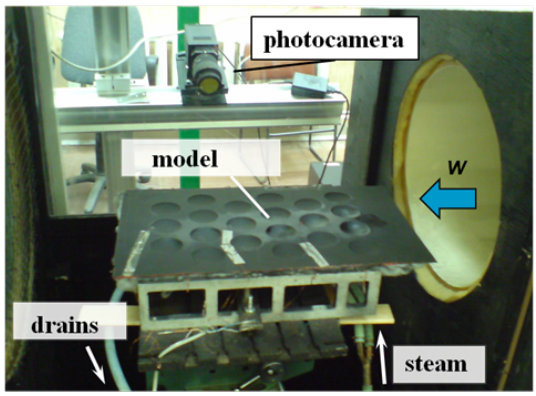

Fig. 3: Working section.

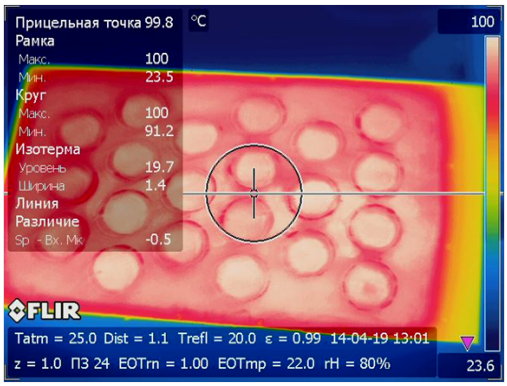

Fig. 4: Image from FLIR.

The operating principle of a GHFS [2] is based on a transverse Seebeck effect: when heat flux transits through a plate with anisotropy of thermophysical and thermoelectric properties, the thermo-electromotive force (thermo-EMF) occurs. Its direction is normal to heat flux vector and proportional to heat flux rate. When the process is non-stationary thermo-EMF is formed in a thin skin layer of GHFS body (Fig. 1).

The response time of our GHFS is about $10^{-8}…10^{-9}$ s, that allows to consider GHFS almost free from transit-time effects heat flux measurement unit. We used the GHFS made of a single crystal of bismuth, 99.99% pure. Sensor plan form dimensions were 2 × 2 mm, thickness was 0.2 mm, its volt-watt sensitivity was 11.6 mV/W. Sensor's signal was measured by the specially improved light beam galvanometer.

A model had a form of the hollow plate covered with spheric dimples. Volume relationship *h*/*D* was 0,2, diameter *D* was 62 mm. The distance between the dimples longitudinally and in across-track direction was alike and totaled 7 mm (Fig 3). Model was made of brass and steel sheets of 0,2..0,4 mm. The model was heated with the steam with temperature close to 100°C. Isothermality of the dimpled surface was controlled by IR camera FLIR P640 (Fig 4).

We have measured heat-flux per unir area in the dimples possessed from second to sixth chain. Fig. 5 Illustrates dependence of non-dimensional heat transfer coefficient inside the dimples. Heat transfer coefficient of i^{th} chain is proportional to that one of 2^{nd} chain. Heat ransfer coefficient decreases with number of the chain. Processes in low Reynolds numbers (2100 and 4500) were differed from others. This fact can be connect to strong impact of natural convection.

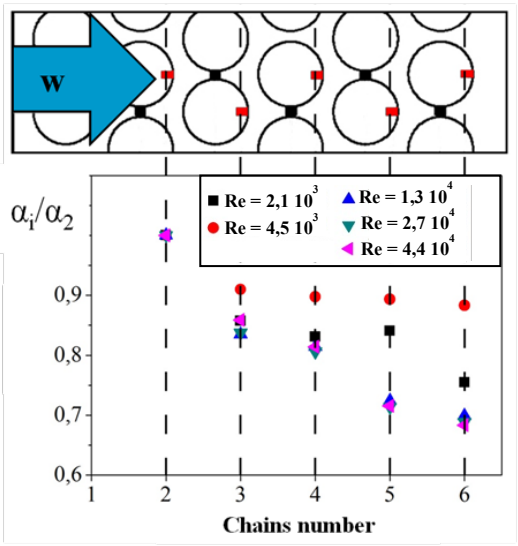

Fig. 5: Heat-transfer coefficient.

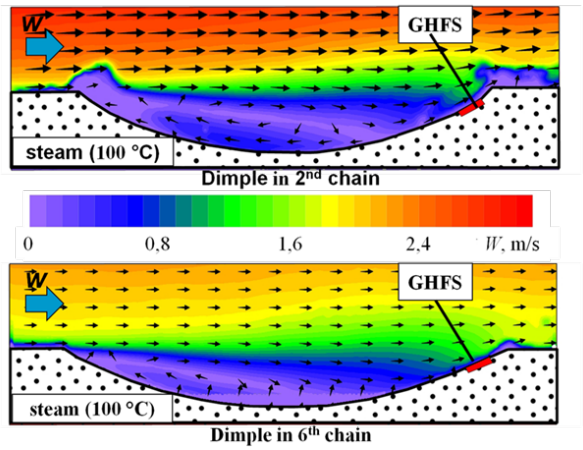

Fig. 6: Velocity fields.

As is shown in literature [2, 3], the largest heat transfer coefficient on the dimple's back edge is measured up where back streaming was strong. Fig. 6 illustrates the velocity fields for dimples on 2^{nd} and 6^{th}chains for Re = $1{,}3 \cdot 10^4$. However, midrange magnitude of velocity near the sensor altered slightly, back streaming side decreased great. This fact shows that the side of eddy generation inside dimple becomes smaller and heat transfer coefficient declined.

References

[1] «POLIS» velocity profile measuring instrument [website]/ Institute of Thermophysics SB RAS, Novosibirsk – access mode: http://eng.polis-instruments.ru/

[2] Sapozhnikov, S. Z., Mityakov, V. Y., Mityakov, A. V., 2013, Gradient heat flux measurement basic concepts, St. Petersburg State Polytechnical University, Saint Petersburg (in Russian).

[3] S.Z. Sapozhnikov, V.Yu. Mityakov, A.V. Mityakov, Gradient Heat Flux Sensors in Heat Engineering Experiments, Polytechnical University Publisher, SaintPetersburg, 2007, 202 pp.

Design and development of a measuring instrument for verification of technical and optical thin-layer materials by advanced reflectance spectroscopy

D. Steinhäußer[1], R. Kaschuba[1], Th. Seeger[2]

[1]Faculty of Engineering and Mathematics, Bielefeld University of Applied Sciences, 33619, Bielefeld, Germany
[2]Institute of Engineering Thermodynamics, University of Siegen,57076, Siegen, Germany

Authors e-mail address: Dominik.Steinhaeusser@fh-bielefeld.de

Design the algorithm compensation of vignetting error at optical-electronic autoreflection system by modelling vignetted image

A. Sakhariyanova[1], I. Konyakhin[1]

[1]ITMO University, 197101, Saint-Petersburg,, Russian Federation

Authors e-mail address: sakhariyanova@gmail.com

Abstract

During the installation and operation of large-scale objects, need to use angle measurement devices, such as optical-electronic autocollimators, which allow to control the deformation of objects [1-2]. The reasons for such deformations are own weight structures, as well as external weather conditions. After considering the optical-electronic autocollimators on the market [3-4], can conclude that these autocollimators have insufficient distance measurement (up to 5 meters), one of the reasons of the limited distance is error due to vignetting of the reflected beam, because with increase in the measurement range, accuracy of the measurement is reduced, because there is no means of compensating beam vignetting.

When the reflector turns an angle β due to the unequal vignetting of the reflected beam occurs asymmetrical redistribution irradiance of image in the plane of the autocollimator analyzer. As a result, the energy axis of the image shifts relative to the geometrical axis. As CCD fixes displacement of the energy center of image, and measured rotation angle of reflecting system is proportional to the displacement of geometry center, as vignetting leads to measurement error [5].

Autocollimator beam has a complicated structure shown in Figure 1, there are the two areas – internal and external. The internal area is limited by a conical surface formed by the rays 4, 6 from the extreme points of the radiating mark that are directed to the optical axis of objective. The Lф distance from center of the exit pupil of the objective to the point K - the distance beamforming. From the outside, external area is limited to the conical surface formed by the extreme rays 3, 5 from the extreme points of the radiating mark, and the inside - internal conical surface. The cross section of collimator beam by plane which perpendicular to the optical axis of the objective has circular I and annular II zones.

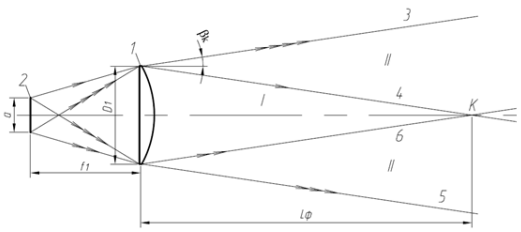

Fig 1. Structure of autocollimation beam: 1 – objective, 2 – the radiating mark, 3-6 – extreme rays, I – circular zone, II – annular zone

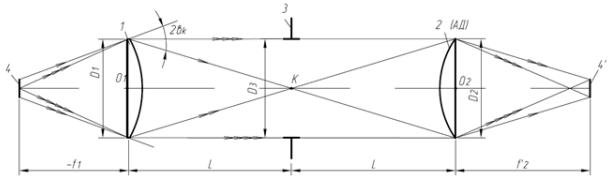

Fig 2. Autoreflection scheme: 1-4 - diaphragms that define light diameters of radiating and receiving objectives, reflector, radiating mark; 4' – image of diaphragm-mark at the receiver; АД – aperture diaphragm

For increasing the measurement distance autocollimator should be considered a variant of the scheme where distance of location aperture diaphragm longer Lф distance, such measurement scheme called autoreflection scheme shown in Figure 2. The advantage of this scheme is increase the distance measuring autocollimator, and when turn the mirror in the process of measuring it occurs monotonically increasing error that can be compensated [6].

In this scheme, the distribution of the irradiance in the image described by a function of the following form [7]:

$$E(r) = \frac{2}{\pi}(\arccos(\gamma(r)) - \sqrt{1-(\gamma(r))^2} \cdot \gamma(r)), \quad (1)$$

$$\gamma(r) = \frac{2 \cdot L}{D \cdot f} \cdot r,$$

where r — the radius that defines the position of the point mark – in fact, the coordinate of a point on the axis OY. Computer original model based on this formula (1) shown in Figure 3.

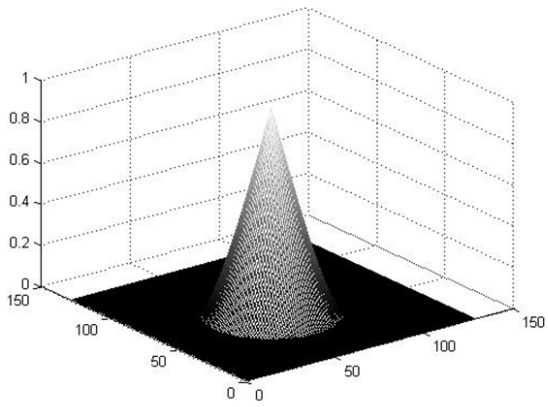

Fig 3. Original computer model of image

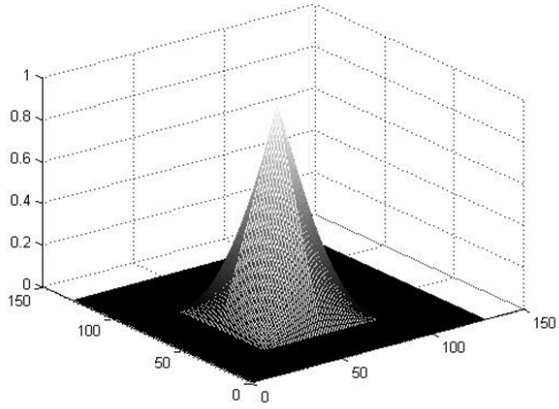

Fig 4. Approximated computer model of image processing

Because of the complexity of the analytical description of the vignetting processes proposes the use of computer model shown in Figure 4. The simulation based on approximation according to which each point of the finite image of a source of radiation essentially is the focused area of intersection of the entrance pupil and the elementary beam reflected by a mirror, and its energy is proportional to integral (the general energy) on this area.

As shown in Figure 4 model matrix analyzer is built as an array of pixel sensitivity *A (128,128)*. The model image on analyzer is built in the form of a circle array *B (64,64)* and values of the elements in the array center is equal to 1. Other values of the array elements are reduced to zero by the end of the array in accordance with the function $E(x, y) = (1 - |x|) \cdot (1 - |y|)$ where *x, y* ranges from 0 to 1, where 0 matches the center of the array, and 1 – the edge of the array. By comparing the approximate computer model with the original found that deviation is an insignificant, because the difference between the models does not exceed 0.1%, and this model can be used in further research.

For constructing systematic error compensation algorithm was reviewed three cases of displacement vignetting area on matrix analyzer due to the rotation control element (mirror). Based on the received dependences, it is seen that the vignetting error for the first case equal to 0.5 % (0.08 CCD pixel), and for the second case, the error is 16% (2.6 CCD pixel). Using this algorithm compensation systematic error due to vignetting reduced to a negligible value, that allows to increase the working distance of commercially available autocollimators in 1.2-1.5 times.

Acknowledgements: This work was financially supported by Government of Russian Federation, Grant 074-U01. The authors thank in particular the Erlangen Graduate School in Advanced Optical Technologies (SAOT) and Medical Valley EMN.

References

[1] Turgalieva, T. V. and Konyakhin, I. A., "Research of autocollimating angular deformation measurement system for large-size objects control," Proc. SPIE 8788, 878832 (2013).

[2] Konyakhin, I. A., Petrochenko, A. V., and Tolochek, N. S., "Optic-electronic system for deformation of radio-telescope counter-reflector computer modeling," Proc. SPIE 9131, 91311O (2014).

[3] "TriAngle electronic autocollimator," <http://www.trioptics.com/triangle/description.php> (24 December 2015). www.trioptics.com

[4] "Electronische autokollimatoren," <http://www.moeller-wedel-optical.com/produkte/elektronische-autokollimatoren> (24 December 2015). www.moeller-wedel-optical.com

[5] Konyakhin, I. A., Sakhariyanova, A. M., Smekhov A. A., "Investigation vignetting beams in optoelectronic autocollimation angle measurement system," Proc. SPIE 9526, 95260H (2015).

[6] Konyakhin, I. A., Polyakov, V. M., Vorona, A. M, "Research on the Methods to Compensate the Systematic Error at Optical Autoreflection Angular Measurements," Journal of Physics, Papers 48(1), 932-936 (2006).

[7] Liu Lei, Koniakhine, I. A, "Research on the methods to reduce the error in autocollimation angular measurements," Proc. The Third International Symposium on Instrumentation Science and Technology, 385-389 (2004).

[8] Anisimov, A. G., Pantyushin, A. V., Lashmanov, O. U., Vasilev, A. S., Timofeev, A. N., Korotaev, V. V., & Gordeev, S. V., "Absolute scale-based imaging position encoder with submicron accuracy," Proc. SPIE 8788, 87882T (2013).

Crosstalk and methods for its reduction in the inline fiber optic sensor array

A. Volkov, M. Plotnikov, M. Mekhrengin, I. Deyneka, I. Sharkov
ITMO University, 49 Kronverksky Pr., 197101, St. Petersburg, Russia
Authors e-mail address: avvolkov9223@gmail.com

Abstract

This paper presents a mathematical analysis of the PGC-scheme output signal distortions based on a crosstalk influence. Conventionally, the inline fiber optic sensor arrays are used in geophysical explorations, underwater security systems, multifunction sonar systems, seismic stations [1]. But those sensor systems are usually based on a fiber Bragg gratings (FBG), which results in the appearance of crosstalk impulses [2,3]. The principle scheme of the inline fiber optic array based on two sensors and timing diagrams are illustrated in Fig. 1.

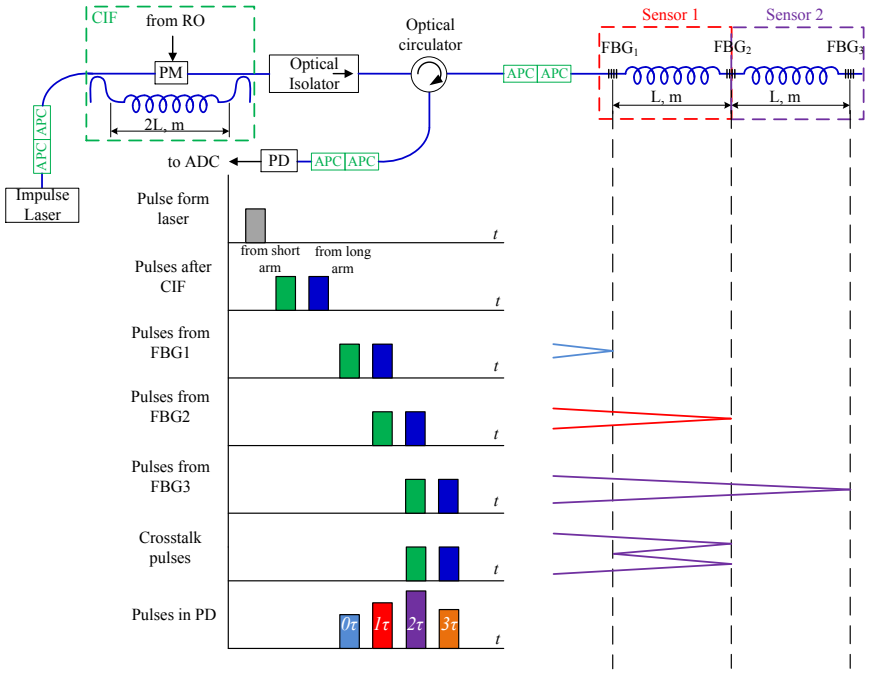

Fig. 1: The principle scheme of inline fiber optic array based on two sensors and timing diagrams

According Fig. 1, the laser produces the light impulse, which propagates along the fiber and arrives on the compensating interferometer (CIF). The light impulse splits on two pulses: the first pulse passes through a phase modulator in the short arm of the interferometer, the second pulse goes through the long arm of the interferometer equal to the double length of the sensor. As shown in the timing diagram the first pulse is marked with green color and the second pulse is indicated with blue color. There are two pulses after the CIF that does not overlap each other because of the path difference in the CIF. After that, pulses pass into sensor array, where they reflect from the first FBG successively. Two transmitted pulses go through the sensing fiber and are divided in two groups: the first one is reflected from the second FBG and the second one is transmitted through the second FBG. Impulses from the third FBG are produced in the same way. Further, pulses from the long arm of the interferometer which are reflected from the previous FBG and pulses from the short arm which are reflected from the current FBG will interfere. Interferometric impulses will be formed. Those pulses will arrive at the photodetector (PD) in the different time slots and will contain the measured phase signals from the sensing fiber. However, the interferometric pulse at the 2τ time slot is produced by three pulses. The two of those impulses are generally called as primary pulses [3,4], because they are reflected only one time from the second and the third FBG respectively and contain phase signals from the sensors. The third pulse reflects three times: one time from the second FBG and two times from the first FBG, it's usually named as crosstalk pulse. Thereby, this pulse comes on the PD at the 2τ time slot. So the interferometric pulse at the 2τ time slot can be represented as:

$$I(2\tau) = I_2 + I_3 + I_{cr} + 2\sqrt{I_2 I_3}\cos(\varphi_3 - \varphi_2) + 2\sqrt{I_{cr} I_2}\cos(\varphi_{cr} - \varphi_2) + 2\sqrt{I_{cr} I_3}\cos(\varphi_{cr} - \varphi_3) \quad (1)$$

where $I(2\tau)$ - the interferometric pulse light intensity at the 2τ time slot, I_2 - the primary pulse light intensity reflected from the second FBG and passed through the long arm of the interferometer, I_3 - the primary impulse light intensity reflected from the third FBG and passed through the short arm of the interferometer, I_{cr} - the

crosstalk impulse light intensity reflected three times, φ_2 , φ_3 and φ_{cr} - the phases of two primary pulses and the crosstalk pulse respectively.

As can be seen, the interferometric impulse at the 2τ time slot contains three components with different phase differences. Only one of them comprises the measured phase signal from the second sensor. Other components contain the measured phase signal from the first sensor and the phase difference between phase signals from the first and the second sensors. After the PD signals are digitized by the ADC, and then they pass into the demodulation scheme PGC-Atan [5,6].

The primary goal of this study is the mathematical analysis and simulation of the crosstalk influence on the output signal from the PGC-Atan algorithm and methods for its reduction in the inline fiber optic sensor array. MATLAB software environment was used for modeling crosstalk influence on the output signal and methods for its reduction, and the FDATool module (Filter Design and Analysis Tool) was used to create digital finite impulse response filters (FIR), as well as Simulink environment was used to create the waveform of reflected pulses. All mathematical transformations of investigated algorithms were described using a scripting language of MATLAB environment.
Output signals from sensors after the PGC-Atan demodulator are shown on the Fig. 2.

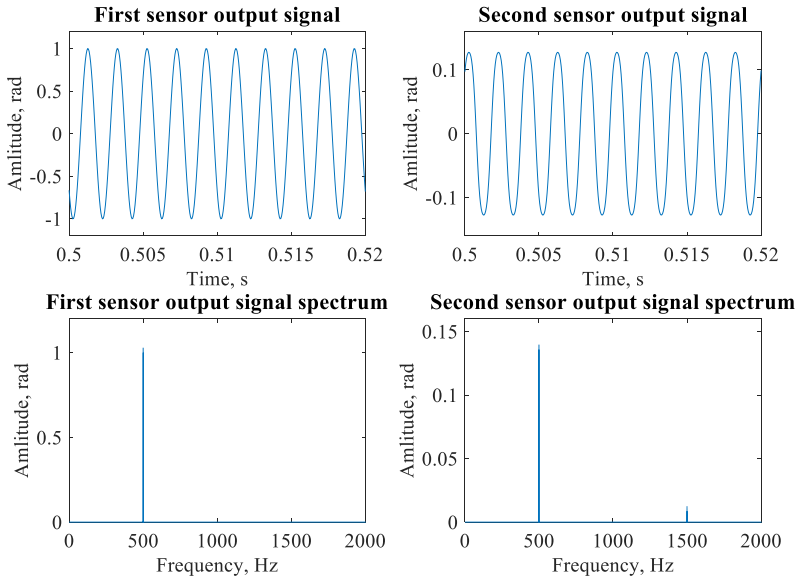

Fig. 2: The outputs sensors signals and their spectra

During the simulation, the phase signal with the amplitude 1 radian and the frequency 500 Hz was applied to the first sensor. Nothing was applied on the second sensor. However, as shown in Fig. 2, the crosstalk phase signal at 500 Hz with the amplitude of 13.56% from the original signal amplitude was received on the second sensor due to the impulse multi-reflection effect.

References

[1] S. Yin, P. B. Ruffin, F. T. S. Yu. 2008. Fiber Optic Sensors, 2nd ed. - Pennsylvania State University. CRC Press Taylor & Francis Group.

[2] A. D. Kersey, K. L. Dorsey, and A. Dandridge. 1989. Crosstalk in a fiber-optic Fabry–Perot sensor system with ring reflectors. Opt. Lett., vol. 14, no. 1, pp. 93–95, Jan.

[3] Lu Yang, Meng Zhou. Methods of reducing TDM crosstalk in an inline FBG based Fabry-Perot sensor. 2011. Proceedings of SPIE - The International Society for Optical Engineering 8194, 81942U , June.

[4] Huizu Lin, Lina Ma, Zhengliang Hu, Qiong Yao, and Yongming Hu. Multiple Reflections Induced Crosstalk in Inline TDM Fiber Fabry-Perot Sensor System Utilizing Phase Generated Carrier Scheme. 2013. Journal of Lightwave Technology, Vol. 31, No. 16, Aug.

[5] Timothy R. Christian, Philip A. Frank, and Brian H. Houston. 1994. *Real-time analog and digital demodulator for interferometric fiber optic sensors*. Proc. SPIE 2191, Smart Structures and Materials: Smart Sensing, Processing, and Instrumentation, 324, May 1.

[6] Liwei Wang, Min Zhang, Xianhui Mao, Yanbiao Liao. 2006. *The Arctangent Approach of Digital PGC Demodulation for Optic Interferometric Sensors*. Proc. of SPIE Vol. 6292, 62921E.

Compensation of thermal effect in fiber-optic gyroscope signal using artificial neural networks

D. Smirnov[1], E. Gareev[1], Ph. Shuklin[1], N. Kikilich[1], V. Kozlov[1]

[1]*Saint Petersburg National Research University of Information Technologies, Mechanics and Optics, 197101, Saint Petersburg, Russia.*

Authors e-mail address: daniil_smirnov@yahoo.com

Abstract

Fiber-optic gyroscope (FOG) is a device that measures the angular velocity. It is widely used in navigation systems as well as systems used in the orientation and position stabilization of objects in space. FOG operating principle is based on Sagnac effect. Basic FOG sensing element is the optical fiber coil (depending on the necessary parameters FOG fiber length can be up to several kilometers). Angular velocity is estimated by measuring the difference between the phases of the beams propagating in two opposite directions through the fiber (Fig. 1). Changing environmental conditions affect the optical characteristics of the main elements of the FOG, which can lead to spurious phase difference, i.e. incorrect detecting of angular velocity magnitude. According to [1-5] the temperature is one of the most important factors influencing the accuracy of FOG, so the thermal drift is necessary to take into account for designing FOGs with desired navigation accuracy.

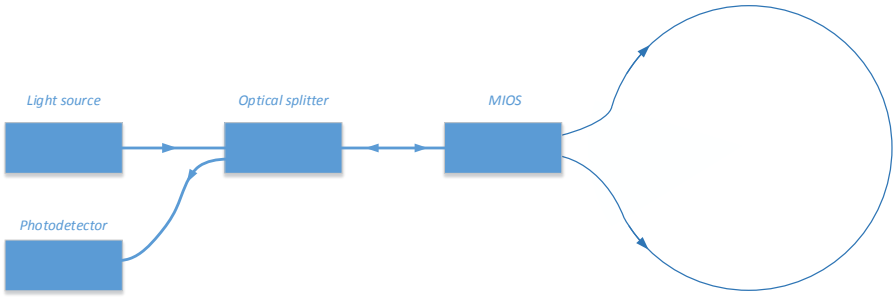

Fig. 1. Basic scheme of FOG using Sagnac effect.

In a large number of Russian and foreign works published over the last decade authors describe the successful use of neural networks in solving problems that are difficult to formalize and algorithmization of systems with unexplained behavior in various fields of science and technology. There are new scientific publications describing the current theories and approaches to the construction of artificial intelligence and neural networks. Analysis of these publications suggests the high prospectivity of neural networks usage in the instrumentation, particularly in the problems of temperature drift compensation.

In this paper, we consider the use of neural networks in the problem of compensation for the thermal effects on FOG.

Artificial neural network (ANN) is a mathematical model based on the principle of biological neural networks. By analogy to biological networks, ANN consists of mathematical neurons, each of which is a set of weighted inputs and one output. The output value is calculated as nonlinear function (activation function) of the sum of products of input values and the corresponding weighting coefficients. Various tasks can be solved by using different types of networks, that can be designed by recombining neurons between themselves and changing activation function (Fig. 2). The weighting factors are calculated using a learning algorithm.

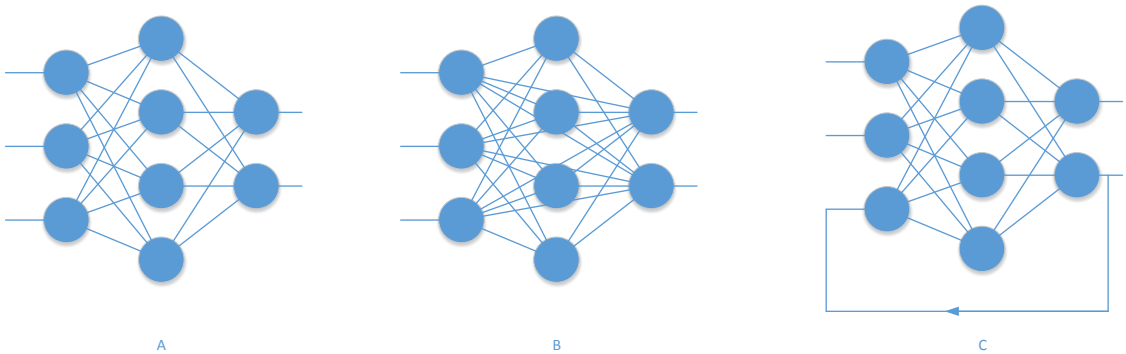

Fig. 2. Different types of artificial neural networks: perceptron (A), neural network with full connections (B), recurrent neural network (C).

For compensation of thermal drift temperature sensors were installed in different parts of the coil. This allows to check not only average temperature of the whole device, but also to check all main temperature gradients inside the coil.
To investigate the thermal fields in FOG it was placed inside the heat chamber where temperature varied by different pre-defined laws in a given range. Despite the fact that the device has been installed on a fixed base a variation of FOG signal was observed. FOG signal variation in this experiment represents a mistake induced by temperature drift. Data sets were recorded several times and separated into training sets and test sets. First ones are used to teach network to calculate the error depending on the temperature. Then, test sets were used to check quality of network calculations. The results of this study are presented in the work.

References

[1] Lefevre H. The Fiber-Optic Gyroscope UK — London: Artech House, 1993. — P.314.
[2] Golikov A.V.,"Temperature error of fiber-optic gyroscopes," Saratov, Dis. candidate. tehn. sciences 2001.
[3] Listvin V.N., Logozinsky V.N.[fizoptika] URL: http://www.fizoptika.ru/describtion/book_bind.pdf
[4] Galyagin K.S., Kiselev E.V. Oshivalov M.A., Ulrich T.A., Vakhrameev E.I.Thermal drift of fiber-optic gyroscope // engineering. — №1. — 2011. — pp. 32-37
[5] Dzhashitov V.E.; Pankratov V.M.Sensors, Instruments and systems aerospace and marine instrument in terms of thermal effects; ISBN 5-900780-57-0 Russia — Saint Petersburg: Concern CSRI Elektropribor, JSC, 2005.

Three colour coherent anti-Stokes Raman spectroscopy for thermometry in sooting flames

Ch. Meißner[1], J. W. Tröger[1,2], F. Beyrau[4], D. N. Kozlov[5], Th. Seeger[1,2,3]

[1]*Engenieering Thermodynamics, University of Siegen, 57076 Siegen, Germany*
[2]*Erlangen Graduated School in Advanced Optical Technologies (SAOT), University of Erlangen Nuremberg, 91052 Erlangen, Germany*
[3]*ITMO University Saint Petersburg,197101 Saint Petersburg, Russia*
[4]Engenieering Thermodynamics, *Otto-von-Guericke University Magdeburg, 39106 Magdeburg, Germany*
[5]*A.M. Prokhorov General Physics Institute, Russian Academy of Sciences,119991 Moscow, Russia*

Authors e-mail address: christian.meissner@uni-siegen.de

Abstract

Laser-based measurement techniques are powerful tools for the investigation of complex combustion processes because information about temperature and species concentrations can be generated non-invasive with a high local and spatial resolution. One of these tools is coherent anti-Stokes Raman scattering (CARS) which has often been used for temperature measurements even in harsh combustion systems (see e.g. [1, 2]). For sooting flames well-known problems are interferences between the C_2-radical absorption/emission lines and the vibrational CARS signal at a wavelength of around 473 nm, the usual N_2 signal-wavelength when a frequency-doubled Nd:YAG laser is applied. This interaction of the C_2 Swan bands and the vibrational CARS signal leads to a falsification of measurement results and a significant error in temperature determination [3].

To overcome this problem, different CARS setups have been proposed in the past [4-6]. The rotational CARS approach has already been used for thermometry in sooting flames [4]. Nevertheless it is well known that the accuracy and precision for rotational CARS temperature measurements at flame temperatures is not as good as for vibrational CARS [7]. An alternative is the relatively complex dual-pump vibrational CARS approach. Such a setup is equipped with an additional narrowband dye laser which leads to a frequency shift of the vibrational CARS signal [5]. For the so called *three colour* or *shifted* vibrational CARS approach also an additional narrowband dye laser is necessary [6]. Such a narrowband dye laser is expensive, needs maintenance and is not easy to realize for ps-laser excitation.

In this work, we propose a novel setup for vibrational CARS thermometry in sooting flames, where a Nd:YAG laser pumped Raman crystal is used as an additional narrowband light source. Such Raman crystals have been investigated in the past for several applications [8, 9] even for combustion diagnostics [10]. Nevertheless, this is the first application for CARS thermometry. An undoped potassium gadolinium tungstate ($KGd(WO_4)_2$) is tested as a narrowband light source in a shifted vibrational CARS setup. With this setup Temperature measurements were performed in a laminar sooting ethylene/air flame established on a McKenna burner. The results were compared to standard vibrational CARS and rotational CARS temperature measurements.

The three colour CARS setup is based on three light sources. One part of a narrowband frequency-doubled, picosecond pulsed Nd:YAG solid state laser is used in the CARS process and one part is used as a pump source for a broadband dye laser. Additionally a third part of the frequency doubled Nd:YAG laser beam is used to pump a $KGd(WO_4)_2$ Raman crystal. The output wavelength of the $KGd(WO_4)_2$ Raman crystal is 558 nm. This narrowband laser beam was used as a second pump beam in the vibrational CARS process resulting in a N_2 vibrational CARS signal at 494 nm. The polarization of the three laser beams are controlled by Glan-air polarizers. The phase matching condition was realized by an USED-CARS geometry. Therefore a hole mirror was placed into the Nd:YAG laser beam to create a donut-like beam profile. The inner part of the Nd:YAG laser beam crossing this hole mirror is used for pumping the dye laser and the Raman crystal. A dichroic mirror separated the first Stokes emission of the Raman crystal which was used in the CARS process from the pump beam. Higher stokes orders were separated by a short pass filter. All three laser-beams were focused with a lens with a focal length of f = 100 mm. The laser beams and the generated CARS signal were collimated by a further lens (f = 100 mm). Due to the USED-CARS geometry it was possible to generate the standard vibrational, the three colour vibrational and the rotational CARS signal simultaneously. Dichroic mirrors were used to separate the signal beams from the three laser beams. For rotational CARS a polarization scheme was used to suppress the smeared vibrational CARS signal. A half-wave plate in the detection path allowed to align the polarization of the CARS signal for maximum efficiency of the spectrometer. The CARS signals are finally focused on the entrance slit of the spectrometer and recorded by CCD camera. The flame measurements were performed in a laminar sooting ethylene/air flame established on a McKenna flat-flame burner. The equivalence ratio for the ethylene/air mixture was 2.3. An outer co-flow of air of 15 l/min was used to stabilize the sooting flame. The potential of this shifted vibrational CARS setup based on a $KGd(WO_4)_2$ Raman crystal is demonstrated in a sooting ethylene/air flame. As an example two shifted vibrational CARS spectra taken in room air and in the

laminar ethylene/air flame are shown in Figure 3 together with the corresponding best fitting theoretical spectrum.

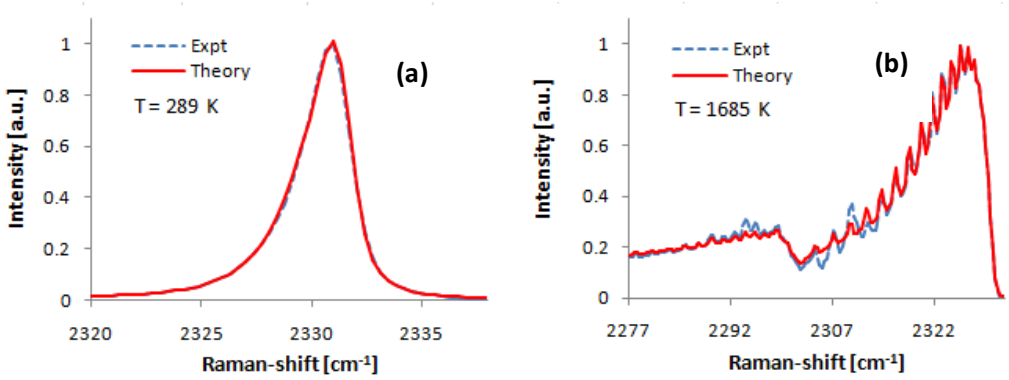

Figure 3: Shifted vibrational CARS spectra taken in room air (a) and in a laminar sooting ethylene/air flame (ϕ = 2.3) (b) with their corresponding best fitting theoretical spectrum.

For comparison temperature profiles were taken for all three different CARS techniques. In Figure 4 the temperature mean values of 1000 single shot measurements are shown for standard vibrational CARS, rotational CARS and three colour vibrational CARS. The temperature profiles for rotational and three colour vibrational CARS are in excellent agreement. The standard vibrational CARS measurements are obviously influenced by C_2 interferences.

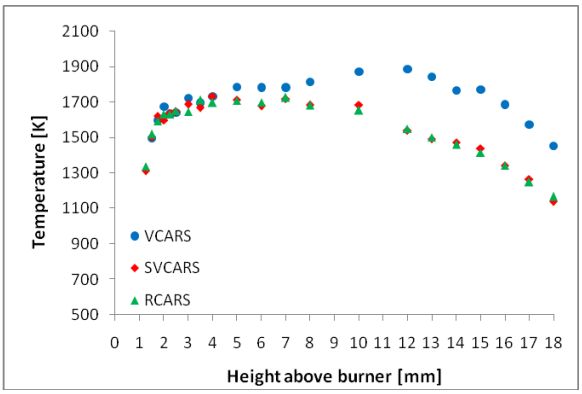

Figure 4: Temperature profiles of an ethylene-air flame (ϕ = 2.3) for the CARS approaches; standard vibrational CARS (VCARS), three colour vibrational CARS (SVCARS) and dual-broadband pure rotational CARS (RCARS)

References

[1] L. E. Harris, M. E. McIlwain, Combust. Flame, **48**, (1982), 87
[2] M. Aldén, S. Wallin, Appl. Opt., **24**, (1984), 3434
[3] A. Malarski, F. Beyrau, A. Leipertz, J. Raman Spectrosc., **36**, (2005), 102
[4] P.-E. Bengtsson, L. Martinsson, M. Aldén, S. Kröll, Combust. Sci. Technol., **81**. (1992), 129
[5] F. Beyrau, T. Seeger, A. Malarski, A. Leipertz, J. Raman Spectrosc. **34**, (2003), 946
[6] M.S. Tsurikov, K.P. Geigle, V. Krüger, Y. Schneider-Kühnle, W. Stricker, R. Lückerath, R. Hadef, M. Aigner, Combust. Sci. Technol., **177**, (2005), 1835
[7] T. Seeger, A. Leipertz, Appl. Opt., **35**, (1996), 2665
[8] A. Z. Grasiuk, S. V. Kurbasov, L. L. Losev, Opt. Commun., **240**, (2004), 239
[9] P. G. Zverev, J. T. Murray, R. C. Powell, R. J. Reeves, Opt. Commun., **97**, (1993), 59
[10] J. Kerl, T. Sponfeldner, F. Beyrau, Combust. Flame, **158**, (2011), 1905

Smart image selection algorithm in analysis plane of angle measuring sensor

A. Nogin, I. Konyakhin

Chair of Optical-Electronic Devices and Systems, ITMO University, 197101, Saint Petersburg, Russian Federation

Authors e-mail address: Rujusted@gmail.com

Abstract

This study presents a fully functional algorithm based on circle Hough transform which enabling to expand the metrological performance of the angle measuring sensor by addressing the problem of malfunction of the device when the marks overlapping. In order to increase the number of measured angles (two or three) in autocollimation angle measuring sensor used a control element is different from a flat mirror. These control elements increase the number of measured angles and the expense of the small ratio of the optical reduction improves the accuracy of the device, and in some cases even reduces its overall dimensions. However, when using such control elements, in the plane of the image analysis may happen marks overlapping which make it impossible to measure the angles. Application of the proposed algorithm significantly reduces the malfunction of the device and the area keeps functionality with the overlapping marks.

The study considered ready to use the algorithm allows solving the problem of inoperability autocollimation angle measuring sensor at the marks overlapping. The controlled object is a passive reflector, and on the base object is located autocollimator sensor. Sensor with the eyepiece attached to it for lighting grid and registering its reflection from the reflector on the object. This system is the most preferred because it does not require a power supply at the control point. It simplifies and reduce the cost of installation the entire system [1,2]. The sensor consists of emitting optic-electronics channel and a receiver with a microprocessor. Emitting channel generates an optical beam that falls on the reflector. Optical electronic receiver meant for registration of optical radiation from the control element and measuring its parameters, which determine rotation angles of the object. When the reflector element rotates on angles Θ_1 and Θ_2, the reflected beam has deviated from the original direction. As a result the image shifts on the matrix photo-receiver of the autocollimator. The microprocessor calculates video frames from the matrix photo-receiver and determines the shift of the image. Angular coordinates Θ_1 and Θ_2, of the reflector, are determined as a result of this processing. The initial stage of the calculation of the angles Θ_1 and Θ_2 is to determine the center of the marks registered by the system. Using the control elements different from a flat mirror creates a situation when in the image plane will mark overlap with each other. In this connection, the question arises what should be the distance between the centers of the marks in order to save serviceability and accuracy of the measurement system.

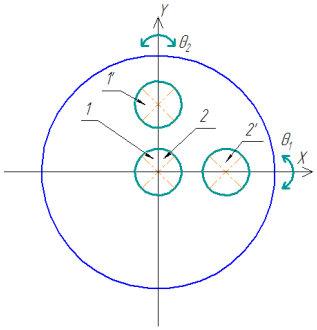

Fig. 1: The images on the photodetector matrix: 1, 2 – before the rotation of the reflector, 1 'and 2' - after the rotation.

To study the possible solution of this problem has been developed and implemented a model for the processing of overlapping arrays of irradiance in technology MatLab. This model has allowed to investigate the influence marks overlapping on the measuring accuracy of the coordinates. The algorithm is based on the idea to use the Hough transform. Hough Transform can solve the problem of determining the boundaries of the object with a strong image noise[3,5] and the problem of grouping boundary points by the use of particular voting procedures [4] to a set of parameterized objects in the image. This is particularly important when it is necessary to detect objects whose boundaries are crossed. For this purpose use the so-called Accumulation array that detects the presence of the required object. The dimension of the Accumulation array is equal to the number of unknown parameters of the Hough space. In the case of circular marks, the number of unknowns is equal to three. This will be the X and Y, and the radius of the mark that known to us only approximate or unknown at all. The algorithm is sufficiently flexible and can correctly measure the marks centres while ignoring the various parasitic

reflections, the inhomogeneity of the background and etc. For each point and its neighbours algorithm determines whether the weight of the boundary at this point is sufficient. This method is based on an assessment of the normal orientation of the voting contour points. The first step of the process is finding edge pixels surrounding the perimeter of the object. For this purpose used evaluation of the amplitude and direction of the gradient vector. The voting contour point is considered in terms of high modulus gradient. The second step for each edge pixel is used position estimate and the orientation of the circuit in order to evaluate the centre of a circular object of radius R by the movement over a distance R from the edge of the pixel in the direction normal to the contour (i.e. in the direction of the gradient vector). If this operation is repeated for each edge pixel will be found a variety of positions alleged points of the centre, which can be averaged to determine the exact location of the centre [6]. After that, we used a threshold filter and search of the local maximum in the accumulator array to determine the centres of the circles.

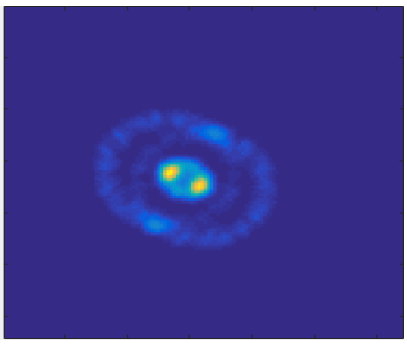

Fig. 2: Accumulation array

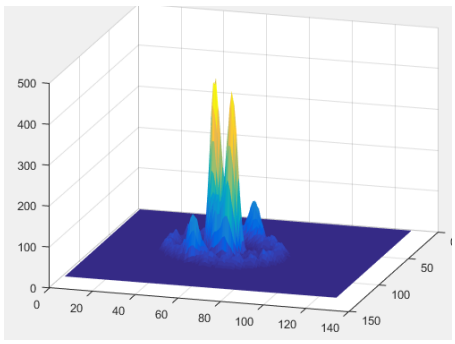

Fig. 3: 3D view of the accumulation array

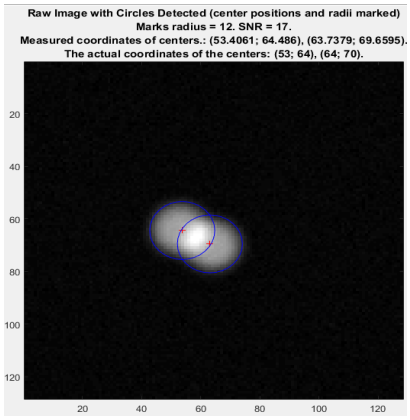

Fig. 4: Original image

In Fig. 2, and 3, is presented the accumulator array which is turned in the processing of the Fig. 4. This is clearly demonstrates how the algorithm working. The algorithm also passed the functional test, the result of which is displayed in the Fig 5, 6, 7.

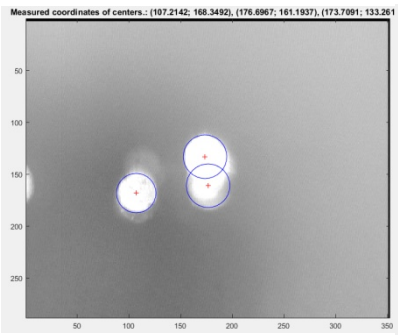

Fig. 5: Original image

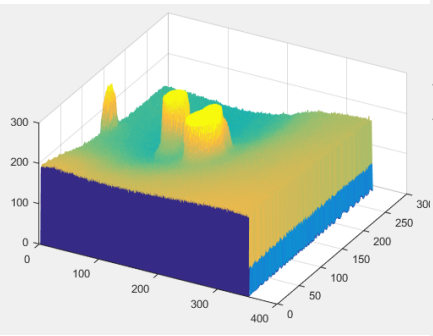

Fig. 6: 3D view of the original image

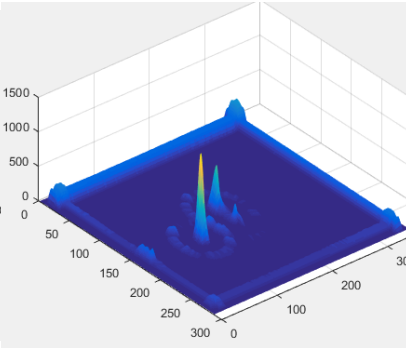

Fig. 7: 3D view of the accumulation array

Acknowledgements: This work was financially supported by Government of Russian Federation, Grant 074-U01.

References

[1] I Konyakhin, T Kopylova, A Konyakhin, 2012 Optic-electronic autocollimation sensor for measurement of the three-axis angular deformation of industry objects, *Proc. SPIE* **8439, 84391N**

[2] I Konyakhin, T Kopylova, A Konyakhin and A Smekhov, 2013, Optic-electronic systems for measurement the three-dimension angular deformation of axles at the millimeter wave range radiotelescope, **Proc. SPIE** *8759, 87593E*

[3] D.H. Ballard, 1981, *Generalizing the Hough transform to detect arbitrary shapes*, **13(2),** pp.111-112.

[4] L.A.F Fernandes, M.M. Oliveira, Real-time line detection through an improved Hough transform voting scheme, №41, pp.299-314, (2008).

[5] R. Gonzalez, R. Woods, S. Eddins, 2010, *Digital Image Processing Using MATLAB*

Implementation of an emission spectroscopy based sensor for engine testing

F. Feldhaus, I. Schmitz, Th. Seeger

Lehrstuhl Technische Thermodynamik, Universität Siegen, 57076 Siegen, Germany

Authors e-mail address: fabian.feldhaus@uni-siegen.de

Abstract

The current discussions about nitrogen oxide (NO_x) emission from diesel engines (CI engines) and high concentrations of NO_x in cities shows the need for action to reduce this emission. The reduction of NO_x is very important, because these pollutants have negative impacts on human health as well as on the environmental. Modern combustion engines need to fulfill increasingly stringent exhaust gas guidelines in the next few years (see e.g. [1]).
The entire engine combustion system has to be even further optimized, that their exhaust gas emissions remain below the ceilings given by different international gas guidelines. Therefore optical measurement techniques are an excellent tool and are used more and more [2]. The challenge of many optical measurement techniques is the usage of large optical windows to get access to the combustion chamber. Such modifications are not possible for production engines, because of their compact design. In this context the data acquisition needs to be obtained from technically unchanged engines. Such measurements are of utmost importance, because the achieved results can immediately be integrated in current developments. Consequently a stronger consideration of research especially on production engines is required for a better understanding of the internal combustion process, like mixture formation, temperatures etc.

The aim of this work is the further development of an new optical in-situ sensor system for technically unchanged combustion engines. The main parts of the ESS system are a probe head designed for in-situ measurements of the combustion chamber, an optical fiber and a spectrometer system. This emission spectroscopy bases sensor system (ESS) is able to detect light from the combustion process with a spectral range from UV to NIR simultaneously. The system setup offers the possibility to detect chemiluminescence signals as well as soot emission spectra, whose occurrence is typical for Diesel engines. In this case the corresponding soot emission spectra can be used to determine a integrated global combustion temperature based on a Planck´s law. The wavelength dependence of the complex refractive index of soot was taken into account using the expression given by MICHELSEN [3]. The accuracy of the sensor system was tested at a laminar premixed ethene/air flame ($\phi = 2.3$) and compared to measurements achieved by the coherent anti-Stokes Raman spectroscopy (CARS). The temperature difference was found to be less than 60 K. A first application test has been performed at a 1.6 l 80 kW PSA Diesel engine on a test bench. [4]
Now the ESS system has been integrated in the test bench control and measurement unit. Now the results of the emissions spectroscopy can be used to characterize the internal combustion process in addition to common measurement techniques like engine indicating, temperature measurement using thermocouples etc. Because thermocouples were installed in exhaust manifolds, they are only able to measure the temperature of the exhaust gas. It is obvious that the exhaust gas is cooler then the temperature of the internal combustion and because of that, this temperatures offer indirect information about the combustion process only. By contrast the ESS system detects light of the combustion during the combustion process. Because of that reason, the results of this measurement technique can be used for a characterization of the combustion directly.

References

[1] Commission Regulation (EU) No. 459/2012 of 29 May 2012, in Official Journal of the European Union, Volume 55, 2012
[2] Merker, Günter, Teichmann, Rüdiger, Combustion Engine Development, Springer Vieweg, Wiesbaden, 2012
[3] Michelsen, Hope A., Understanding and predicting the temporal response of laser-induced incandescence from carbonaceous particles, in: The Journal of Chemical Physics, Volume 118, 2003
[4] Feldhaus, Fabian, Schmitz, Ingo, Asbach, Sascha, Seeger, Thomas, Development and application test of an emission spectroscopy based sensor for IC engines, Sensorica, November, St. Petersburg 2012

Implantable Sensing Systems for Brain Signal Characterization and Measurement

Aimé Lay-Ekuakille[1], G. Griffo[1], P. Vergallo[1] **Keynote Lecture**

[1]*Department of Innovation Engineering, University of Salento, 73100 Lecce. Italy*

Authors e-mail address: aime.lay.ekuakille@unisalento.it

Abstract

The detection and treatment of strokes has an increasing interest not only for adults but also for children and young people. EEG (Electroencephalogram) recording is very essential for stroke understanding as well as epilepsy which is defined as the recurrent paroxysmal transient disturbance of brain function due to disturbance of electrical activity in the brain, where the disturbance is unrelated to infection or acute cerebral insult. The disturbances may be manifested as episodic impairment or loss of consciousness, abnormal motor phenomena, psychic or sensory disturbances, or perturbation of the autonomic nervous system. The main causes are the followings: In about 60% of cases (in developed countries) there is no known cause. Of the remaining 40%, the following are the most frequent: Head trauma, especially from automobile accidents, gunshot wounds, sports accidents, falls and blows at work or in the home; the more severe the injury, the greater the risk of developing epilepsy - Brain tumor and stroke - Poisoning, such as lead poisoning. Many people each year are reported to suffer seizures caused by alcoholism and pollution - Infection, such as meningitis, viral encephalitis, lupus erythmeatosus and, less frequently, mumps, measles, diphtheria and others - Maternal injury, infection or systemic illness affecting the developing brain of the fetus during pregnancy.

There are many attempts to block epilepsy reactions: pharmacological approach and hardware one. The second aspect is now very interesting since the first approach produces an addiction that leads to an inability of physiological organs to be able to accept drugs for a long time. The second approach is based on a sensing system which must be bio-implantable. Sensing devices and bio-implantability are a major gage for a correct acquisition and processing of EGG features [1] as indicated in Fig.1. Moreover the hardware approach allows also to design and fabricate implantable systems able to intervene as anti-surge for lowering and smoothing high peaks from strokes. The anti-surge model is the main scope of this paper and the system is located under the skull [2]. It is a complete system designed according to nanotechnology principles as depicted in Fig.2. This system, with dimensions of 3cm x 4 cm, is related to recording, transmitting and creating anti-surge reaction.

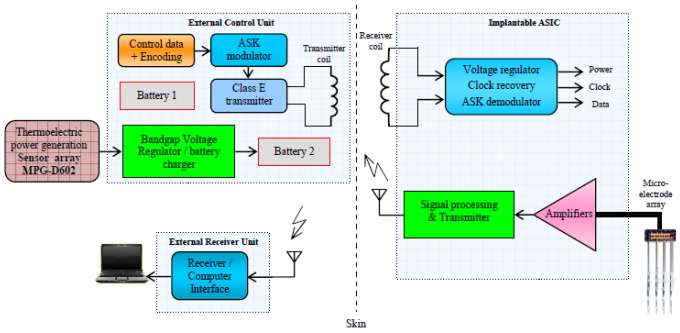

Fig. 1: A neurorecording system based on microtechnology [1].

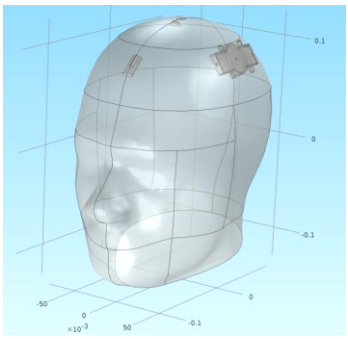

Fig. 2: Position of a the new implantable system.

The system hereby illustrated uses micro and nanotechnologies with some components in SMT but most of them are in nanotechnology. Once the signal, from nerves, is acquired, it is managed by a multiplexer (similar to ADG1408/ADG1409) [3]. A complex of 8 operational amplifiers or 2 quad-amplifiers (LM124 series) [4] is used to amplify the captured signal to be sent to the processing unit and system control that consists in a microcontroller PIC18F2XK20 series with nanowatt XLP Technology [5]. This microcontroller, once programmed in an appropriate way, is able to deliver a pre-stored counter-signal capable of blocking pre-ictal and ictal levels that provoke impairments to the person under test. The PIC (programmable interface controller) has a special configuration for this purposes. A Wi-Fi system, antenova A5839 [6], is used to transmit data to an external computer.

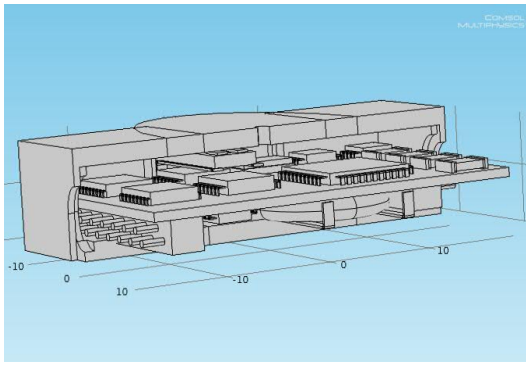

Fig. 3: Overview of the new implantable system.

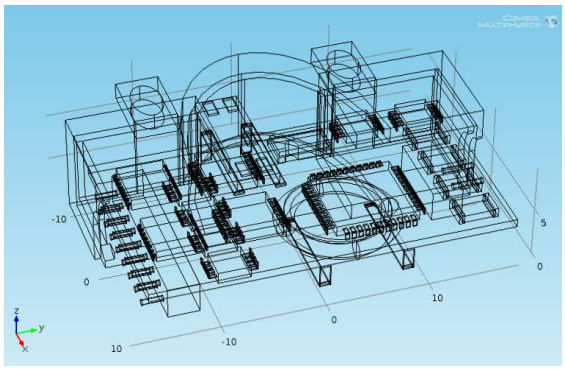

Fig. 4: 3D transparent view of some components.

The attention of this research is paid for sudden changes in brain electrical signals that could not be removed by pharmacological care because of resistance opposed by the epilepsy, for example refractory one. That is why there is a dedicated topic regarding RNS (Responsive Neuro Stimulator) [7] and VNS (Vagal Neuro Stimulator) [8]. We are working on the development bio-systems capable of recognizing an epileptic crisis during EEG registration and to stop it during its arising thanks to electrical pulses emitted by the bio-device (sensor) implanted in the cerebral cortex to follow the medical examination. This technique is generally called RNS (Responsive Neuro-stimulator). The main current troubles are due to crisis monitoring and cluttering. This latter could be due by excess of sensitivity. The RNS, implantable device, constantly monitors electrical activity of the brain, gets accustomed to what is normal for that patient and, when it detects activity that is abnormal, within a few milliseconds, sends out a small electrical stimulus to stop it. All electrodes are designed thanks to nanotechnology.

References

[1] G. Ben Hmida, A. Lay Ekuakille, A. Kachouri, H. Ghariani, And A. Trotta, Extracting Electric Power From Human Body For Supplying Neural Recording System, *International Journal on Smart Sensing and Intelligent Systems* (on line). Vol.2 n.2, pp.229-245, 2009.

[2] A. Lay-Ekuakille, G. Griffo, A. Massaro, F. Spano, G. Gigli, Experimental characterization of an implantable neuro-packaging for EEG signal recording and measurement, *Measurement*, Vol. 79, n.2, pp 321–330, 2016.

[3] www.analog.com/static/.../ADG1408_1409.pdf

[4] www.ti.com/lit/ds/symlink/lm124-n.pdf

[5] www.microchip.com/downloads/en/devicedoc/41303g.pdf

[6] www.antenova-m2m.com/.../956d970d6b2c8cc4d.

[7] R. Yadav, "Responsive Neuro Stimulator System: An implantable device to treat epilepsy", 2006, http://www.rxpgnews.com/epilepsy/Responsive_Neurostimulator_System_An_implantable_d_4966_4966.shtml

[8] M.S. George et al., Vagus Nerve Stimulation: A New Tool for Brain Research and Therapy, *Biol Psychiatry*, vol.47, pp.287–295, 2000

A new technique for processing the data obtained via sensors and detectors in X-ray computerized tomography

V. Sizikov, A. Serebryansky

Saint-Petersburg ITMO University, 197101, Saint-Petersburg, Kronverksky pr., 49, Russia

Authors e-mail address: sizikov2000@mail.ru

Abstract

The aim of this work is a further development of a stable technique for calculating X-ray tomograms on the basis of processing the data obtained by means of sensors and detectors. The technique is based on solving the 2-dimensional Fredholm integral equation of the 1st kind of convolution type instead of the traditional technique based on solving the non-standard Radon integral equation.

Introduction. On the basis of processing the data obtained via sensors, transducers and detectors, it is possible to perform a diagnostics and monitoring of medical and other objects. For example, in the X-ray computerized tomography (CT), data processing consists in solving the *Radon integral equation* [1–4]:

$$\int_{L(l,\theta)} c(x,y)\,ds = q(l,\theta), \qquad (1)$$

where $c(x, y)$ is desired substance density in some cross-section, $q(l, \theta) = -\ln[I(l, \theta)/I_0]$, I_0 is the intensity of the emitted tubes, $I(l, \theta)$ is the intensity on a detector, (x, y) are coordinates in fixed coordinate system connected with a substance, and (l, θ) are coordinates in rotating coordinate system connected with a frame containing tubes and detectors. Let us consider the parallel scanning.

Equation (1) is *non-standard*, since

- a kernel is absent,
- the integral is one-dimensional, but the functions $c(x, y)$, $q(l, \theta)$, $I(l, \theta)$ and $L(l, \theta)$ are two-dimensional,
- there are no explicit limits of integration,
- the integrand $c(x, y)$ depends on x and y, but the integration is performed over s along the line $L(l,\theta)$.

This creates difficulties when solving the Radon equation (1). Nevertheless, such methods of solutions have been developed as the *convolution and back projection method* in the form of filters of Ramachandran–Lakshminarayanan, Shepp–Logan, Troitskii, et al. [3], some of which have been implemented in commercial computerized tomographs.

Example. Fig. 1 shows an example of modeling the function $q(l, \theta)$ (direct problem) by means of MatLab-function radon.m [5] and obtaining the tomogram $c(x, y)$ (inverse problem) by means of m-function iradon.m [5] by the convolution and back projection method. We see, that the high-quality tomogram I is obtained.

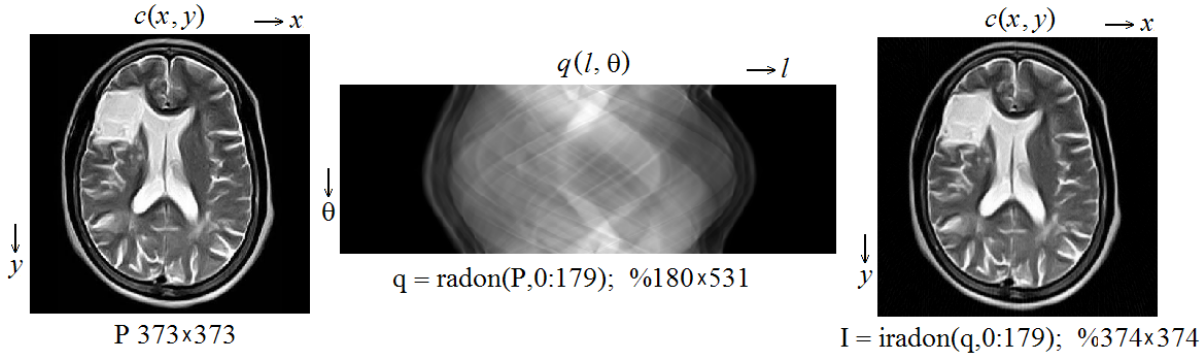

Fig. 1. P — initial density distribution $c(x, y)$; q — modeled function $q(l, \theta)$; I — obtained tomogram

The technique based on solving the Fredholm equation. In [1,2], non-standard Radon equation (1) has been transformed to standard two-dimensional first-kind Fredholm singular equation of convolution type [3,4]:

$$\int_{-\infty}^{\infty}\int_{-\infty}^{\infty} \frac{c(x',y')\,dx'\,dy'}{\sqrt{(x-x')^2+(y-y')^2}} = S(x,y), \qquad (2)$$

where

$$S(x,y)=\frac{1}{\pi}\int_0^{\pi} q(x\cos\theta+y\sin\theta,\theta)\,d\theta. \tag{3}$$

Equation (2) has a standard form. In it, the difference kernel is

$$K(x,y)=\frac{1}{\sqrt{x^2+y^2}}. \tag{4}$$

Solving equation (2) by the method of Fourier transform with regularization. Methods for solving equation of the type (2) are developed in detail [3, 4, 6, 7]. The main method is a method of 2-dimensional Fourier transform with Tikhonov regularization (since the problem for solving the equation (2) is ill-posed). According to this method, the solution of equation (2) is [3, 4]

$$c_\alpha(x,y)=\frac{1}{4\pi^2}\int_{-\infty}^{\infty}\int_{-\infty}^{\infty}\hat{c}_\alpha(\omega_1,\omega_2)\,e^{-i(\omega_1 x+\omega_2 y)}\,d\omega_1\,d\omega_2, \tag{5}$$

$$\hat{c}_\alpha(\omega_1,\omega_2)=\frac{\hat{K}(-\omega_1,-\omega_2)\hat{S}(\omega_1,\omega_2)}{|\hat{K}(\omega_1,\omega_2)|^2+\alpha\omega^{2p}}, \tag{6}$$

where $\alpha > 0$ is the regularization parameter, $p \geq 0$ is the regularization order, and

$$\hat{K}(\omega_1,\omega_2)=\int_{-\infty}^{\infty}\int_{-\infty}^{\infty}K(x,y)\,e^{i(\omega_1 x+\omega_2 y)}\,dx\,dy=\frac{2\pi}{\omega},\quad \omega=\sqrt{\omega_1^2+\omega_2^2}, \tag{7}$$

$$\hat{S}(\omega_1,\omega_2)=\int_{-\infty}^{\infty}\int_{-\infty}^{\infty}S(x,y)\,e^{i(\omega_1 x+\omega_2 y)}\,dx\,dy \tag{8}$$

are the Fourier transform (FT) of the kernel $K(x, y)$ and the right-hand side $S(x, y)$. Parameters α and p can be chosen by visual estimating tomogram, as well as by using different ways for their choice [6, 7].

Solution discretization. In practice, the foregoing continuous relations must be implemented in discrete form. To increase efficiency, we offer to take into account the following *conditions*:

1. One cannot connect the CFT and DFT in one program, namely, determine FT of $S(x, y)$ using the m-function fft2.m [5], i.e. use DFT (discrete FT), and determine FT of kernel $K(x, y)$ using analytical formula (7): $\hat{K}(\omega_1,\omega_2)=2\pi/\omega$, i.e. use CFT (continuous FT). One should calculate FT of $K(x, y)$ also in the form of DFT using the m-function fft2.m. Furthermore, the function K must be executed in the form of K(i,j), but not K(x,y), since the DFT uses only numbers of variables.
2. To speed up the computations, one should use a matrix M instead of m-function K.m (since MatLab is oriented to the matrix calculations).
3. When calculating the DFT, it is necessary to perform calculations on the so-called main interval $\omega\in[0,\omega_{\max}]$ [4] or even on the half-interval $\omega\in[0,\omega_{\max}/2]$.
4. The kernel $K(x,y)$ according to (4) may become infinite at $x = y = 0$, so we offer: $K(i,j)=1/\sqrt{i^2+j^2+\beta}$, where $\beta > 0$ is some small addition.

The use of these conditions appreciably improves a technique for tomogram calculating.

Software and the results of modeling. In the framework of the programming system MatLab, a software has been developed, namely, the main program IeFred2.m and m-function K.m for calculating the CT-tomograms via solving Fredholm equation (2) by method of 2-dimensional DFT and Tikhonov regularization. We also used the m-functions radon.m and iradon.m embedded into MatLab. With them, a series of tomographic images was calculated, their histograms were built, sharpness was increased, etc.

Fig. 2 shows the result of the *direct problem* solution, namely, calculating $S(x, y)$ according to (3) (in the discrete form), where $q(l, \theta)$ is taken from Fig. 1. Image S and its histogram are obtained. The image S is obtained pale. To improve it, the histogram alignment (equalization) is used with the help of m-function histeq.m [5]. We obtain the improved image Sh and its aligned histogram (Fig. 2).

Further, we solved the *inverse problem*, namely, tomogram calculating by solving Fredholm equation (2) by two-dimensional FT and Tikhonov regularization according to (3)–(8). Fig. 3 shows regularized tomographic image (tomogram) $c_\alpha(x, y)$ according to (5) and its histogram, as well as the improved tomogram $c_{\alpha h}(x, y)$ at the expense of histogram equalization.

Conclusion. Comparison of the results shown in Fig. 1 (solution of Radon equation (1)) and in Fig. 2–3 (solution of Fredholm equation (2)) leads to the following conclusions.

1. The original function $q(l, \theta)$ is completely different from the desired solution $c(x, y)$ (Fig. 1), and $S(x, y)$ (Fig. 2) is image $c(x, y)$ diffused by the function $1/\sqrt{x^2+y^2}$, therefore, $S(x, y)$ is like $c(x, y)$ (though with a diffusion) and $S(x, y)$ is a good initial approach to $c(x, y)$.
2. The quality of restorating the image $c(x, y)$ in Fig. 3 is lower than in Fig. 1. This means that it is necessary to improve the technique based on solving the Fredholm equation.

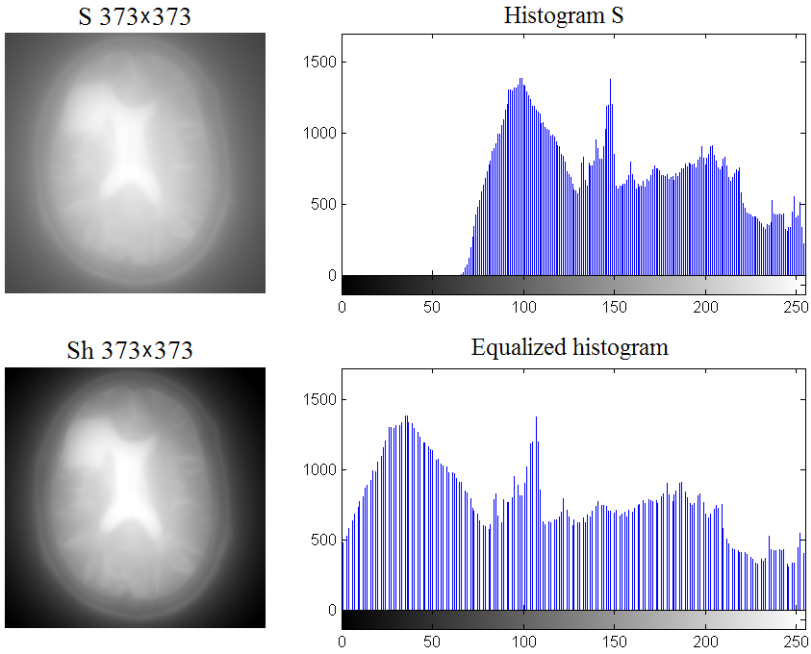

Fig. 2. The direct problem. Calculating $S(x, y)$ in discrete form and $S_h(x, y)$ after histogram equalization.

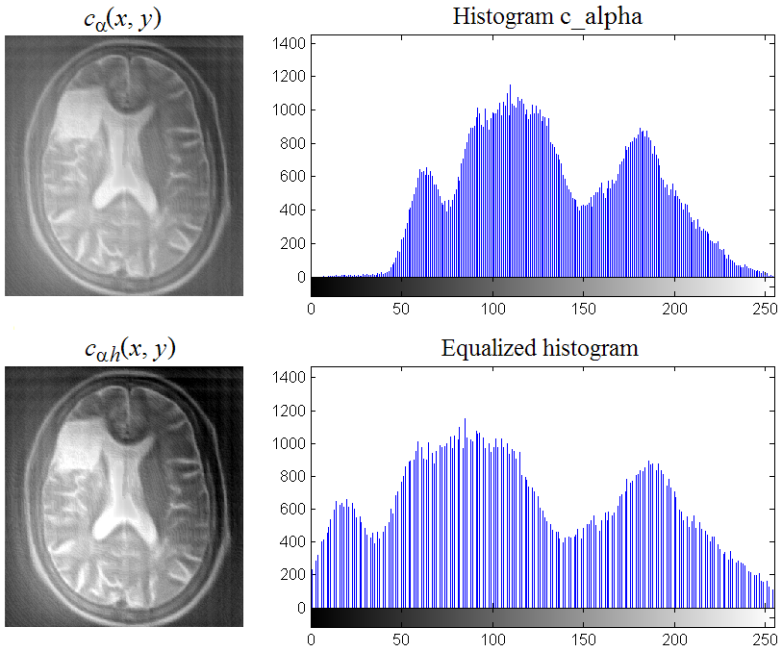

Fig. 3. The inverse problem. Obtaining tomogram by solving Fredholm equation (2) using method of 2-dimensional DFT and Tikhonov regularization

Acknowledgements: This project is supported by the Russian Foundation for Basic Research (RFBR), project grant No 13-08-00442.

References

[1] Tikhonov A.N., Arsenin V.Ya., Rubashov I.B., Timonov A.A. 1984. The first Soviet computer tomograph. *Priroda*. № 4, 11.
[2] Tikhonov A.N., Arsenin V.Ya., Timonov A.A. 1987. *Mathematical problems of computerized tomography*. Nauka, Moscow.
[3] Sizikov V.S. 2011. *Inverse applied problems and MatLab*. Lan', Saint-Petersburg.
[4] Sizikov V.S. 2001. *Mathematical methods for processing the results of measurements*. Politekhnika, Saint-Petersburg.
[5] Diakonov V., Abramenkova I. 2002. MATLAB. *Signal and image processing*. Piter, Saint-Petersburg.
[6] Engl H.W., Hanke M., Neubauer A. 1996. *Regularization of inverse problems*. Kluwer, Dordrecht.
[7] Verlan' A.F., Sizikov V.S. 1986. *Integral equations: methods, algorithms, programs*. Nauk. Dumka, Kiev.

Development of an optical tracking system for a novel flexible and soft manipulator with controllable stiffness for minimal invasive surgery (MIS)

E. Gerz, M. Mende, H. Roth

Institute of Control Engineering, University of Siegen, 57068, Siegen, Germany

Authors e-mail address: erwin.gerz@uni-siegen.de

Abstract

In minimally invasive surgery, tools go through narrow openings and manipulate soft organs that can move, deform, or change stiffness. There are limitations on modern laparoscopic and robot-assisted surgical systems due to restricted access through Trocar ports, lack of haptic feedback, and difficulties with rigid robot tools operating inside a confined space filled with organs. Inspired by the octopuses movement the STIFF-FLOP project created a soft robotic arm that can squeeze through a standard 12mm diameter Trocar-port, reconfigure itself and stiffen by hydrostatic actuation to perform compliant force control tasks while facing unexpected situations.

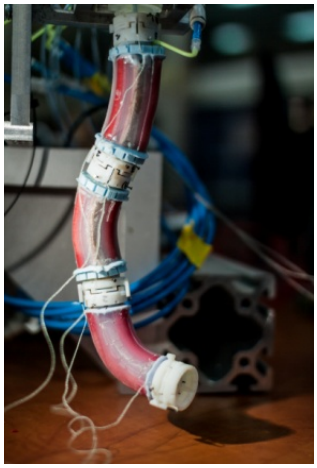

Figure 1: STIFF-FLOP Manipulator

To monitor and control the STIFF-FLOP arm the video data of the surgeon's endoscope is recorded and evaluated. After colour and distortion corrections, the robot arm has to be detected in the images. The challenge here is in the detection of a flexible arm which changes its shape and size during the movement, as well as the fact that the visible section of the arm can vary in the endoscope image. With the aim to develop an automated learning and recognition method with high performance, a texture-based pattern recognition and classification method based on Support Vector Machines [3] has been implemented. The basic idea is to divide the image into small rectangular parts which are classified as object or background.

The next step is to calculate the spatial position of the manipulator in camera coordinates. Therefore, the centre line of the detected object is identified and the diameter is calculated accordingly. Based on this information the x and y coordinates can be extracted from the pixel coordinates, the distance of the object to the camera's optical centre is calculated based on the determined diameter.

The implemented machine learning STIFF-FLOP arm detection algorithm has shown a good identification of the manipulator. In order to integrate the vision system into the control loop, it was necessary to detect the connection points of the manipulator. Therefore, another approach has been chosen to enhance the position detection of the connecting elements containing the force/torque sensors which are used to control the manipulator.

The idea is to place unambiguous markers on the rigid connectors that are easy to detect and which imply a fixed offset to the centre of the manipulator. Reproducible results were achieved by the application of green ring markers as displayed in Figure 3. The idea is based on an algorithm for camera calibration with two arbitrary coplanar circles [1].

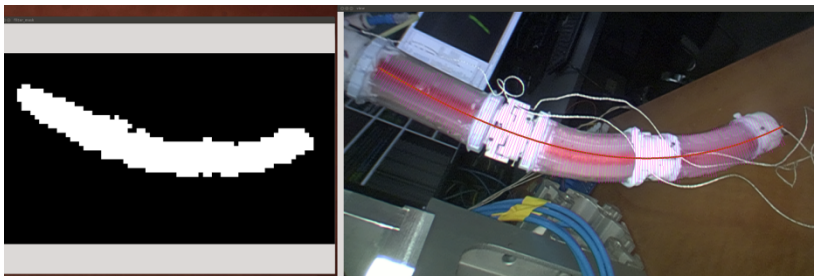

Figure 2: (l) detected parts of the STIFF-FLOP arm, (r) Surveyed manipulator

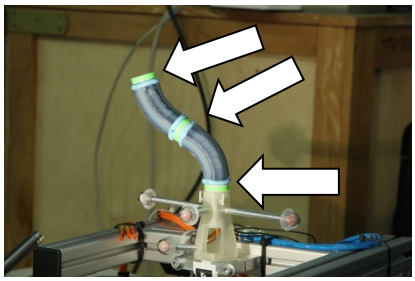

Figure 3: Manipulator with ring markers

The detection process is visualized in figure 4. As a first step a mask containing all the green coloured areas of the video image is generated (b). This mask is the source for a standard contour detection algorithm. The detected contours are filtered based on a set of rules eliminating noise and other unsuitable objects so that only sections of ring-like objects of a suitable size should reach the next step (c).

The remaining contours are split into a concave (d, blue curve) and a convex (d, red curve) part. Each of them is now treated like the visible part of a closed elliptical shape.

Unfortunately, the contours cannot be used directly to determine the parameters of an ellipse, because they are quite noisy and therefore the ellipse parameters are oscillating in a wide range.

A RANSAC [2] approach seems suitable to improve the results. 10% of each contour's points are selected and fed into a least-square-error algorithm to define the ellipse's parameters. The resulting ellipse is compared with the contour as a whole and the average error is evaluated. If the ellipse fits well, the parameters are stored – if not, another set of points is generated as a basis for the parameter calculation. The results can be seen in (e).

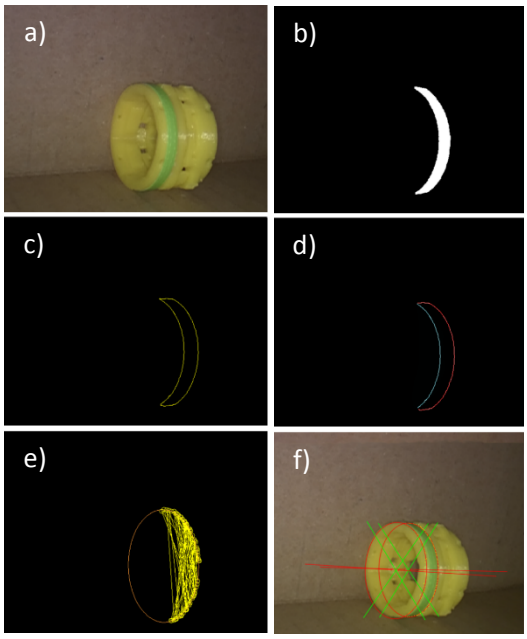

Figure 4: Ring marker detection sequence

The determined ellipses can be seen as projections of circles. Knowing the circles diameters, the calculation of those circles' poses in space is possible (f). Although the orientations of these generated poses are ambiguous, the position helps to determine the position of the STIFF-FLOP connectors in space.

Both algorithms have been verified in an experimental setup which is shown in figure 5. The manipulator is located in the middle; the left monitor shows the recorded video stream. The right monitor shows a simulation of the manipulator based on the model that is used for controlling the manipulator.

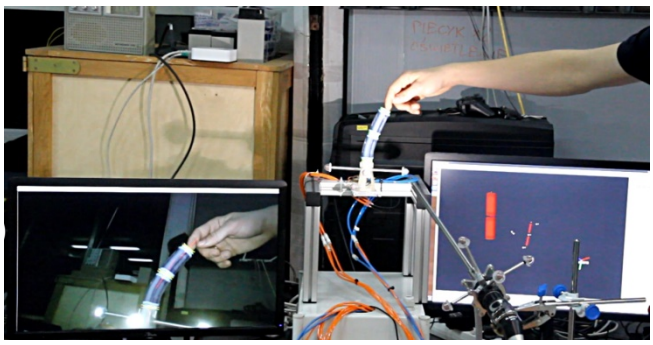

Figure 5: Verification of results

The detected position of the connectors is compared to the positions of the control model. If a deviation, which might be caused by external forces which are applied, is detected, the deformation is recognized by the optical tracking system and an alarm signal is displayed by colouring the simulated arm in red.

Acknowledgements: The work described in this paper is supported by STIFF-FLOP project grant from the European Communities Seventh Framework program under grant agreement 287728.

References

[1] Chen, Q., Wu, H., & Wada, T. (2004). *Camera Calibration with Two Arbitrary Coplanar Circles*. Computer Vision - ECCV 2004. Lecture Notes in Computer Science Volume 3023, S. 521-532. Berlin Heidelberg: Springer.

[2] Fischler, M. A., & Bolles, R. C. (June 1981). *Random Sample Consensus: A Paradigm for Model Fitting with Applications to Image Analysis and Automated Cartography*. (J.D.Foley, Hrsg.) Graphics and Image Processing.

[3] Vapnik, W., & Chervonenkis, A. (1974). *Theory of Pattern Recognition*.

Methods to determine the scaling factor in X-ray images for exact preoperative planning in hip surgery

O. Gieseler[1], H. Roth[1,2], J. Wahrburg[1,2]

[1]*Center for Sensor Systems (ZESS),Univerity of Siegen, Paul-Bonatz-Straße 9-11, 57076 Siegen, Germany*
[2]*Institute of Control Engineering University of Siegen, Hölderlinstraße 3, 57076 Siegen, Germany*

Authors e-mail address: gieseler@zess.uni-siegen.de

Introduction

This paper presents and compares common methods for calculating the scaling factor of X-ray images and reveals their basic technical difficulties, accuracy and error sources. Finally a new approach is introduced which is based on a stereo camera system used to identify the magnification in anterior-posterior pelvis images for hip application, considering the geometry of X-ray apparatus while minimizing errors by foreclosing the well-known central issues of all the conventional methods. In cases of using X-rays for preoperative planning, like in our application, to prepare total hip arthroplasties it is indispensable for correct choice of implant components to identify accurately the correct scaling. Acquired X-ray images are always afflicted by a scaling factor due to the perspective central projection (Fig. 1) of the human body to the X-ray film or image receptor. This is caused by the divergent, conical beam emitted by the X-ray source, representing the projections focal point in the tip of the cone. Thus, projections of objects and measured sections are scaled up to a certain extent. All objects in one plane parallel to the film appear with the same magnification [1] not affected by the exact position in this plane. Hence, magnification can be assumed as only dependant on the planes distance to the film, so there is just one scaling factor to be identified.

State of the art

There are various approaches to find out the magnification and improve the scaling process.
The existing methods can be divided in three main groups according to principle:

Assumption of constant scaling factors for all patients: In this case a scaling factor mean value, depending on device specific dimensions of X-ray apparatus, is applied. King et al. [2] observed a mean error of 2.4% at 118% and Riddick et al. [3] reported 2% mean error at 127% constant magnification factor. Both stated a magnification range from 113% respectively 116% to 132% leading to maximum errors of 19% and 11%.

Placing one or more radiopaque calibration bodies in the beam: Several designs of calibration bodies are described, e.g. rulers, discs or coins, single affixed on the skin [4] or multiple fixed in a mount [5] and spheres with diameters between 20 and 30 mm [2,3,6,7] mounted, height adjustable either in a tube, special stand or strap holders (Sectra Calibration Tool) or on goosenecks e.g. Voyant Mark (Brainlab) or Aktual Evo (J2 Medical). All these are meant to be placed beneath or between the legs exactly in the same plane as the hip joints centers i.e. the scaling plane (Fig. 1). Mean errors are reported between 1.12% [5] and 4.8% while occurring 24.7% in the worst case [2]. The approach according King et al., using two marker groups, leading to nearly similar results, but preventing large outliers [2].

Geometric approach: With given dimensions of an X-ray apparatus it is also possible to determine the scaling factor based on the 2nd intercept theorem. According to Heinert et al. measuring the plane-detector or plane-table distance with e.g. with a ribbon, combined with the source-detector and table-detector distance given from the data sheet of the X-ray (Fig. 1), leads to mean errors of 1% (maximum 10%) [7].
In all pre-described methods the procedure to determine the plane of the hip joints is either carried out through statistical considerations or by palpating the greater trochanter as position reference, mostly with internally rotated leg. Therefore accuracy is highly dependent on operator experience, anatomical conditions and legs position. For those reasons it is difficult to define the exact scaling plane.

New alternative using a stereo camera system

We developed a method that determines the hip joint rotation center, employing a stereo camera system (Axios 3D Services GmbH, CamBar2), to define the scaling plane without the need for palpating the trochanter. This is done by noninvasively attaching a reference body (DRB), which can be recognized and located by the camera, to the distal part of the thigh. Then, while moving the leg through the range of motion, the camera tracks and records the DRB´s positions (Fig. 2). Due to the ball joint character of the hip joint, all collected points are lying on a spherical surface as part of a sphere. The spheres center can be calculated by regression algorithms and matches the hip joint center. Combined with additional measurement of the table plane of the X-ray by probing

with a Pointer-DRB our software computes the scaling plane-table distance. Finally applying the geometric approach yields the scaling factor. To evaluate the method we created a test arrangement composed of an artificial femur bone pivot-mounted in a table holder, representing the pelvis (Fig. 2). X-ray images were generated with a Ziehm Vario 3D C-arm (23cm image intensifier, 97cm source detector distance). The application of the procedure will be carried out in the X-ray room before image acquisition, while the patient is lying in supine position, and shall not take more time than accurate placement of a calibration body.

Results and Discussion

We achieved scaling factor errors of maximum 1% in the first trials with our setup. Accuracy has been proven by comparison with an exactly placed calibration body. Potential inaccuracies may arise from limited camera 3D accuracy and unintentional relative movement of the DRB to the thigh bone and finally the hip joint center, due to soft tissue elasticity. Influence of the last one has not yet been considered.
In summary, the first tests justify the assumption that our approach offers a more accurate and reproducible way to determine the scaling factor of X-ray images. In contrast to conventional methods it neither depends on statistical factors nor on a more or less accurate positioning of calibration bodies. In forthcoming steps the practical applicability, possible error sources and achievable accuracy will be further investigated.

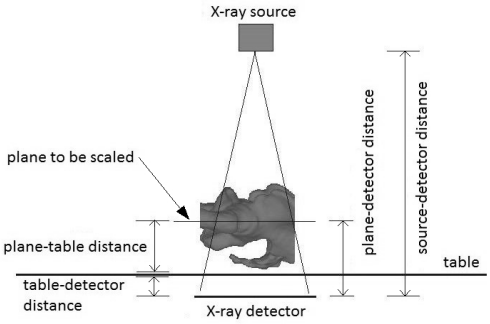

Fig. 1: Structure and geometry of an X-Ray apparatus.

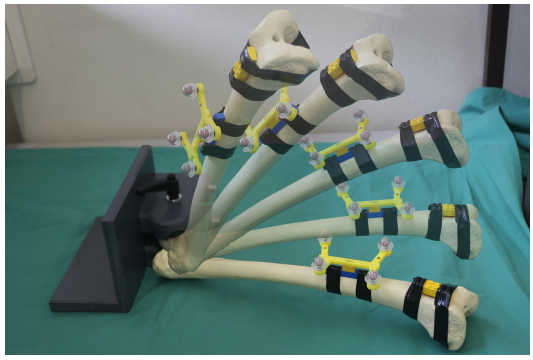

Fig. 2: Test setup for hip joint center determination during motion

Acknowledgements: Part of this work is carried within the framework of the ZIM project KF2383704KJ4 funded by the German Federal Ministry BMWi.

References

[1] Clarke IC, Gruen T, Matos M, Amstutz HC. 1976. Improved methods for quantitative radiographic evaluation with particular reference to total hip arthroplasty. Clin Orthop Relat Res. 121:83-91.
[2] King R J, Makrides P, Gill J A, Karthikeyan S, Krikler S J, Griffin D R. 2009. A novel method of accurately calculating the radiological magnification of the hip. J Bone Joint Surg [Br] 2009;91-B:1217-22.
[3] Riddick A, Smith A, Thomas D P. Accuracy of preoperative templating in total hip arthroplasty. 2014. Journal of Orthopedic Surgery 2014;22(2):173-6
[4] Conn K S, Clarke M T, Hallett J P. A simple guide to determine the magnification of radiographs and to improve the accuracy of preoperative templating. 2002. J Bone Joint Surg [Br] 2002;84-B:269-72.
[5] Wimsey S, Pickard R, Shaw G. Accurate scaling of digital radiographs of the pelvis. 2006. J Bone Joint Surg [Br] 2006;88-B:1508-12.
[6] Blake CA, van der Merwe J, Raubenheimer JE. A practical way to calibrate digital radiographs in hip arthroplasty. 2013. SA Orthopedic Journal Vol 12, No 4
[7] Heinert G, Hendricks J, Loeffler M D. Digital templating in hip replacement with and without radiological markers. 2009. J Bone Joint Surg [Br] 2009;91-B:459-62.

The sensor system for investigation the air flow movement in the 3D solid model of the human nose

A. Rassadina[1], G. Lukyanov[1], E. Frolov[1]

[1]*Department of Laser and Light Engineering, ITMO University, 197101, St. Petersburg, Russia*

Authors e-mail address: a.a.rassadina@gmail.com

Abstract

Using of the artificial models of nose is one of the principal methods of examination of breathing. They are demonstrable and allow you to see convective profile in virtually all parts of nose, which is often not possible in such studies in humans. This study presents a sensor system for investigation the breath in the artificial model of nose and nose sinuses. The conceptual difference of our investigation is in use the air as the service fluid. Previously presented models based upon the visual observations of convective flows, there, for visualization as the service fluid used the water with injection the dye [1-3] or used the air-flue gas mixture [4]. Presented method and sensor system are based on measurements of air flow conditions in artificial model of nose at the time of simulation breath. The sensor system allows receiving pressure drops in different parts of the model.

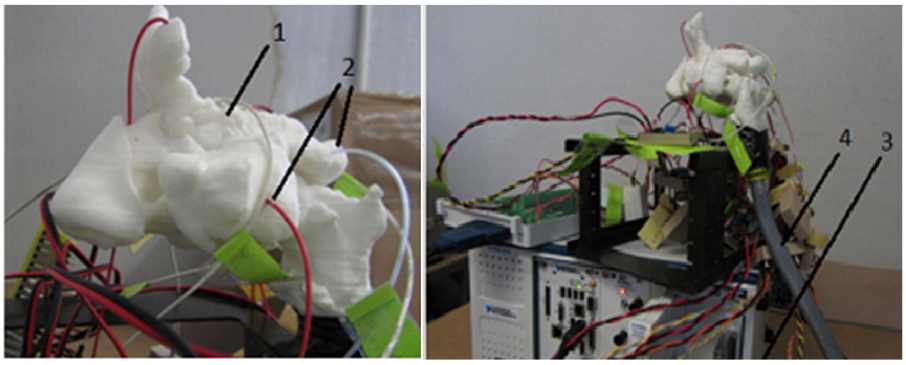

Fig. 1: Artificial model: 1 – solid model with nasal cavities; 2 – shunt tubes to piezo-resistive pressure sensors; 3 – processing device; 4 – breathing tube for simulation respiration.

The artificial model of nose and nose sinuses was created from the data of computer tomography with the help of 3D printer. The model includes cavitas nasi with nasal turbinate inside. The nose sinuses open in cavitas nasi. Breathing simulated by human lung through the bellow, which applied to model, replacing the trachea. Examination of breathing was executed by the sensor system including 17 piezoelectric pressure sensors used for measuring flow pressure drop within the air stream as a function of time. The sensor system and the artificial model are shown in the fig. 1. Pressure drop measured through a thin tubes connected with piezoelectric pressure sensors (1) in the left and the right entrances of nose (vestibule of nose); (2) in the left and the right maximally sinuses; (3) in the left and the right parts near nasal septum (aria of ridge of nose); (4) in the left and the right frontal sinuses; (5) in the left and the right anterior, middle and posterior ethmoid cells; (6) in the left and the right sphenoid cells; (7) in choanae. Signals received from pressure sensors supplied to the data automation subsystem, which control and synchronize the sensors. Settings and data recording performed by software provided by the manufacturer.

Interpretation and processing of the results (presented on fig. 2) is the main part of the study performed. It can be seen that the pressure fluctuations obtained differ in amplitude, but are close in frequency. Furthermore, in some parts of the nose, for example in ethmoid cells, is observed time lag. A more in-depth analysis of the results can be obtained by the spectral analysis method. Fig. 3 is a graph of the spectral power density, built for the experimental modeling results. The spectrum is continuous. Two main peaks can be distinguished on the graph: 0,22 Hz (4,54 s); 0,64 Hz (1,56 s). There the spectrum with the maximum value of PSD defines the time of the "inspiration- expiration" cycle. The second on height spectrum characterizes weak fluctuations with mean wave period about 1,5 seconds, putting on the tops of the main "inspiration- expiration" cycle. Also we can identify peaks corresponding to approximately the duration of the inhalation is set to be 1,7 seconds (0,59 Hz), the duration of the exhalation equal to 2,3 (0,44 Hz) on the basis of average data.

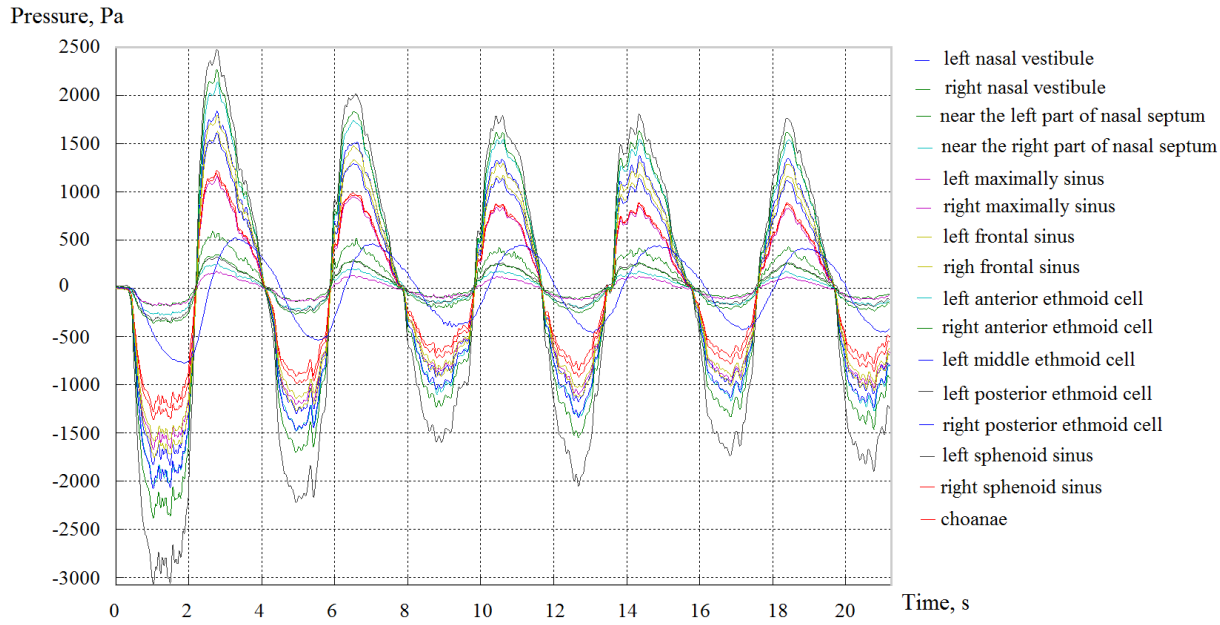

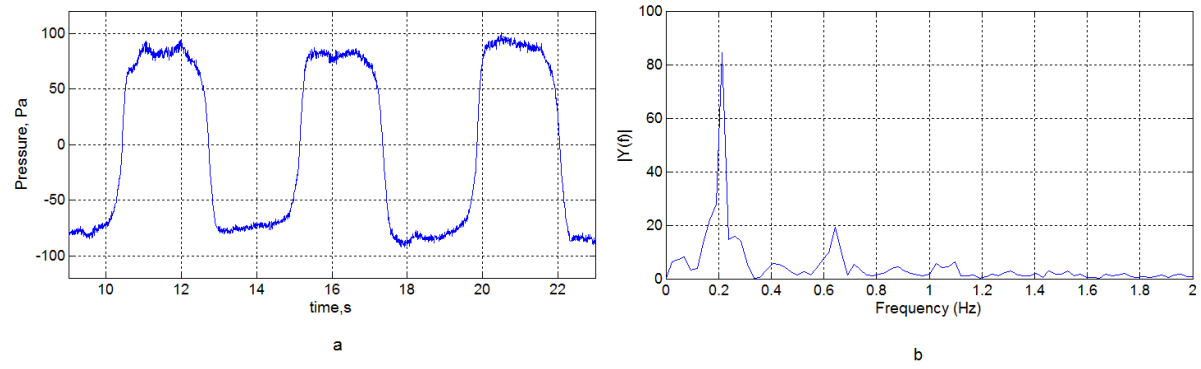

According to the study results, we can get the following conclusions: the sensor system is sensitive for both basic characteristics of breathing (such as the time of inhalation – exhalation) and weaker fluctuations observed in different parts of the nose during the breathing. The graph of the spectral power density showed a significant role of weak fluctuations. Our intention is to include in this fluctuations the information about respiratory, lungs and cardiovascular diseases.

Acknowledgements: The authors thank DR. R. Neronov, chief physician clinics "MMT" (St. Petersburg) for support in creation 3D solid model and for useful discussions.

References

[1] Doorly, D.J., Taylor, D.J., Franke, P., Schroter, R.C., 2008a. *Experimental investigation of nasal airflow*. Proc. Inst. Mech. Eng. H: J. Eng. Med. 222, 439–453, doi:10.1243/09544119jeim330.

[2] Spence, Callum, J. T., 2011. *Experimental Investigations of Airflow in the Human Upper Airways During Natural and Assisted Breathing* A thesis presented for the degree of Doctor of Philosophy in Mechanical Engineering at the University of Canterbury, Christchurch, New Zealand.

[3] Mlynski, G., Grützenmacher, S., Plontke, S., Mlynski, B., Lang C. 2001. *Correlation of nasal morphology and respiratory function.* Rhinology, 39, 197–201

[4] Uliyanov, Y.P., 1995. Nose aerodynamics. Arch. Otolaryngol. Head Neck Surg. 121: 352.

Telemetric Multi Sensor System for Medical Applications – The Approach

J. Weidenmueller[1], Ch. Walk[1], O. Dogan[1], P. Gembaczka[1], A. Stanitzki[1], M. Goertz[1]

[1]*Fraunhofer Institute for Microelectronic Circuits and Systems, Finkenstraße 61, 47057 Duisburg, Germany*

Authors e-mail address: Jens.Weidenmueller@ims.fraunhofer.de

Abstract

Continuous monitoring of physiological parameters in cardiovascular areas allows early detection of critical conditions which may lead to clinical symptoms and hospitalization, if not treated in time. Thereby early diagnostics, optimization of therapy and reduction of therapy costs can be achieved [1], see Figure 1. This study presents the concept of an implantable multi sensor system that utilizes, amongst others, capacitive pressure sensor elements monolithically integrated in a CMOS process suitable for medical implants [2]. In medical applications it is generally recommended to achieve high-precision pressure measurement. For example the controlling the haemodynamic [1] in pulmonary artery requires a very accurate detection of important physiological changes in pressure having to meet the challenge of a very high miniaturization level.

The approach of a multi sensor system enables parallel monitoring of side effects, see Figure 2. The patient's position, shocks, temperature or energy level deviations may lead to inaccuracies or faulty pressure measurement. By monitoring these influences, compensations of measured pressure values can follow in a later step.

In prior studies the potential of using the capacitive measurement principle for medical sensor implants by the means of wireless energy and data communication has successfully been proven. For example, the sensor element, compare Figure 3, is applied in a system to treat an abnormal accumulation of cerebrospinal fluid in the brain, known as hydrocephalus [3, 4]. This system has already achieved medical certification and has been implanted in humans [5].

However, there is a need for methods to control the long-term stability, biocompatibility and integrity of implantable systems. The realization requires many new technologies and material combinations to fulfill these specifications, especially in the domain of implant encapsulation. Most implantable and medically approved systems, like the presented system for hydrocephalus treatment, are encapsulated by materials like titanium or ceramics. These techniques obtain limitations with regard to further miniaturization of implantable sensor systems. The required encapsulation shall not only guarantee biocompatibility and long-term functionality, but also show suitable pressure transmission properties. These requirements can be achieved by a very thin three-dimensional passivation of the micromechanical pressure sensor membranes by, for example a stack of ceramic layers by Atomic Layer Deposition (ALD). ALD passivation method shows hermetic sealing and high conformity, even on complex topographies. [6, 7]

Figure 4 shows the basic assembly and packaging concept of the new implantable multi-sensor system setup. The core element is a multi-functional Application Specific Integrated Circuit (ASIC) which is able to handle all measurements but also power management and communication with the extracorporeal electronics. The complete system operates without any integrated energy sources. All the components are simulated and designed in such a way, that very low power consumption allows telemetric operation distances up to 15 cm. The communication is according to the international standard for passive RFID item level identification for air interface communications at 13.56 MHz (ISO/IEC 18000-3). The required antenna is located within the circuit board.

The multi-functional ASIC has recently been developed at Fraunhofer IMS. First evaluation results regarding the pressure sensor performance are presented in Figure 5. There, the calibration errors plus 1σ deviation is presented with respect to applied temperature and two different assembly technologies. The assembly technologies differ in the polymers utilized for die-bond and glob-top. While #1 represents a soft material, #2 represents a high temperature stable material that meets further requirements regarding ALD of further encapsulation materials. Independently from assembling, the multi sensor system fulfill requirements to obtain high accuracy pressure measurements with errors < 2 hPa.

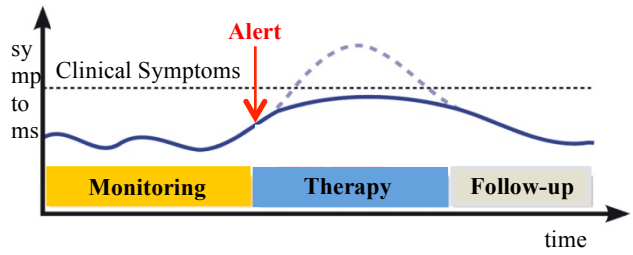

Figure 1: Early detection of critical conditions and start of therapy before clinical symptoms may occur [according to 2]

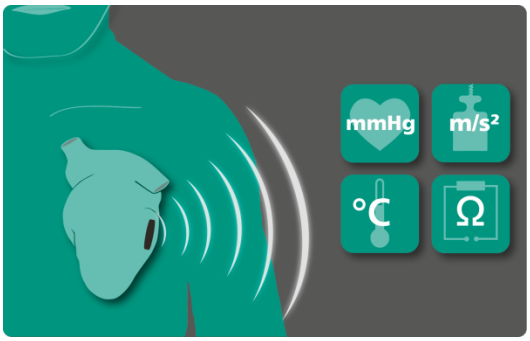

Figure 2: Schematic on functions of multi sensor system

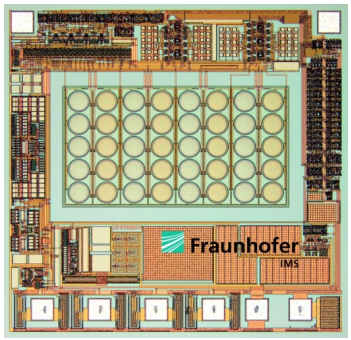

Figure 3: Photograph of capacitive pressure sensor (size 1.85 mm x 1.8 mm)

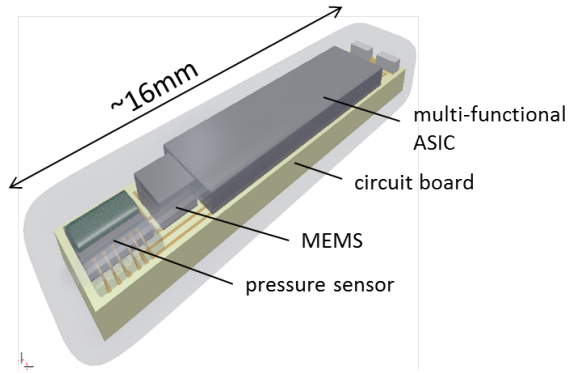

Figure 4: Basic assembly and packaging concept of the new multi sensor implant

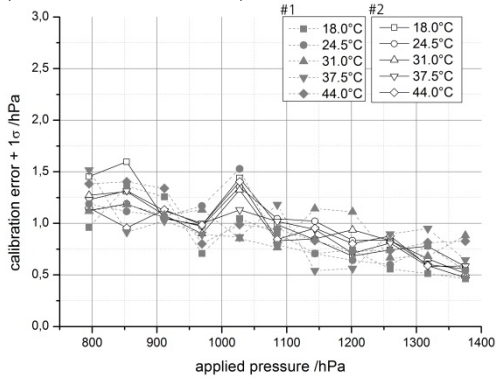

Figure 5: Calibration error + 1 σ deviation of pressure sensor connected to multi sensor system, #1 and #2 represent different assembly materials

References

[1] Urban, G., Bunge, A. (Eds.): VDE-Positionspapier Theranostische Implantate. Verband der Elektrotechnik Elektronik Informationstechnik e. V. und Deutsche Gesellschaft für Biomedizinische Technik im VDE e. V., Frankfurt 2011

[2] N. J. Cleven, J. A. Muentjes, H. Fassbender, U. Urban, M. Goertz, H. Vogt, M. Graefe, T Goettsche, T. Penzkofer, T. Schmitz-Rode, and W. Mokwa, "A Novel Fully Implantable Wireless Sensor System for Monitoring Hypertension Patients", IEEE Transactions on Biomedical Engineering, Volume 59, No. 11, November 2012

[3] https://www.miethke.com/produkte/sensor-reservoir/beschreibung/ (April 2016)

[4] Mokwa, W.; Schnakenberg, U.; Goertz, M. & Trieu, H. K. (2015), „Mikro-Transpondersysteme für medizinische Anwendungen", TUDpress, Dresden.

[5] Heckelmann, M. Antes, S. Breuskin, D. Oertel, J. Tschan, „First clinical experience using a novel shunt reservoir with a telemetric pressure probe for permanent implantation,", C. A. 2015 DGNC, Karlsruhe, Germany, doi: 10.3205/15dgnc161

[6] W. Betz, "Flexible microelectromechanical implants for chronic use: encapsulation concepts and test procedures for material characterization," dissertation, Universität Duisburg-Essen, 2011

[7] P. Gembaczka, M. Goertz, Y. Celik, A. Jupe, M. Stuehlmeyer, A. Goehlich, H. Vogt, W. Mokwa, M. Kraft "Encapsulation of Implantable Integrated MEMS Pressure Sensors Using Polyimide Epoxy Composite and Atomic Layer Deposition", J. Sens. Sens. Syst., 3, 335-347, doi:10.5194/jsss-3-335-2014, 2014

Microfluidic structures for stray light measurement in cytometry applications with integrated optical fibers made from PDMS

I. Vinogradov [1], M. Freundlieb [1], M. Schlüter[1]

[1]*Westphalian University of Applied Sciences, Germany*

Authors e-mail address: ilya.vinogradov@w-hs.de

Abstract

In many medical and biological applications specific cells or in general particles within a liquid have to be analyzed. With the so-called cytometry particles within liquids can be measured regarding particle type, size and surface properties. In many applications it is advisable to replace the classical laboratory analysis through integrated (microfluidic) systems, which combine all the processes on one chip.

In this work a Lab on a Chip system for hydrodynamic focusing of a sample stream with particles in microfluidic channel structures is introduced.

A particle containing sample stream is surrounded by a sheath stream (hydrodynamic focusing) [see fig.1]. This forces the particles to flow one by one through the channel. The particles pass a laser of appropriate wavelength. To pass the laser centered it is necessary that the sample stream is not only focused laterally but also from the top and the bottom. [1]

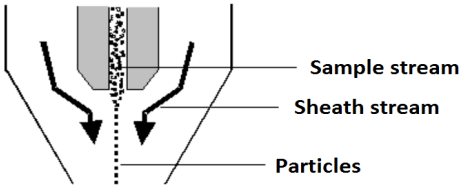

Figure 6: Schematic representation of the hydrodynamic focusing [2]

Passing the laser the particles cause characteristic scattered light. This scattered light is detected at small angles as forward scattered light and at larger angles as the side scattered light. By analyzing the magnitude of the forward and side scattered light the particles can be classified in terms of size, surface properties, internal structure, etc.

Previous structures were micromilled in PMMA or molded in PDMS. The microfluidic channels allowed a hydrodynamic focusing of a sample stream in two dimensions. The two dimensional fluid focusing is realized by the structure shown in figure 2. These structures can be produced on one side. In the middle channel the sheath stream is introduced into the first inlet (1). Via the second inlet (2), the sample stream is introduced. It presses the sheath stream to the lower channel side. In the third inlet (3) sheath stream is introduced.

The sample stream is now surrounded on top and bottom with sheath fluid and can be constricted by the two side channels from the right and left. The two-dimensional focusing results in a very uniform liquid flow with well-defined position and velocity of the particles. This improves reproducible measurements and the signal quality of a single particle. The fluid flow is driven by hydrostatic pressure and precisely controlled by means of piezo valves.

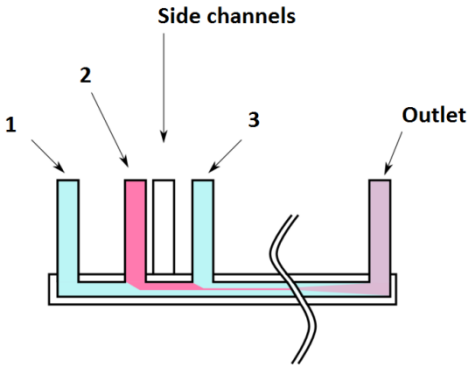

Figure 7: Fluidic structure for a two-dimensional focusing which can be manufactured on one side

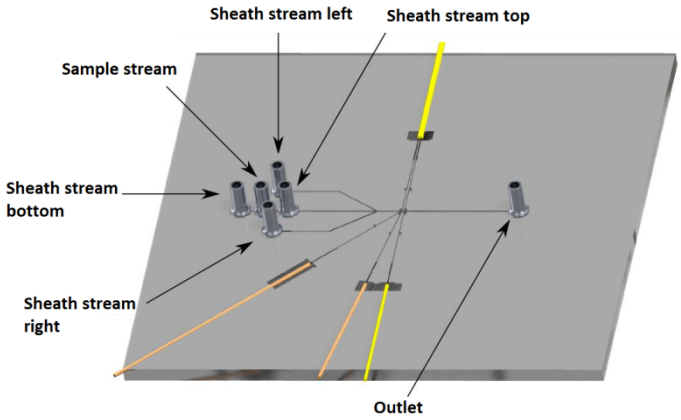

Figure 8: CAD-design of the microfluidic structure

Glass fibers for measuring forward and side scattered light were implemented in these structures. A 1310 nm laser was coupled through the microchannels by single-mode glass fibers with 9 µm diameter to generate a direct light pass in the size of the particles to be detected. At an angle of 10° and 45° additional 50 µm multi-mode glass fibers were used to measure the scattered light. The larger diameter of theses fibers results in an increased aperture [see fig. 2].The light was detected by a photodiode, amplified and graphically displayed. For testing the structures the sample stream was replaced by 9 µm diamond particles in water.

The integration as well as the alignment of the glass fibers turned out to be very complex and showed a low reliability. Therefore the mounting of commercially available glass fibers shall be replaced by in-situ manufacturing of waveguides in the structuring process of the channels.

There already exist publications about optical waveguides prepared from moldable polymer (e.g. PDMS) [3]. PDMS is particular well for preparing optical waveguides. It can be easily molded, has a high shape-persistent, low shrinkage and good optical properties.

First microfluidic channels were molded in PDMS and filled with higher refractive PDMS. The molding master structures were micromilled from PMMA. Due to the milling process the rough surface of the walls caused a high loss of the guided light.

Figure 4 shows light transmission through these PDMS waveguides with a lot of light leaving through the rough sidewalls. The light introduced into the PDMS optical fibers from the left side is transmitted by the structures to a screen on the right side.

Figure 9: Cross section through the optical waveguide structure

Figure 5 shows a cross section of the structure with the first and second cladding surrounding the light transmitting core.

Improved structures made from PDMS with a photolithographic structured mold are currently under development.

Figure 10: transmitted light through PDMS

In the next step the PDMS molded fluidic channel structures will be combined with the light guiding structures to an integrated cytometric labchip.

References

[1] "Flow Cytometry: First Principles," A. Longobardi Givan (2001)
[2] B. J. Holzknecht, Dissertation 2003 HU Berlin, online verfügbar: http://edoc. hu-berlin.de/ dissertationen/holzknecht-barbara-juliane-2003-07-14/HTML/chapter3.html
[3] Maluck, Matthias (2007): Replikationstechniken zur Herstellung einmodiger integrierter-optischer Komponenten aus neuartigen und kommerziellen Polymeren, Universität Dortmund

Mathematical model of free radicals flux action on eukaryotic cells lifetime and biomembranes sensitivity

A. Mamykin [1,3], M. Listov[2], A. Rassadina[3]

[1]*Saint-Petersburg State Electrotechnical University, 197376, Saint-Petersburg, Russia*
[2]*S.M. Kirov Military Medical Academy, 194044*, Saint-Petersburg, Russia
[3] *ITMO University, 197101, St. Petersburg, Russia*

Author e-mail address: a.a.rassadina@gmail.com

Abstract

A mathematical model of the impact of the free radicals flux on the outer surface of the eukaryotic cell membrane represents reversible and irreversible redox processes accompanying the electron transfer flux of free radicals from the body fluid through the cell membrane. The impact of these processes on the regulation of the vital functions of the biological system have been considered in terms of the model of physical and chemical interaction between the positively charged active sites of the plasmalemma surface and negatively charged particles of radicals flux. This interaction causes not only a local depolarization of a double electrical layer of the plasmalemma, but the membrane local oxidation and peroxidation that substantially affects on the functioning of the cell and its membrane sensitivity. According to a large number of experimental studies of free radical etiology disease it has been sufficiently reliably established that neurohumoral regulation of the vital functions of the biological system to a large extent depends on the balance between the rate of neutralization of free radicals (AOS efficiency of the body) and the performance of its oxidative systems (OS). This performance depends on the operating speed of the generation of the reactive oxygen species (ROS) and other free radicals and ultimately determines the flow rate of the active particles generated during vital activity of the organism under the influence of external and internal factors. The imbalance between the efficiency of the AOS and the OS performance leads to the development of pathologies, socially significant in that number.
The objective of the present work is the mathematical description of the interaction of the flow of free radicals from the outer surface of the plasma membrane cells, and communication concentration of free radicals in a liquid medium with a lifetime of eukaryotic cells. The physical basis of the mathematical model is a dynamic mechanism of adsorption of negatively charged particles on positively charged active sites of the energy inhomogeneous surface of liquid crystal cell membrane.
The model of interaction of the diffusion flux of free radicals to the active sites of the membrane is assumed that the flux with j_{dif} density formed on the outer surface of the membrane the elements of the following types of structures. The neutralized active site (N_n) is formed by adsorption of superoxide at the positive charge of the elementary electric dipole of integrated protein to form a covalent bond. This center is involved in the local depolarization of the membrane and provides counter transport of Na^+ and K^+ ions enhancing depolarization. Active center oxidation occurs with the formation of bridging oxygen structures oxide (N_{ox}) and peroxide (N_{px}) types, which are difficult to counter ion transport. In this case, it becomes possible to form porous structures because of burning the nearby environment of the lipid.
It is easy to see that vitality of a cell, which is determined by the ability of its response to the external excitation, is given by the equation

$$\frac{N_a}{N_0} = \frac{1}{j_{dif}}\left(\frac{N_n}{\tau_n} + \frac{N_{ox}}{\tau_{ox}}\right) \quad (1)$$

In equation (1) N_0 - initial concentration of active sites on the membrane surface, N_a - equilibrium concentration of active centers in the homeostasis, N_n - concentration of neutralized centers, N_{ox} - concentration of oxide structures. We assume that a single oxidation of the active site, as well as its neutralization, are reversible processes with lifetimes τ_{ox} and τ_n, j_{dif} is the density flux of the superoxide. Peroxidation of the active center is an irreversible process, so the concentration of these centers (N_{px}) increases during the life of the cell.
Assuming irreversibility of multiple oxidation of the active site, one can construct a system of equations describing the interaction of the flow of free radicals with the surface centers of the plasma membrane of eukaryotic cell.

$$\begin{aligned}
\frac{dN_a}{dt} &= j_{dif} + N_n\left(\frac{j_{dif}}{N_0}+\frac{1}{\tau_n}\right) + N_{ox}\left(\frac{j_{dif}}{N_0}+\frac{1}{\tau_{ox}}\right) + N_{px}\frac{j_{dif}}{N_0};\\
\frac{dN_n}{dt} &= j_{dif} - N_n\left(\frac{j_{dif}}{N_0}+\frac{1}{\tau_n}\right) - N_{ox}\left(\frac{j_{dif}}{N_0}-\frac{1}{\tau_{ox}}\right) - N_{px}\frac{j_{dif}}{N_0};\\
\frac{dN_{ox}}{dt} &= N_n\frac{j_{dif}}{N_0} - N_{ox}\left(\frac{j_{dif}}{N_0}+\frac{1}{\tau_{ox,eff}}\right);\\
\frac{dN_{px}}{dt} &= N_{ox}\frac{j_{dif}}{N_0};
\end{aligned} \tag{2}$$

Where $\tau_{ox,eff}$ is the effective lifetime of the oxidized center, considering two possible mechanisms for recovery: direct recovery of the center to the active state, and the internal transformation of the oxidized center in neutral.
Direct integration of the system (2) gives significant results. Modeling of the efficiency of the cells in conditions of balance and imbalance OS and AOS confirms the conclusion [1] of the possibility of the effective functioning of the cells in a wide range of concentrations of radicals. If the AOS compensates for changes in the activity of the OS, as well as external influence, for example, the influence of ionizing radiation sources, or stressors of different physical nature, causing increase in the concentration of free radicals in biological systems.
The figure below shows the dependence of the lifetime of the eukaryotic cell under conditions of balance (1) and imbalance (2) the OS and AOS, when the last does not compensate the the dynamics of the growth of radical concentration. The lifetime of the cells was determined by the achievement of equality concentrations irreversibly oxidized (non-functional) and current active centers. Comparison with previously tested real experiments confirmed the adequacy of the mathematical description of the effect of negatively charged particles on the lifetime of the cells of the body and a significant dependency of these processes on the balance of the OS and AOS in biosystems.
The immediate impact of the flow of negatively charged radicals in the lifetime of the cells is also easy to see from a comparison of the results of hemo-dependent exophthalmos [3] and polymyositis [2] modeling.

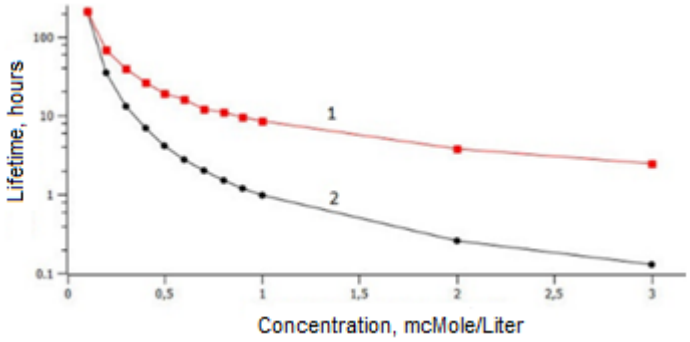

Fig. 1: Dependence of the lifetime of the eukaryotic cell under conditions of balance (1) and imbalance (2) the OS and AOS.

The analysis of the results of mathematical modeling and comparing the results with experimental data confirms the thesis of the decisive importance of negatively charged particles of active superoxide in the neurohumoral regulation of the basic functions of biological systems.

References

[1] Listov M. V., Mamykin A. I. 2014. *The concentration of free radicals in the body of mammals under changing activity of superoxide generation and antioxidant systems*. Vestnik rossiiskoi voenno-medicinskoi akademii [Bulletin of the Russian Military Medical Academy], vol. 45, no. 1, pp. 121-126 (in Russian).

[2] Listov M. V., Mamykin A. I., Tikhonova L. P. 2012. *Experimental modeling of polymyositis of Wagner-Unferriht form. The physiological, physical and mathematical aspects*. Vestnik rossiiskoi voenno-medicinskoi akademii [Bulletin of the Russian Military Medical Academy], vol. 40, no. 4, pp. 153-159 (in Russian).

[3] Listov M. V., Mamykin A. I. 2013. *Experimental modeling of hemo-dependent exophthalmos*. Vestnik rossiiskoi voenno-medicinskoi akademii [Bulletin of the Russian Military Medical Academy], vol. 42, no.2, pp. 120-125 (in Russian).

Gas- and bio-sensors based of graphene, produced by thermal destruction of SiC substrates

A. A. Lebedev[1,2,*], S. P. Lebedev[1,2], S. N. Novikov[3], Yu. N. Makarov[4,5], V. B. Klimovich[6]

[1]Ioffe Physical-Technical Institute, Russian Academy of Sciences, Politekhnicheskaya 26, 194021, St. Petersburg
[2]ITMO University, Kronverkskii 49, 197101, St. Petersburg
[3]Aalto University, Tietotie 3, 02150, Espoo, Finland
[4]Nitride Crystals Corp. group, Engel'sa 27, 194156, St. Petersburg
[5]Nitride Crystals Inc., 181 E Industry Court, Suite B, Deer Park, NY 11729, USA
[6]Russian Research Center for Radiology and Surgical Technologies, Ministry of Health of the Russian Federation, Leningradskaya 70, Pesochnyistlmnt, 197758, St. Petersburg

**) corresponding author: shura.lebe@mail.ioffe.ru*

Abstract

The discovery of the ability of carbon to form a 2D modification (graphene) has resulted in an explosive rise in the number of publications concerned with the properties of this material and its possible application in electronics. It is known that, being a 2D material, graphene possesses a unique set of electrical and physical properties:
- high mobility of carriers in combination with their low concentration;
- maximum possible area-to-volume ratio;
- low noise level.

These properties combined result in that adsorption of a minimum amount of impurity on the surface of graphene can noticeably change its overall conductivity. Thus, graphene is a rather promising material for fabrication of various kinds of sensors.

It was shown in [1] that graphene is capable of sensing even the adsorption of a single molecule. Depending on their charge and on the conductivity type of the graphene film, added gas molecules behave as donors or acceptors. That is they change the concentration of mobile carriers. Adsorbed molecules also create additional scattering centers and change the carrier mobility. As a result, the resistance of a film either decreases, or increases, depending on the type of an adsorbed molecule [2, 3].

The graphene films used in the present study were grown on semi-insulating substrates of 6H-SiC by thermal decomposition of SiC at a temperature of ~1700ºC. Prior to growth of graphene, the substrate was etched at 1600ºC in the atmosphere of hydrogen to remove from the surface its defective layer. Results of measurements by Auger and Raman spectroscopies confirmed the presence of single-layer graphene on the surface of silicon carbide.

The sensor structure was formed on a graphene film by laser photolithography with an AZ5214 photoresist. Excess amounts of graphene were removed from the substrate surface by etching in oxygen-argon plasma. Ti/Au (5/50 nm) ohmic contacts were fabricated by lift-off photolithography after the metals were deposited onto the photoresist surface by electron-beam evaporation. The sensor chip was fixed on a holder together with two Pt100 resistors. One of these was used to measure temperature, and the other served as heater.

Relative measurements of the resistance of the graphene-based sensor were made in the presence of NO_2 in the gas mixture (gas supply periods are designated by light gray bands) at 20ºC. Because the NO_2 desorption rate at room temperature is very low, the sensor was annealed at 110ºC after each exposure in order to return it to the initial state. The sensors developed in the study demonstrated sensitivity to the NO_2 concentration at a level of 1--0.01 ppb.

Results are also presented, obtained in the development and testing of a graphene-based sensor for detection of protein molecules. The sensor was fabricated by the technology previously developed for the gas sensor. The working capacity of the biosensor was tested with an immunochemical system constituted by fluorescein and monoclonal antibodies (mAbs) binding this dye. The antibodies were attached to the graphene surface via amino groups formed by a number of electrochemical reactions. The biosensor was placed in a buffer borate solution to which fluorescein molecules were added. The attachment of fluorescein molecules to the antibodies situated on the graphene surface changed the total resistance of the graphene film. It was found that the sensor is sensitive to a fluorescein concentration at the level of 1-10 ng/mL and to a concentration of conjugate of bovine serum albumin with fluorescein on the order of 1-5 ng/mL. It is shown that the device is highly promising for early diagnoses of various diseases.

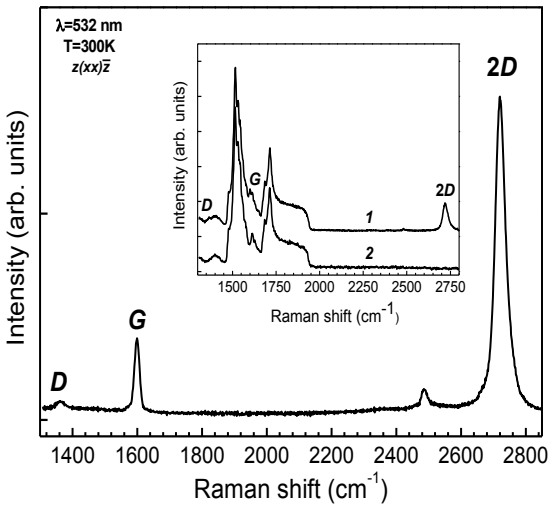

Fig. 1. Typical Raman spectrum of a graphene film grown on a 6H-SiC substrate. The inset shows the spectrum of the graphene /6H-SiC structure (1) and that of the 6H-SiC substrate 6H-SiC (2).

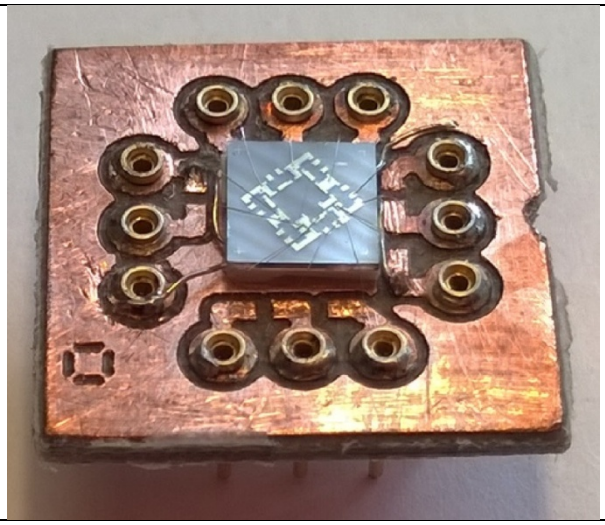

Fig. 2. Outward appearance of the sensor mounted in a case.

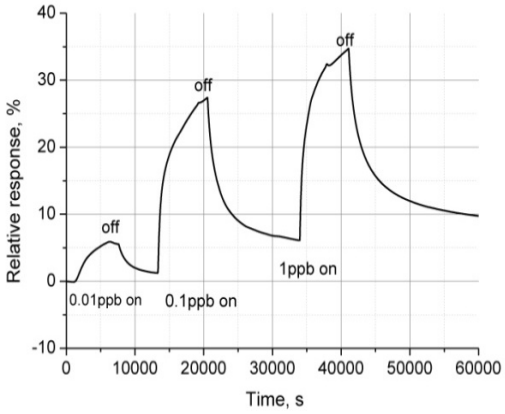

Fig. 3. Response to exposure to a gas mixture containing NO_2 gas at 100°C for the graphene-based device.

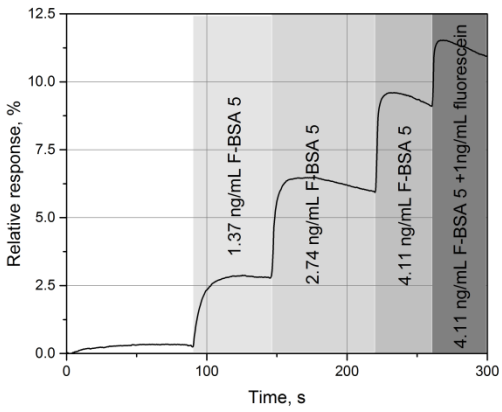

Fig. 4. Change in the sensor resistance brought in contact with solutions containing the concentrations of the BSA conjugate with fluorescein (F-BSA-5), specified in the plot, or a mixture of the conjugate and free fluorescein. The change in resistance in % is plotted along the ordinate axis, and the time of contact with the solutions (s), along the abscissa axis.

References

[1] F.Schedin, A.K.Geim, S.V.Morozov, E.W.Hill, P.Blake, M.I.Katsnelson, and K.S.Novoselov.// Nature materials. 2007. Vol. 6 P. 652-655.

[2] R. Pearce, T. Iakimov, M. Anderson, L. Hultman, A. Lloid Spetz, R. Yakimova// Sensors and Actuators B 155, pp. 451–455, 2011.

[3] S. Novikov, N. Lebedeva, and A. Satrapinski, Journal of Sensors, vol. 2015, Article ID 108581, 7 pages, 2015. doi:10.1155/2015/108581.

A Fuzzy based Energy Aware Unequal Clustering Protocol for Large Scale Wireless Sensor Networks

S. Khriji[1], D. El Houssaini[1], Ch. Viehweger[2], O. Kanoun[2]

[1] *University of Sfax, National Engineering School of Sfax, Tunisia*
[2] *Chemnitz University of Technology, Germany*

Author e-mail address: khrijisabrine@hotmail.fr

Abstract

Wireless Sensor Networks (WSNs) consist of a large number of distributed sensor nodes with limited processing capability and limited non rechargeable battery power. To reduce energy consumption and increase the network lifetime, a Fuzzy based Energy Aware Unequal Clustering protocol is strongly developed. The proposed algorithm is based on the partitioned circles network model having better accuracy in the energy consumption analysis than the rectangular one. This algorithm encompasses cluster head selection, intra-clustering and inter-cluster routing protocols. A comparison with similar works in the literature shows that the proposed algorithm outperforms the existed protocols in term of energy efficiency and network lifetime.

Keywords: *Wireless Sensor Networks, unequal clustering, multi-hop communication, energy balancing, optimal cluster radius, fuzzy logic.*

Proposed algorithm

The total area of the network is assumed as a circle with a base station at the center. The area is partitioned into rings with a specific radius called clusters. In every cluster, a Cluster Head (CH) is selected.

The proposed algorithm is split into two phases: cluster formation phase and data transmission phase. The cluster formation phase contains two stage; Offline stage including the process of calculating the radius of each ring which will be done manually before the network deployment. The outputs of offline stage are the optimal number of cluster $\mathbf{m_{kopt}} = \sqrt{\frac{9N_k(k^2+(k-1)^2)(2k-1)(2k-3)}{2(42(k-1)^2-17)}}\ \mathbf{k = 2, \dots, L}$ and the radius of CH in each ring $\boldsymbol{R_{(CH_k)_{opt}}} = \boldsymbol{\delta}\sqrt{\frac{2k-1}{m_{kopt}}}\ \mathbf{k = 2, \dots, L,}$ with N_k is the total number of nodes in ring k, L is the total number of ring, δ is the radius of each ring.

Based on fuzzy logic system [4], clustering setup stage attempts to select CHs. Three parameters are used: Residual energy, number of neighboring nodes and centrality of node among its neighbours. These parameters are chosen because of their importance for extending the network lifetime. The data transmission phase contains also two stages. An intra-clustering stage where data are forwarded from normal nodes to their proper CHs.Then an inter-clustering stage is performed to establish routes between CHs from consecutive rings until reaching the BS. To select a CHi from the next ring as a relay, this CHj should calculate the ratio of residual energy of CHi , E_{res}(CHi), and distance between CHi and CHj, $d_{CHitoCHj}$, as expressed in this equation:

$$\boldsymbol{ratio(E_{res}, d_{CHitoCHj}) = \frac{E_{res}(CHi)}{d_{CHitoCHj}}}$$

Simulation Results

Performance of proposed routing algorithm is compared with EEUC [1] and FAMCRO [2] protocols. The simulations are performed using Matlab [5]. The network scenario consist of 1000 nodes randomly deployed in 1000×1000 m area and BS at centre (0,0). Initial energy of all nodes is 0.5 J, data packet is of 6500 bits. For node's energy dissipation, model [3] is used with radio parameters E_{elec}=50 nJ/bit; ε_{fs}=10 pJ/bit/m^2 ; ε_{mp}=0.0013 pJ/bit/m^4.

To investigate the energy efficiency of protocols, sum of residual energy of nodes is measured and traced in figure 2 every 20 rounds. After 260 rounds, the residual energy in our proposed algorithm is approximately equal to 464.06 joule, only 40 joules are consumed from all the nodes. Our protocol is about 82 % more energy efficient compared to FAMCRO and about 91 % more energy efficient compared to EEUC.

Table 1 shows the rounds in which the first node died (FND) and half of the nodes dead (HND) for each simulated algorithm.

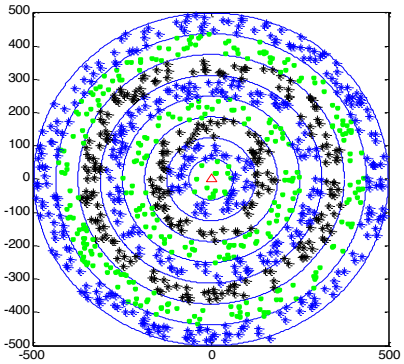

Figure 1. Nodes dispersion

Table 1.Values of FND and HND metrics for each algorithm

Protocol	FND	HND
EEUC	8	340
FAMCRO	10	540
Proposed Algorithm	125	2520

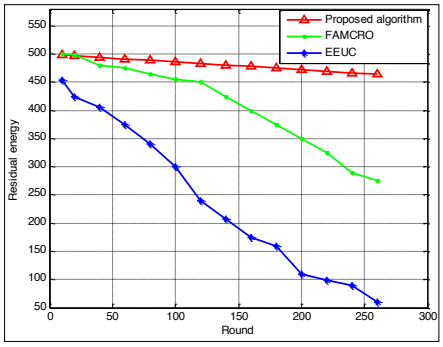

Figure2. Total residual energy of the network over rounds

As shown in table 1, the proposed algorithm outperforms EEUC and FAMCRO considering FND and HND metrics. Therefore, it has 92 % more network lifetime compared to FAMCRO Protocol.

Conclusion

An unequal size clustering algorithm to avoid hotspot problem, to balance the energy consumption among all sensor nodes and to achieve an improvement on the network lifetime has been presented. The proposed model uses fuzzy logic with residual energy, number of neighboring nodes and centrality of node among its neighbours to select the suitable cluster head. Simulation results show that the proposed algorithm provides best performance compared to EEUC and FAMCRO protocols and realizes very acceptable outputs in terms of energy efficiency and network lifetime.

References

[1] C. Li, M. Ye, G. Chen and J. Wu, "An energy-efficient unequal clustering mechanism for wireless sensor networks," Mobile Adhoc and Sensor Systems Conference, 2005. IEEE International Conference , vol., no., pp.8 pp.,604, 7-7 Nov. 2005.

[2] S. Gajjar, M. Sarkar, K. Dasgupta, "FAMACRO: Fuzzy and Ant Colony Optimization based MAC/Routing Cross-layer Protocol for Wireless Sensor Networks", International Conference on Information and Communication Technologies (ICICT 2014).

[3] A. Suharjono, G. Hendrantoro A new unequal clustering algorithm using energy-balanced area partitioning for wireless sensor networks, international journal on smart sensing and intelligent systems vol. 6, no. 5, december 2013.

[4] I. Iancu, "A mamdani type fuzzy logic controller in Fuzzy Logic: Controls, Concepts, Theories and Applications ", pp. 325–350, InTech, 2012.

[5] MathWorks Documentation Center [Online] Available: http://www.mathworks.in/help/matlab/.

Sensors materials on the basis of acrylic hydrogels for detection of ions of copper

T. Nosenko[1]., K. Volkova[1], M. Uspenckaya[1]

[1] *University ITMO, 49 Kronverkskiy pr-kt, Saint-Petersburg, 197101, Russia*

Authors e-mail address: tnnosenko@corp.ifmo.ru

Abstract

Recently the usage of hydrogels as the cheap and well absorbing materials, finds application in sensor technologies. The application of sensor materials is especially important in the field of ecology and environmental protection when it is required to check and clear environment from the harmful emissions containing ions pollutants of heavy metals. We have studied sorption of ions of polyvalent metals salts by acrylic hydrogels from their water solutions.

Samples of hydrogels, after their swelling in water solutions of $CuSO_4$ with various concentration have been investigated. IR-spectrums were removed on an FTIR-spectrometer of Bruker, Tensor 37 on the ATR prefix, ZnSe crystal, with the resolution of 4 cm-1. The FTIR-spectrometry was carried out on average FTIR-radiation range from 600 cm^{-1} to 4000 cm^{-1}.

Preparation of samples: dry acrylic hydrogel puted in water solutions of $CuSO_4$ with various concentration for 24 hours, then the sample was taken from solutions and his FTIR-spectrum was removed.

The purpose of work was - to analyse the existence of the metal containing particles in hydrogel. It is also important to draw a conclusion on the mechanism of sorption of metals ions by hydrogel, whether metal ion creates a chemical bond with molecules of hydrogel or there is a usual adsorption of metal's ions by acrylic polimers.

Samples:

1) hydrogel – the cross-lined copolymer on the based on partially neutralized acrylic acid (AK) (extent of neutralization 0,8) and acrylamide (AA) in the ratio AK: AA = 70:30. As the cross-lined agent N,N methylene bis acrylamide with a mass fraction of 0,1 mass.% has been used. Hydrogel has been synthesized by radical polymerization in the water environment at a temperature of 45 C^o.

2) Water CuSO4 solutions – 1 M; 0,1 M, 0,01 M.

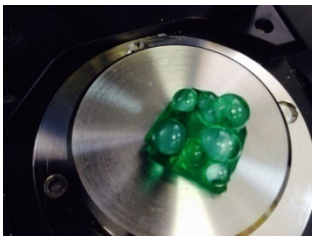

Fig. 1: Hydrogel with sorption of ions of copper on the ATR prefix.

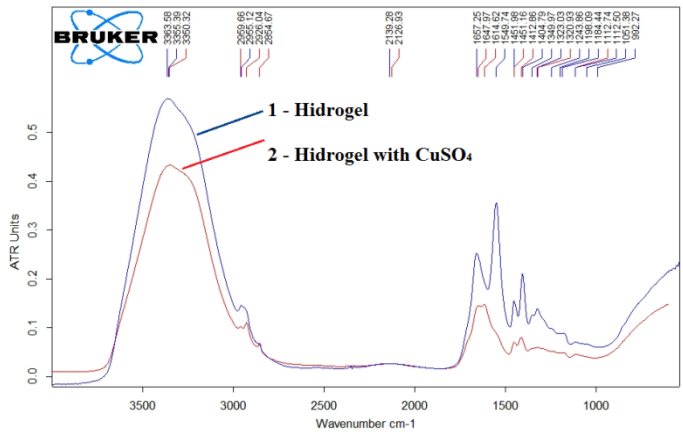

Fig. 2: IR-spectrums of 1 – hydrogel and 2 – hydrogel after sorption of ions of copper from 1M of water solution of sulfate of copper.

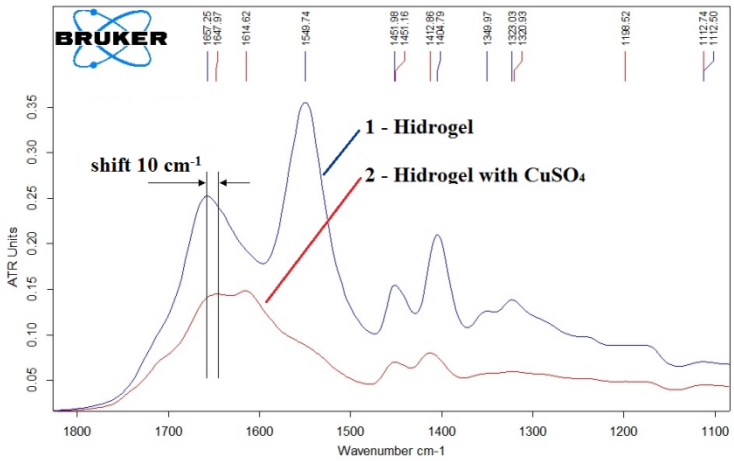

The fig. 3 Site of IR-spectrums of 1 – hydrogel and 2 – hydrogel with copper particles in the range from 650 cm^{-1} to 1750 cm^{-1}.

Conclusions:

In the analysis of IR-spectrums of the hydrogel and hydrogel with sorption of copper's ions the conclusion is drawn that there is not an adsorption, but a hemosorption of metal's ions by hydrogel. Change of frequency of FTIR-radiation absorption in areas of vibrations of functional groups –CO shows that there was an accession of an ion of metal to groups – CO. Thereof reduction, the number of hydrogen bonds in hydrogel, and also increase in molecular weight, due to introduction of an metal's ion and as a result reduction in the frequency of vibrations of bond – CO, i.e. chemical sorption of ions of metal have happened.

During the sorption of copper's ions by hydrogel changes in the frequency of deformation vibrations of groups - CH in the field of the frequencies of 1404 - 1412 cm^{-1}, and have appeared an additional peak 1614sm^{-1}, that is connected to the introduction of Cu^{+2}. Copper is an active element concerning formation of complex connections in which communications are formed on the donor-acceptor mechanism. Ions of copper are bivalent and show coordination number 4. In the sorption process by hydrogel, two valent bonds of copper form communications with group – CO, and the remained two external electrons show properties of a complex formation, forming communication on the donor-acceptor mechanism with groups – CH and – NH, as it is reflected in minor change of frequencies of – CH group vibrations. The emergence of the 1614 cm^{-1} peak is connected with emergence of groups – NH which have formed coordination bonds with Cu^{+2} ion and respectively there is a reduction of number of groups – NH having the associated to hydrogen bonds and that results a decrease of intensity at a frequency of 1548 cm^{-1}.

Thus chemical sorption of coopers ions in hydrogel was shown.

Results of the experiment shows the prospects for the usage of acrylic hydrogels as sensor materials for detection of ions of polyvalent metals.

References

[1] Interpretation of FTIR spectra of polymers and Raman spectra of car paints by means of likelihood ratio approach supported by wavelet transform for reducing data dimensionality, Agnieszka Martyna · Aleksandra Michalska, Grzegorz Zadora, Received: 14 November 2014 / Revised: 23 January 2015 / Accepted: 10 February 2015 / Published online: 11 March 2015, © Springer-Verlag Berlin Heidelberg 2015, Anal Bioanal Chem (2015) 407:3357–3376

[2] K. Nakanishi, Infrared absorption spectroscopy --- practical Holden-Day, Inc., San Francisco, 1962, pp. 233.

[3] L. J. Bellamy , Advances in infrared group frequencies - 1968.

Challenges and solutions to integrate and calibrate RF and microwave power and phase measurements inside a power amplifier for RF energy applications

Klaus Werner[1]

[1] *KW-TEC, 6603 DG Wijchen, The Nederlands*

Authors e-mail address: klaus.werner@kw-tec.de

RF Energy applications require solid state power amplifiers which also deliver feedback with respect to forward and reflected RF power levels. For some applications, also phase information and/or IQ vectors need to be made available, next to the magnitude of the signals. Ideally, all these information can be generated inside the amplifier to avoid further cabling and integration issues. This poses severe challenges in view of the high power levels next to very small (detected) RF signals. Hence, Isolation requirements on the order of 50 to 60dB within a few centimeters need to be realized, which tend to be costly and mechanically involved.

At the same time, all the functionalities need to be provided at rock bottom prices in view of consumer oriented applications (solid state cooking, plasma lighting, etc.).

This paper will report on the current status quo of the RF Energy application markets. It will focus on a number of possible solutions to above mentioned technical and application requirements. Integrated reflectometers and –coupler structures as well as point-of-use phase detection will be discussed. It will conclude with a brief overview of other, RF Energy system related measurement and modelling challenges.

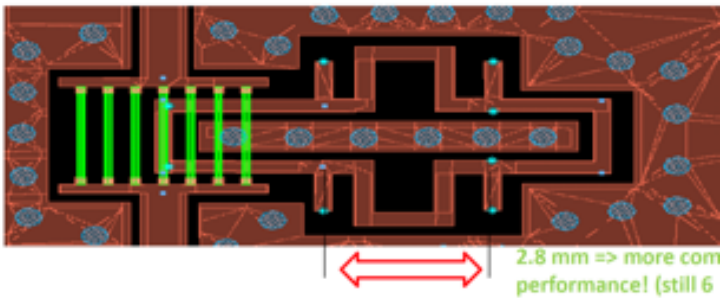

Sensorics in energy saving and water treatment

G. Lukyanov, I. Kovalski, A. Malyshev

Institute of Sensorics, ITMO University,197101, Kronverkski Pr.,49, St-Petersburg, Russland

Author e-mail address: gen-lukjanow@yandex.ru

Abstract

Life of modern society, especially big cities is impossible without power and water supply. Resources and money are spent for these purposes. Saving these funds and resources for our civilization are one of the most important goals. Energy savings can be seen in various aspects, it is true not only for housing and communal services, but also for industrial enterprises.

To solve this problem it is necessary to have information about the actual energy consumption. Typically, it is obtained from measurements of various parameters such as coolant flow rate, temperature, heat flux.

Typically, the operating principle of sensors to measure heat flow based on the Fourier law:

$$q = -\lambda \frac{\partial t}{\partial x} \quad , \tag{1}$$

where $q=Q/S$, *W/m2,* Q - heat flux, W; λ - thermal conductivity, W/m·K; x – coordinate, m; $t(x)$ - temperature profile along the x-axis, °C; S – surface, m^2. If such a sensor is placed for measurement on any wall, and if the thermal conductivity of the material of the sensor is low, it prevents the passage of heat flow and gives incorrect values . With high thermal conductivity of the material of the sensor value of Δt is very small and there are difficulties in its measurement. Also heat flux sensor on this principle has high inertia because it has a big size and weight.

We have developed and we use the heat flux sensor of on other principle. A basis of his functioning is the processes into ferroelectrical ceramics. Passing of heat through this plate leads to its electric polarization. The plate becomes electrically charged. If now such a capacitor discharge, the discharge time is proportional to the amount passed through the plate heat. Thermal and electrical power are related by:

$$C_T \frac{\partial t}{\partial \tau} = C_E \frac{U^2}{2} \frac{1}{\tau} \quad , \tag{2}$$

where $C_T=\rho c_T V$ the full thermal capacity, c_T is a thermal capacity, ρ – density, V- volume, τ - time, C_E - electrical capacity, U - voltage.

Appearance of the heat flux sensors on the considered principle is given on Fig. . Typical dependence of capacity on temperature is presented on Fig.1.

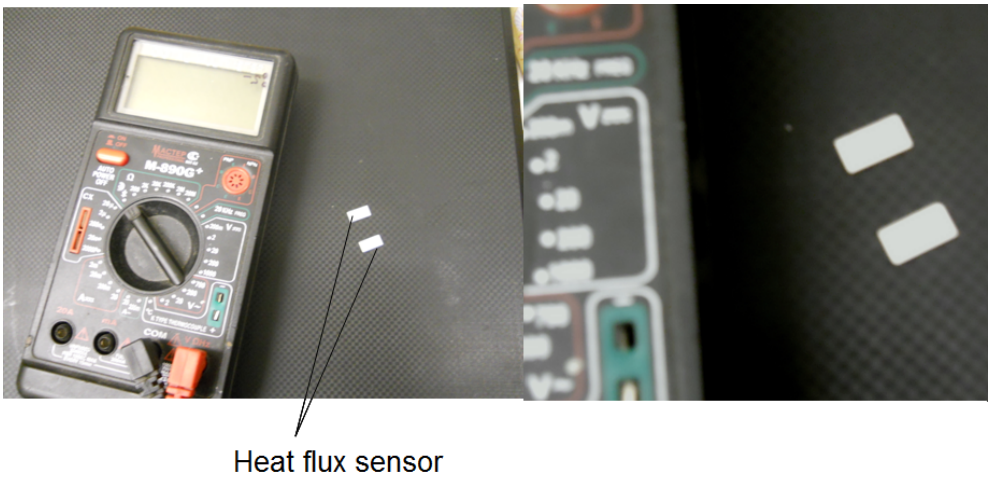

Fig. 1: Appearance of the heat flux sensors

Tests are performed on the basis of the laboratory of the ITMO University "Sensors and Sensor Networks in Energy Saving" (Fig. 2).

Fig. 2. Laboratory of the ITMO University "Sensors and Sensor Networks in Energy Saving"

Heat flux sensor has shown good reproducibility properties from instance to instance and can be produced in any quantity in the electronics industry enterprises.

Problems in water treatment require among others the following issues:

- Energy saving as cleaning solution of problems requires significant energy consumption;
- Minimizing the emission of harmful gases, such as CO_2;
- Control of the composition of water and the reaction to his departure from the norm. This is true also in the control of effluents.

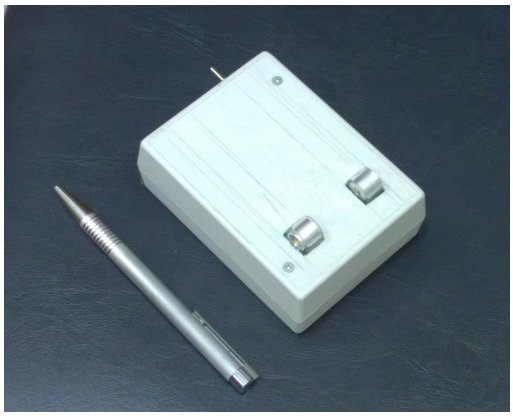

Fig. 3: Gptical sensor

An optical sensor [1] (Fig. 3) used to measure the CO2 concentration.

Sensor has the maximum sensitivity on the wavelength of 4,3 microns that corresponds to strong absorption of CO_2

The electric sensor with time of measurement of an order of units of milliseconds is applied to measurement of a deviation of composition of water from norm. The next figure (Fig. 4) shows the sensor response to various composition of water. Blue curve is tap water, green is mineral water “Yessentuki” and the red curve is drinking bottled water

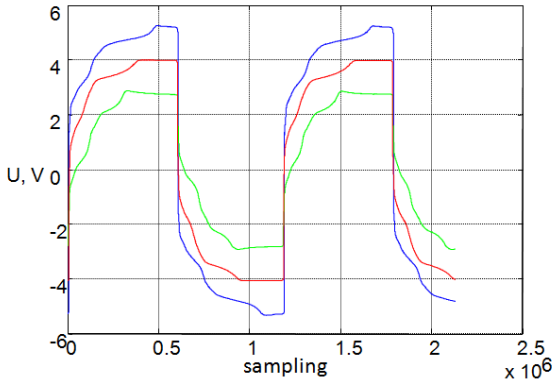

Fig. 4: Sensor response to various composition of water

Acknowledgements: This study was financially supported by the Ministry of Education and Science of the Russian Federation (the Agreement No. № 14.578.21.0111), a unique identifier for Applied Scientific Research (project) RFMEFI57815X0111.

References

[1] Rassadina A.A., Lukianov G.N., Malyshev A.S. The prototype of the sensor system for monitoring greenhouse gas emissions to wastewater treatment plants // Proc. of the III International Scientific and Practical Conference «Sensorica-2015» - 2015, pp. 64-66, ISBN 978-5-7577-0513

An Improved RSSI Localization Technique for Wireless Sensors Networks

Dhouha El-Houssaini, Sabrine Khriji, Olfa Kanoun

[1]*National School of Engineers of Sfax, Sfax,Tunisia*

Authors-mailaddress:houssaini.dhouha@gmail.com

Abstract

Localization is considered as one of the most important services provided by WSN [1]. The goal of this work is to develop a new algorithm that determines the location of static nodes in outdoor environments. Many localization techniques can be observed. Aiming to have an energy efficient, low cost and small size network, the Received Signal Strength Indicator (RSSI) [4,5] is proven to be adequate to measure the distances between nodes in large scale. Since the radio signal is unpredictable and sensitive to multipath, a selection algorithm is proposed based on the use of the fuzzy logic [3]. A selection of the three nearest and available reference nodes is applied which will reduce the problem of erroneous values of RSSI.

Method

The problem of sensor localization is to find out the location of sensor nodes based on input data. If there is any reference available in the network, the common inputs are the location of references while other inputs are based on the measurement techniques. The proposed algorithm is proceeded in three steps. First the node deployment where nodes are deployed randomly in a grid area. Second distance determination between sensor nodes and beacons is estimated using the RSSI values. Finally positions calculation is obtained by applying multirateration method combined with maximum least square estimation.

The RSSI value presents the attenuation of the transmitted signal, the logarithmic distance path loss model can be calculated as : $RSSI = P(dBm) = A - 10 \times \eta \times \log(d)$ where; d is the Euclidian distance between the receiving reference node and the sending node, η is the path loss exponent in propagation environment (free space model η =2), A is the path loss at known reference distance d0 (dBm). Using the previous equation and with simple mathematical modification the distance between node j and a beacon node can be easily deducted:

$$d = 10^{\left(\frac{A-RSSI}{10\times\eta}\right)}$$

In order to improve the accuracy of the localization algorithm, the unknown node should be contained in the coverage area of the selected references as presented in figure1. Therefore, a threshold is applied to the calculated distance between the selected reference and the unknown node.

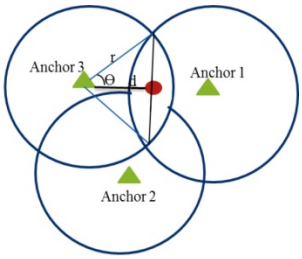

Figure 1 interconnexion between one unknown node three reference nodes

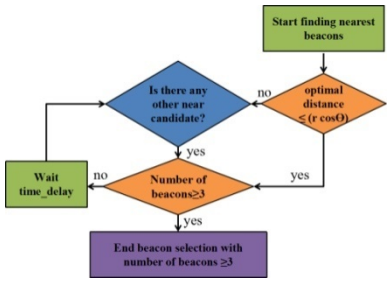

Figure2 Fuzzy logic flow chart

To calculate the estimated distance reference to unknown node a simple geometric projections with the Pythagoras theorem were used; cosΘ = d/r , where r is radius of the reference node and d is the calculated distance reference-to-unknown-node. So, to select the closest reference to the unknown node, the calculated distance reference-to-Uunknown should be lower than the radius of the selected reference multiplied by the cosines of the angle of arrival of the transmission line ; optimal distance ≤ r cosΘ. Thus each node tries to look for all its neighbors. If another node is placed within the same reference range, this node becomes an reference candidate and so it calculates its delay time and its chance using fuzzy logic (figure2).

Simulations

Many parameters are to be initiated to make simulations. These parameters are related to the application specifications such as the number of nodes, the dimensions of the field and to the properties of the sensor node especially the radio. Simulations are performed in Matlab to study the performance of the defined algorithm as well as to compare it to other existent algorithms.100 sensor nodes are deployed randomly in a 100*100 m² field. The Beacon nodes are placed randomly in the field.

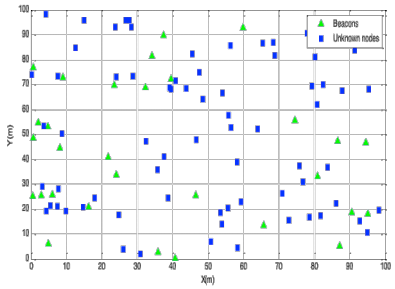

Figure 3 randomly deployed 100 sensors nodes

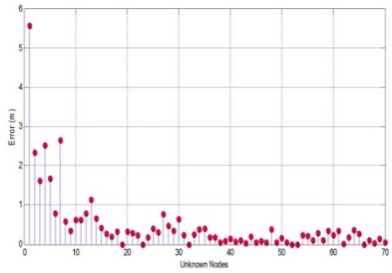

Figure 4 error estimations

To understand the efficiency of the algorithm a comparison between the results obtained and the real values could be presented. Therefore the two following tables present respectively the real coordinates of the unknown nodes and the estimated values obtained after applying the localization process. Also the error obtained while computing the distances is presented in figure 4.

Table 1 Real coordinates of unknown node in the range of R

	1	2	3	4	5	6	7
1	31.1321	72.5320	44.5551	69.8864	19.9822	51.3534	29.3647
2	53.3890	72.7408	49.1589	52.7405	52.3147	56.5986	86.8584

Table 2 *Estimated Coordinates In Range R Of Sensor*

	1	2	3	4	5	6	7
1	36.8402	71.1335	42.1220	64.1957	28.1816	49.6112	38.1753
2	52.4451	78.7793	46.8081	61.5316	47.8427	58.9730	82.2136

Conclusion

Localization is an important issue in WSN. Many solution are proposed in order to reduce the cost the size and energy consumption in both levels the node and the network. The goal of this work is to develop a new algorithm that determines the location of static nodes in outdoor environments. In this work the RSSI technique was used to estimate distance between nodes. The fuzzy logic method were presented to select the best near reference node in order to ensure a better accuracy and unnecessary computational effort . For future aspects the behavior of the proposed algorithm is intended to be tested for dynamic networks

References

[1] K . Bhaskar, “Wireless Sensor Networks”, The Second International Conference on Intelligent Sensing and Information Processing (ICIIP), Chennai, India, January 2005.
[2] P. Carlos, "Centre for Wireless Communications Wireless Sensor Networks”, Proc. Int. Workshop on Wireless Ad-Hoc Networks , pp.300 -304 , 2004.
[3] V. Kumar, A. Kumar and S. Soni, “A New Fuzzy Based Localization Error Minimization Approach with Optimized Beacon Range” , 2nd International Conference and workshop on Emerging Trends in Technology (ICWET), 2011.
[4] Y. Yao, Q. Han, X. Xu and N. Jiang, “A RSSI-Based Distributed Weighted Search Localization Algorithm for WSNs”, Hindawi Publishing Corporation International Journal of Distributed Sensor Networks , Article ID 293403, 11 pages, 2015.
[5] Z. Chen, W. Han, Y. Jiang and F. Yin, “A Modified RSSI-Based Indoor Localization Method in Wireless Sensor Network” , International Conference on Mechatronics, Control and Electronic Engineering, 2014.

Sensor for determining the composition of fluid

I. Kovalskiy[1], G. Lukyanov[1], A. Fedorov[2], S. Volkov[2]

[1]ITMO University, 197101, Saint Petersburg, Russian Federation
[2]ALL-RUSSIAN RESEARCH INSTITUTE OF FATS, 191119, Saint Petersburg, Russian Federation

Authors e-mail address: ilya.kovalskiy@hotmail.com

Abstract

The composition of the substances commonly occurs by using these basic methods: spectroscopic, diffraction, optical. All these methods are based on determining the radiation changes, fields or particles flow after interaction with the substance having a set of physical properties.

All of these methods have sufficiently accurate determination of the composition substances, but in the real industry is not always required an exact determination of the composition, for example, in the oil industry should be conducted rapid tests to determine the type of oil or water utilities need to control the level of emissions of harmful substances by various companies.But the solutions to these problems, by existing methods are not cost-effective and therefore require the development of new methods and techniques to determine the change in the composition of substances.

In particular, to solve these problems, have been suggested a method of determining the composition and / or by measuring the dynamic changes electro physical characteristics and their subsequent treatment.

As objects of study in the early stages of work were selected different samples of sunflower oil and water, and it is no coincidence, because the plant oils are major source of energy for humans, and water is an essential substance for all living beings on the planet, and used in many manufacturing processes.

Formed research program is aimed to define such characteristics for liquids that could make it possible to link the electrical properties of liquids with a concentration of the individual components. Only in this case the data may be used to form an adequate information model.

In this research program to study the electrical properties of plant oils should position sunflower oil as initial research object, because the composition of the main components of plant oil - oleinic acid (C18: 1) and linoleic acid (C18: 2) varies over the entire range of concentration values taking place separately for each of a plurality of other vegetable oils.

In accordance with the research program of measuring the dynamic electrical properties of oils the laboratory setup was created. It allows us to study changes in the numerical values of electro physical parameters depending on the concentration of the individual components plant oils.

As the objects of the study were selected three sample of refined sunflower oil having a fatty acid composition specified in Table 1. Determination of the fatty acid composition was performed on BRUKER «Scion 436-GC» capillary gas-liquid chromatograph using a Bruker «Wax-fame» capillary column.

Table 1. Fatty acid composition of samples of refined sunflower oil.

Name fatty acid	Reference designation	Relative concentration (%)		
		Sample №1	Sample №2	Sample №3
Palmitinic	C 16:0	5,9	6,4	4,0
Stearinic	C 18:0	3,4	3,1	2,6
Oleinic	C 18:1	23,7	31,4	81,6
Linolic	C 18:2	66,3	58,1	11,6
Arachic	C 20:0	-	-	0,2
Behenic	C 22:0	0,7	1,0	0,1

For each sample of sunflower oil were obtained values of output level changes in time at the measuring cell. Figure 1 clearly shows that functions have characteristic maximum rate of changing the output level of the values of the measuring cell. The character of the data obtained for three different samples of sunflower oil, confirms the presence of proportional growth rate of its value changes in process of increase concentration of oleic acid in the samples. Thus, during the studies were obtained numerical values of electro physical parameters.

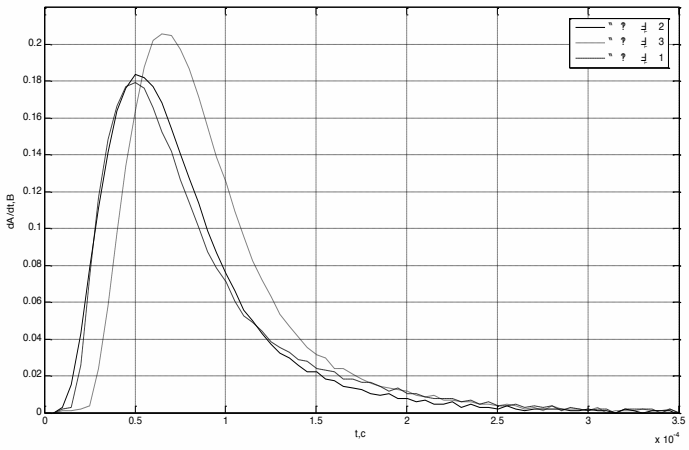

Fig. 1. The dependence of the rate of change of the output signal from the measuring cell time for various samples of sunflower oil.

The relationship between the concentration of the main component plant oils - oleinic acid and electro physical parameters of sunflower oil in the analytical laboratory unit cell has been discovered. It can be concluded about the possibility of creating express-method for determining compliance with the standards of the quality requirements of sunflower oil based on the detected patterns.

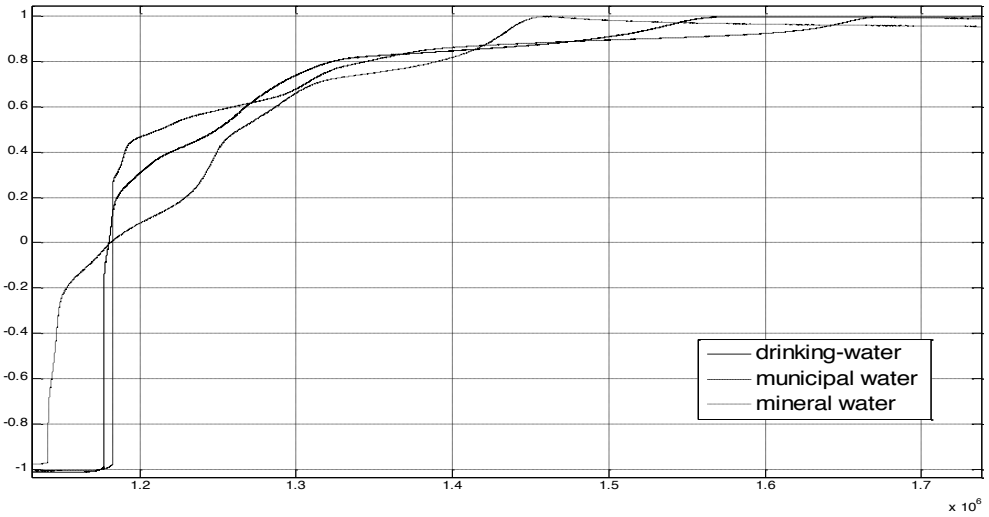

Figure 2

Figure 2 shows plots of the output signal in the primary analysis of various samples of water from which it is evident that they are strongly dependent on the water content. It can be concluded about the possibility of creating express method for determining change in the **c**omposition of substances based on the detected patternson the basis of the data obtained.

References

[1] AB Rudakov, AN Ponomarev, KK Polyansky, A. Lyubarev. Fats. The chemical composition and quality expertise. Moscow. De Li print. G. 238 to 2005.

[2] Modern aspects of the technology and expertise of vegetable oils. Department of examination of consumer goods VPO "SP-B EMT" Report. St. Petersburg. EMT. 2012 124.

[3] IB Lubchenco, EA Nikitin. Comprehensive quality control at the enterprises of oil and fat materials. St. Petersburg, 2012 243 s.

Efficiency Considerations for Multichannel Impedance Spectroscopy Measurement Systems in Battery Applications

Thomas Günther,[1] Olfa Kanoun[1]

[1]*Professur Mess- und Sensortechnik, Technische Universität Chemnitz, 09126 Chemnitz, Germany*
Authors e-mail address: thomas.guenther@etit.tu-chemnitz.de

Abstract

Impedance Spectroscopy is a well-known method for system identification[1], [2]. By the obtained data a non-invasive insight into the device under test is provided. These data can be used for state determination and prediction.[3]–[5] Due to the complexity of laboratory setups it is challenging to migrate this method for system identification into portable applications [6]. Different obstacles have to be faced to make this method for multichannel measurements available in low-cost and low-power applications. Main issues are hardware complexity and complexity of algorithms for data processing. A hardware approach for multichannel impedance measurements has been presented by the author to reduce the effort concerning hardware complexity[6]. In this article an improvement to reduce the computational load further by avoiding unnecessary measurements is presented. Thereby the total number of required measurements reduced by keeping the amount and precision of the obtained data. Consequentially either the capability to measure more channels or a reduction of the requirements for the setup is the outcome.

Method

For impedance spectroscopy at low impedance systems, the voltage response is measured together with the excitation current. When the time domain data for the current and the voltage are transferred into the frequency domain the linear transfer function of the investigated system, known as the complex frequency dependent impedance, can be calculated. In some cases multiple response channels refer to one perturbation path (compare to Figure 11 left). The intuitive approach for the measurement of the perturbation and response implies a cyclic simultaneous sampling of the perturbation and response for each channel (compare to Figure 11 right). This results in a fixed alignment within the cycle for all sampling processes per channels in the multichannel measurement system.

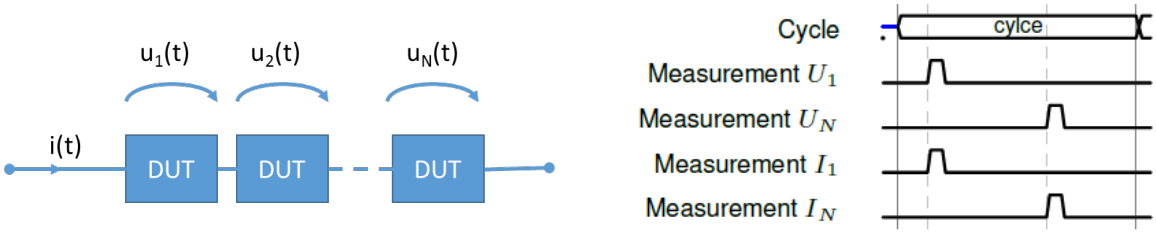

Figure 11: Multichannel system with one perturbation and multiple response channels (left); Timing diagram for measurement of data for determination of response characteristics for each channel 1… N within one cycle

Within one cycle each channel is going to be measured at least once. Depending on the device under test additional marginal conditions such as a series connection of all DUTs as depicted left in Figure 11 can be utilized. In this case the excitation is the same for all DUTs. Concluding that the following equation for the impedance for non-simultaneous sampling of excitation and response can be obtained.

$$Z(\omega,\alpha)=\frac{F\{U(t)\}}{F\{I(t+\alpha)\}}=\frac{U(\omega)}{I(\omega,\alpha)}=\frac{U_0(\omega)}{I_0(\omega)}\cdot e^{j(\varphi_u-\varphi_i)}\cdot e^{j\varphi_\Delta}\cdot e^{j\varphi_\epsilon}$$

By grouping the influencing effects the following dependencies are:

- magnitude and phase of the DUTs frequency dependent impedance
- phase shift φ_Δ depending on the misalignment Δ between the sample of voltage and current for a particular channel
- Phase noise due to stochastic errors

When all measurements occur in a fixed relative alignment, then a fixed time delay Δ between the samples per channels will be existing. Time shift between the signals for voltage and current will be present i.e. due to different signal conditioning HW or signals paths in the measurement system. Therefore the time shift Δ need to be

calibrated. This can be used to avoid the measurement of all but one channel of the current measurement depicted in the timing diagram in Figure 11.

The mentioned time shift Δ appears as frequency and channel dependent phase shifts φ_Δ visible as rotational deformation in the impedance spectrum (compare to Zmisaligned in Figure 12 left). Therefore the shift theorem of the Fourier transformation is the basis to compensate these deformations of the impedance spectra. In Figure 12 the impact and result after compensation of the deformations related to the phase shifts are depicted.

Consequentially for multichannel measurement systems the efficiency of the method increases the more channels are going to be measured. Thus up to almost 50 % of the measurements can be treated as unnecessary and can be avoided in multichannel impedance measurements (compare to Figure 12 right).

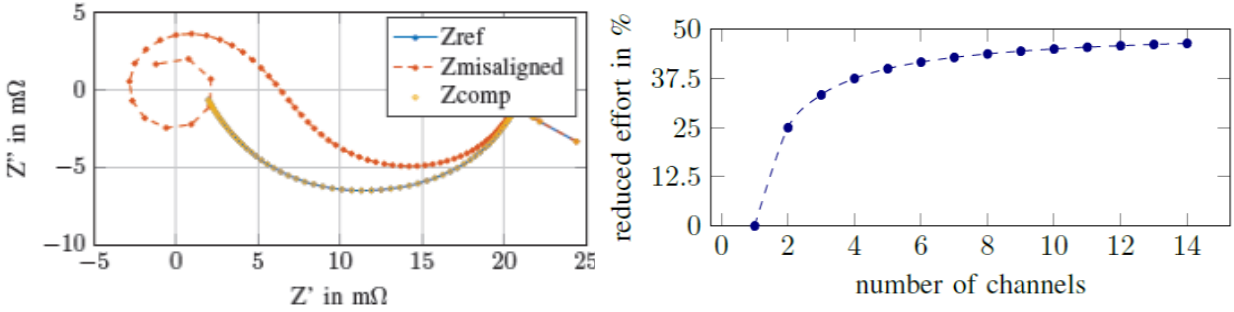

Figure 12: Effect of a time shift Δ on the shape of an impedance spectrum (left), reduction of the effort in multichannel measurements by avoiding unnecessary measurements and reconstruction by the shift theorem

Design Criterion

How much misalignment regarding the compensation of the time delay between voltage and current is acceptable depends on the target applications frequency range. A remaining error of 0,1 % with respect to the correct value of the impedance is a common threshold. Therefore a simple design rule for the remaining time shift Δ after compensation and calibration is derived as:

$$|\Delta| \approx 0{,}1\ \%/\omega$$

The effect of misalignment regarding the sampling process in measurement channels is inverse proportional to the investigated frequency. For battery applications the maximum frequency of about 1 kHz results in a maximum acceptable misalignment in the measurement channels of approximately 159 ns after calibration. Nowadays microcontrollers as the STM32F4 operate at frequencies of about 168 MHz..[7] Consequentially the time base for triggering analog to digital conversions has a higher precision as the required 160 ns with approximately 6 ns.

Conclusion

A method to reduce the effort for measurement in multichannel systems for impedance spectroscopy by utilizing the shift theorem of Fourier transforms has been proposed. Therefore up to 50 % of the measurements can be avoided. This allows to increase the number of measured channels use less powerful hardware. Furthermore an equation for the design process of the measurement hardware has been presented to indicate the required precision either in the timing depending on the target frequency range for impedance measurements.

References

[1] M. E. Orazem and B. Tribollet, Electrochemical Impedance Spectroscopy. Wiley, 2011.

[2] R. Pintelon and J. Schoukens, System Identification: A Frequency Domain Approach. Wiley, 2012.

[3] U. Tröltzsch, "Modellbasierte Zustandsdiagnose von Gerätebatterien," Universität der Bundeswehr München, 2006.

[4] P. Büschel, U. Tröltzsch, and O. Kanoun, "Use of stochastic methods for robust parameter extraction from impedance spectra," Electrochim Acta, vol. 56, no. 23, pp. 8069–8077, Sep. 2011.

[5] U. Tröltzsch, O. Kanoun, and H.-R. Tränkler, "Characterizing aging effects of lithium ion batteries by impedance spectroscopy," Electrochim Acta, vol. 51, no. 8–9, pp. 1664–1672, Jan. 2006.

[6] T. Günther, P. Büschel, and O. Kanoun, "Eingebettetes Impedanzmesssystem für das Batteriemanagement in Elektrofahrzeugen," Tm - Tech. Mess., vol. 81, no. 11, pp. 560–565, Nov. 2014.

[7] "STM32F4DISCOVERY - STMicroelectronics." [Online]. Available: http://www2.st.com/content/st_com/en/products/evaluation-tools/product-evaluation-tools/mcu-eval-tools/stm32-mcu-eval-tools/stm32-mcu-discovery-kits/stm32f4discovery.html. [Accessed: 25-Apr-2016].

Application of nonlinear autoregressive model with external inputs for identification and filtering of experimental data

S. A. Polistchouk
ITMO University, Russia, St. Petersburg city, Kronverksky Ave., 49
Author e-mail address: Gersey@yandex.ru

Abstract

The application of nonlinear dynamic models based on autoregression filtering of the experimentally determined series of observations. This was used NARMAX model. Presents the results of identification and filtering of the experimentally determined series of observations of fluctuations of the concentrations of carbon dioxide at wastewater treatment plants of sue "Vodokanal", as well as physical quantities in the process of respiration [1-4].

The aim of research

Testing of possibilities of application of nonlinear autoregressive model with external inputs for identification and filtering of experimental data.

Basic provisions of research

The method NARMAX (Nonlinear Autoregressive Moving Average with eXogenous Iinputs) is used.[5] As an illustration of the application of nonlinear dynamic models based on the method used to filter experimental data on fluctuations of carbon dioxide concentrations at wastewater treatment plants of sue "Vodokanal" and the physical quantities in the breathing process (pressure and temperature).

Interim results

Identification and filtering of fluctuations of the concentrations of carbon dioxide at wastewater treatment plants of sue "Vodokanal" and the physical quantities in the breathing process (pressure and temperature).

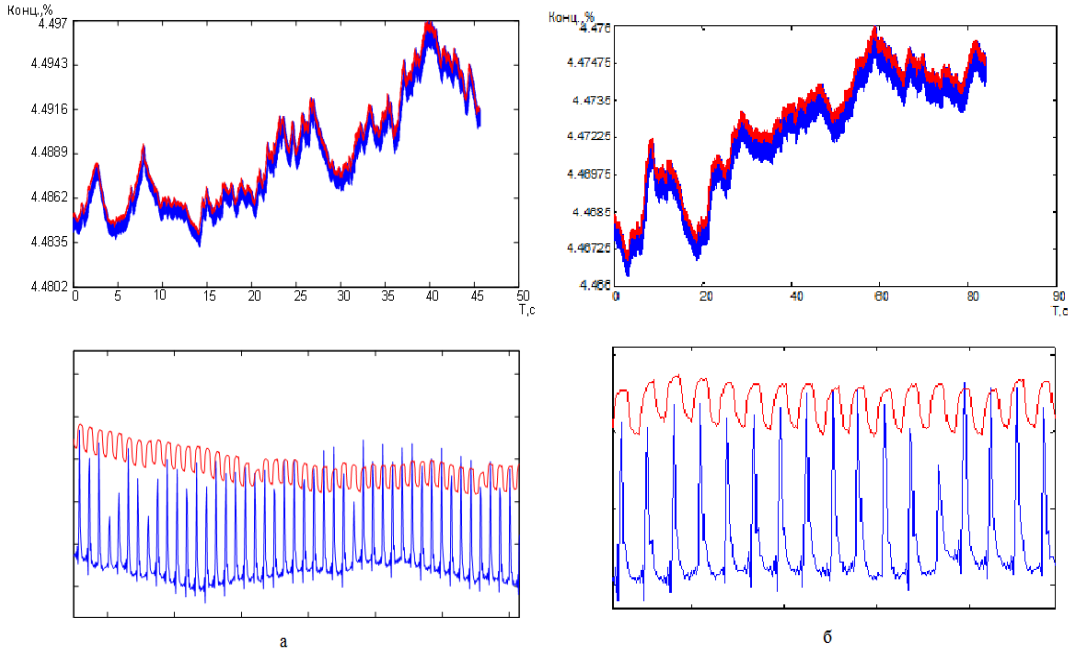

Pic.1: Charts the fluctuations of carbon dioxide concentrations: a,b-the Results of data processing of monitoring the concentration of carbon dioxide.

Polinomial model:

Y(t)= -1.3211-0.233626*y(t-1)-0.00384242*y(t-1)*y(t-1)-0.00047096*y(t-1)*y(t-1)*y(t-1)*y(t-1)

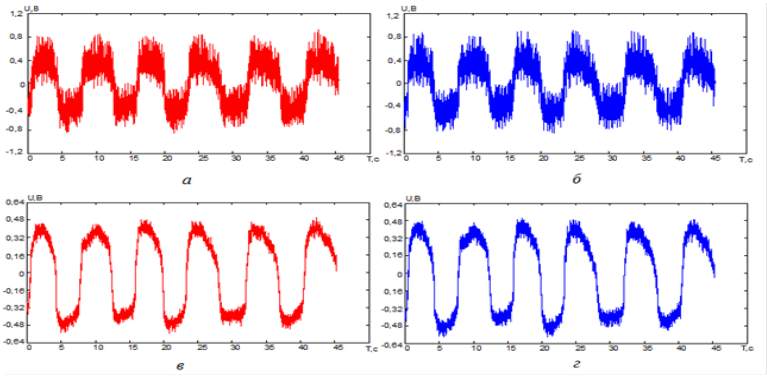

Pic. 2: Charts of breathing: a, b – the pressure in the left and right nostril respectively, without filtering;C,d – the pressure in the left and right nostril after filtering

Polinomial model:
right nostril
Y (t)= -377.5-66.8922*y(t-1)-8.85864*y(t-1)*y(t-1)-1.10905*y(t-1)*y(t-1)*y(t-1)*y(t-1)
left nostril
Y(t)= -456-80.6471*y(t-1)-10.6407*y(t-1)*y(t-1)-1.32749*y(t-1)*y(t-1)*y(t-1)*y(t-1)

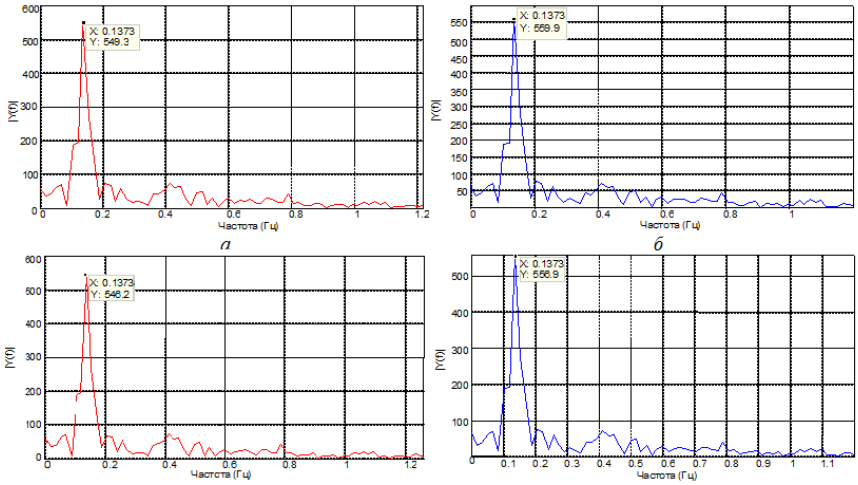

Pic. 3: Graphs of power spectral density: a,b – the pressure in the left and right nostrils until filter, respectively; C,d – the pressure in the left and right nostrils after filtering, respectively

The main result

The use of nonlinear dynamic models based on autoregression filtering of the experimentally determined series of observations allows to adequately describe the processes, regardless of their nature.

References

[1] ГОСТ Р 14064-2007. Газы парниковые. Часть 1. Требования и руководство по количественному определению и отчетности о выбросах и удалении парниковых газов на уровне организации. М.: Стандартинформ, 2010

[2] Молчанова Я.П., Гусева М.С., Данилкина М.С. Углеродный след – новый аспект добровольной отчетности предприятий водоснабжения и водоотведения. // Вестник РХТУ им. Д. И. Менделеева. Гуманитарные и социально-экономические исследования. В 2-х томах. Том 2. Социально-экономические исследования. Выпуск III. –М.: РХТУ им. Д. И. Менделеева, 2012. С. 137-146.

[3] Бегак М.В., Гусева Т.В., Молчанова Я.П., Аверочкин Е.М., Сагайдук В.Л. Мониторинг и сокращение углеродного следа российских водоканалов. Методика определения углеродного следа сооружений очистки сточных вод. М.: Российский химико-технологический университет имени Д. И. Менделеева, 2013. − 56 с.

[4] Sweetapple C., Fu G., Butler D. Multi-objective optimisation of wastewater treatment plant control to reduce greenhouse gas emissions. // Water Research. Vol. 55, 15 May 2014, Pages 52–62. doi:10.1016/j.watres.2014.02.018. URL: http://www.sciencedirect.com/science/article/pii/S0043135414001341

[5] Billings, S.A Extended model set, global data and threshold model identification of severely non-linear systems,/ Billings S.A., Int. J. Control, vol. 50, no. 5, 1897-1923, 1989.

Crack Detection in Hot Rolled Rods

T. Morgenstern[1], N. Golischewski[1], A. Pritula[1], O. Kanoun[2], J. Himmel[1]

[1]*Institute of Measurement and Sensor Technology, University of Applied Sciences Ruhr West, 45479, Mülheim an der Ruhr, Germany*
[2]*Faculty of Electrical Engineering and Information Technology, Technical University Chemnitz, 09111, Chemnitz, Germany*

Authors e-mail address: Tino.Morgenstern@hs-ruhrwest.de

Abstract

Semi-finished round products made of high quality steel are based on crack and defect free rods. Thus eddy current sensors are well-established with improvements of rolling processes and their measurement systems. A major challenge is the online detection of cracks and other surface defects in hot rolled rods during the rolling process with up to 100 m/s rod speed and up to 1200 °C rod temperature [1]. This study is dealing with the crack detection in rods based on inductive measurement systems. By using an excitation coil a magnetic field is generated to induce an eddy current in the rods surface. As a consequence a secondary magnetic field is generated, which influences the excitation field. Cracks in the rod influence the field dependent on their depth, width and length. For the detection of these influences detections coils and GMR sensors were used.

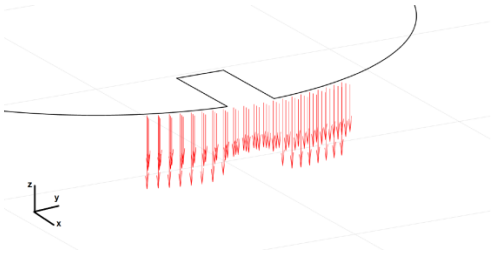

Fig. 1 Crack influenced magnetic flux density close to rod surface [2]

The eddy current skin depth in the frequency range of 1MHz up to 20 MHz is smaller than 500 µm. Therefore they can be approximated by surface line currents.

Additionally this set up is simulated as a mathematical model using Biot – Savart`s law. Thus it is possible to calculate stationary magnetic fields to comprehend the physical effects. Depending on the excitation coil geometry and the rod position in the coil the z-component of the magnetic field is the dominant field part. It can be described with equation (1).

$$B_z = \frac{\mu_o I}{2\,\pi} \int_0^{\pi} \frac{a^2 - a\rho\cos\phi}{\cos(a^2 + \rho^2 - 2a\rho\cos\phi)^{\frac{3}{2}}} d\phi \tag{2}$$

In this application the cross-section-areas of coils and rods without cracks have a circular shape. The equation (1) can be solved with elliptical integrals [3]. If rods include cracks the circular shape is altered as shown in Fig 2. The calculation has to be realized by separated integrations for each section. Therefore the rod shape is split in 4 parts. Part 1 is the cylindrical part of the rod with less than 360 ° circumference, part 2, 3 and 4 are straight lines where part 2 and 4 corresponds the crack depth and part 3 the crack width.

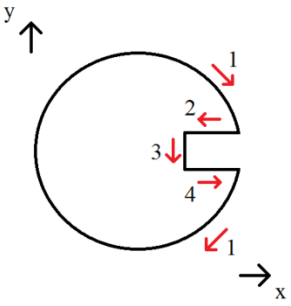

Fig. 2 Rod shape [2]

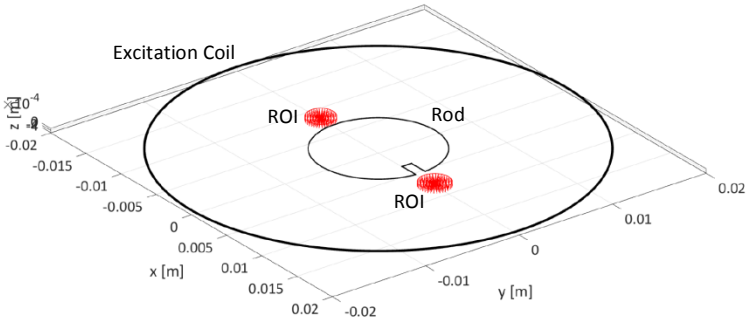

Fig. 3 Coil and rod shape with ROIs [2]

In Fig. 3 the excitation coil, the rod shape and the region of interest (ROI) are shown. To find out the crack influence the ROIs are placed closed to the rod surface. Modeling the excitation coil the number of turns corresponds to the number of current lines and the coil length by the distance between the current lines. Here the coil length is parallel to the z-coordinate. To get a sufficient accuracy the rod length needs to be modeled with the double coil length and the double number of turns of the coil [2]. The ROIs can be interpreted as a cylindrical detection coil or GMR detector with the same length as the excitation coil. The crack influence can be determined by calculating the difference of the integration of the magnetic flux density in the ROIs volume. Depending on the ROI size and the ROI distance to the rod surface the crack influence represents about 0.13 %. This result is verified with the measurement set up under laboratory conditions.

References

[1] Morgenstern, T., Himmel, J., Kanoun, O. 2014. *Detektion von Rissen in Drähten auf Basis der ortsabhängigen magnetischen Induktion*. tm – Technisches Messen 2014; 81(11): 573–580.

[2] Pritula, A., Golischewski, N., 2016. *Analytische Berechnung und Validierung verschiedener Messmethoden zur Risserkennung*. Master thesis.

[3] Good R.H. 2001. *Elliptic integrals, the forgotten functions*. Eur. J. Phys. 22 (2001) 119–126.

Neighbourhood Frequency Maps
A new Approach in the discrete Domain of Heart Rate Variability.

J. Mockenhaupt, H.-H. Schäfer
University of Applied Sciences Bonn-Rhein-Sieg, 53773, Hennef, Germany
Author e-mail: Johannes.Mockenhaupt@h-brs.de

Abstract

In the last decades it became evident that the fluctuations in heart rate [HR] contain information about the balance of the sympathetic nervous system and the vagus as part of the parasympathetic nervous system. There are three commonly used analyzing methods available to extract and to visualize this information as the so called heart rate variability [HRV]. Basis for the application of these methods are heart beat series.
The sympathetic nervous system and the vagus (as part of the parasympathetic nervous system) influence the HR as well as the HRV. Due to their different neurotransmitters (catecholamines and acetylcholine) their mode of operation is different as well. While the sympathetic system increases HR, the parasympathetic system slows down HR. In contrast, the sympathetic system decreases HRV, whereas the vagus increases it. These effects can be found both in the time domain and in the frequency domain. Due to the extensive characteristics of the applied methods the gathered information is only entirely available, without possibilities to select a particular HR for a deeper analysis.
To overcome this disadvantage we have complemented the statistical tools in the time domain by a simple heart beat depended counting of successive heart beats. Instead of a whole observation we separated the given heart beats in classes, arranged in a vertical direction. The differences to successive heart beats may be positive or negative and lead to a classification in the horizontal direction. This arrangement of gathered heart beats and their classified successors can be displayed as a matrix of numbers or visualized as a mapping of pseudo-colours we named Neighbourhood Frequency Maps [NFM]. Although the term "frequency" is used synonymously for heart rate in medicine it should be kept in mind that the frequency is in a reciprocal relation to the counting of heart beats. The creation of such NFM is not time consuming, for all of the test cases, the computing time was smaller than the time of a beat-to-beat difference. NFM may allow real-time execution and can be used for further examinations in laboratory experiments as well as in field studies.

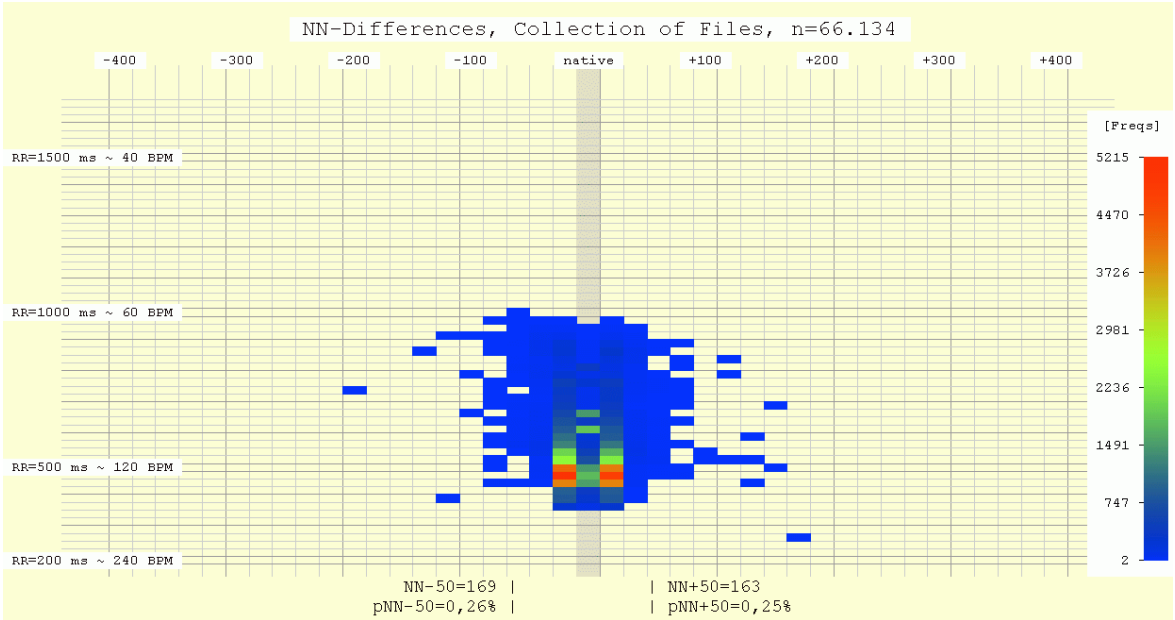

Fig. 1: A Neighbourhood Frequency Map obtained from 12 cycling training sessions.

IMPRESSUM

Editors:

Prof. Dr. Jörg Himmel, University of Applied Sciences Ruhr West
Prof. Dr. Thomas Seeger, University of Siegen
Prof. Dr. Klaus Thelen, University of Applied Sciences Ruhr West

Scientific Advisory Board:

Prof. Dr. Jörg Himmel, University of Applied Sciences Ruhr West
Prof. Dr. Klaus Thelen, University of Applied Sciences Ruhr West
Prof. Dr. Gennadij Lukjanow, ITMO University, St. Petersburg
Prof. Dr. Thomas Seeger, University of Siegen
Prof. Dr. Olfa Kanoun, Chemnitz University of Technology
Prof. Dr. Lothar Kempen, University of Applied Sciences Ruhr West
Prof. Dr. Dirk Rüter, University of Applied Sciences Ruhr West
Prof. Dr. Frank Kreuder, University of Applied Sciences Ruhr West

Responsible according to German press law:

President of the University of Applied Sciences Ruhr West, Prof. Dr. Gudrun Stockmanns,
Duisburger Str. 100, 45479 Mülheim an der Ruhr

ISBN: 978-3-9814801-7-7

University of Applied Science Ruhr West
Duisburger Str. 100
45479 Mülheim an der Ruhr

Cover design:

Agatha Gebus
Stabsstelle PR & Marketing

Print

University of Siegen
UniPrint
Hölderlinstr. 3
57076 Siegen
Print run: 150 pieces, as of June 2016

Legal disclaimer

Mülheim an der Ruhr, Juni 2016

With generous support from: HRW FÖRDERVEREIN DER HOCHSCHULE RUHR WEST

HOCHSCHULE RUHR WEST
UNIVERSITY OF APPLIED SCIENCES

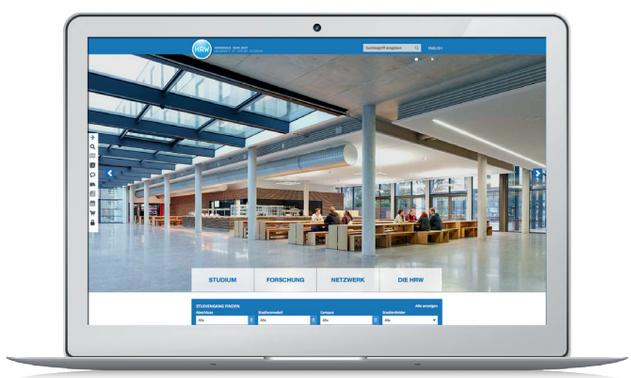

WWW.HOCHSCHULE-RUHR-WEST.DE